Modeling and characterization of polycrystalline silicon for solar cells and microelectronics

Von der Fakultät Informatik, Elektrotechnik und Informationstechnik der Universität Stuttgart zur Erlangung der Würde eines Doktor-Ingenieurs (Dr.-Ing.) genehmigte Abhandlung

vorgelegt von

Kurt R. Taretto

geboren in Buenos Aires

Hauptberichter: Prof. Dr. rer. nat. habil. Jürgen H. Werner

Mitberichter: Prof. Dr. phil. Erich Kasper

Tag der Einreichung: 1. Oktober 2002

Tag der mündlichen Prüfung: 3. Februar 2003

Institut für Physikalische Elektronik - Universität Stuttgart

2003

Contents

Abstract

The present work models and characterizes the electronic properties of polycrystalline silicon films and solar cells. The analytical and numerical models provide limiting values of solar cell efficiency that can be reached with polycrystalline silicon. These limit efficiencies are of prime interest for the development of the polycrystalline silicon solar cell technology. The electronic characterization of laser-crystallized silicon films given in this work, provides a complete picture of the electronic transport and recombination parameters, which were unknown up to now.

Polycrystalline silicon solar cells show a grain size dependence of the electrical output parameters, regardless of the preparation method. This work develops an analytical model considering the recombination in the space-charge region and in the base of the cell, finding that the open circuit voltage and the short circuit current density are linked by a *single* parameter, which is the *effective diffusion length*. Additionally, I develop a second model that relates the effective diffusion length to the short-circuit current density and the optical generation rate. Both models constitute new methods to *extract* the diffusion length in a solar cell.

The model is then utilized to explain the grain size dependence of polycrystalline silicon solar cells output parameters over *six orders of magnitude* of the grain size. I show that the literature data of 10 % efficient cells with grain sizes as small as 10 nm, is explained by a very low grain boundary recombination velocity between 100 and 1000 cm/s. The origin of such low recombination velocities is proposed in a recent paper, which explains that since all the cells with small grains and high efficiency were reported to have a {220} surface texture, the low recombination velocity could be explained by a large amount of defect-free [110]-tilt grain boundaries.

A two-dimensional numerical model developed specifically for *pin* solar cells with small grain sizes, confirms that the efficient cells made from small-grained films, must have grain boundary recombination velocities in the range of 100-1000 cm/s, in agreement with the predictions of the analytical model. The simulations

also set bounds upon the efficiency of microcrystalline solar cells: with a grain size and cell thickness around 1 μm, and a recombination velocity between 100 and 1000 cm/s, an efficiency of 10 % can be reached using a *pin* structure (as confirmed by the record values found in literature); while a higher limit of 15 % is found for *pn* cells with highly passivated contacts. The higher efficiency limit found in the *pn* cells is a consequence of the Shockley-Read-Hall recombination statistics, which yields lower recombination rates at defect levels in the center of the energy gap in a doped material, leading to higher open circuit voltages of the *pn* cells compared to *pin* cells.

To give a more simple picture of the *pin* cells modeled numerically, an analytical model for the current/voltage characteristics of the *pin* cell is developed. Unlike the models shown up to now in the literature, the current/voltage equation of the *pin* structure developed in this work applies to *the whole* range of applied voltages between short-circuit and open-circuit conditions. I show that this model also explains many features observed in fine-grained silicon *pin* solar cells, and establish conceptual bridges between the *pin* and the *pn* cell. Thus, this model constitutes a new analytical tool to analyze *pin* solar cells.

The electrical characterizations of laser-crystallized silicon show that the films have p-type conduction, with a strong anisotropy of the conductivity due to the elongated shape of the grains. Hall measurements reveal a hole density between 4×10^{12} and 4×10^{13} cm^{-3}, indicating a compensated material, and mobilities between 12 and 120 cm^2/Vs. The conductivity of the undoped films lies at 10^{-4} S/cm at room temperature. The temperature-dependent conductivity reveals a distribution of grain boundary barrier heights, which are about 100 meV high. The carrier density and the barrier heights, imply a minimum defect density at the grain boundaries of 1.6×10^{10} cm^{-2}. The photoconductivity measurements give a mobility-lifetime product of 2.3×10^{-5} cm^2/V, a value that implies a high electronic quality of the films, which explains the high-quality thin-film transistors obtained with this material. These measurements permit to explain the good quality of laser-crystallized silicon, by means of fundamental electronic parameters of the films.

Furthermore, this work demonstrates that the use of laser-crystallized silicon may also be considered for vertical electronic devices, by preparing a test-diode structure made from laser-crystallized silicon prepared on a *metallic* instead of an *insulating* layer. The model of the *pin* cell fits the current/voltage characteristics of the diode with mobility-lifetime products greater than 4×10^{-6} cm^2/V, revealing good electronic quality also in these films.

The high electronic quality of laser-crystallized silicon films revealed by the electrical characterizations performed in this work, indicates that the application of this material to minority carrier devices, like bipolar junction transistors or solar cells, should deserve further investigation.

Zusammenfassung

Die vorliegende Arbeit stellt analytische und numerische Modelle zur Beschreibung von Schichten und Solarzellen aus polykristallinen Halbleiter vor. Weiterhin werden die elektrischen und optischen Eigenschaften laserkristallisierter Siliziumschichten untersucht.

Grundlagen (Kapitel 2). Die elektrische Modellierung von polykristallinen Schichten erfolgt durch die Beschreibung der im Bild 1 dargestellten Ladungsträgertransport- und Rekombinationsprozesse an einer Korngrenze. Das Banddiagramm an einer Korngrenze (KG) in p-Typ Material zeigt die Energieniveaus der Störstellen an der KG, die durch die Unterbrechung der Kristallstruktur zwischen den zwei benachbarten Körner hervorgerufen wird.
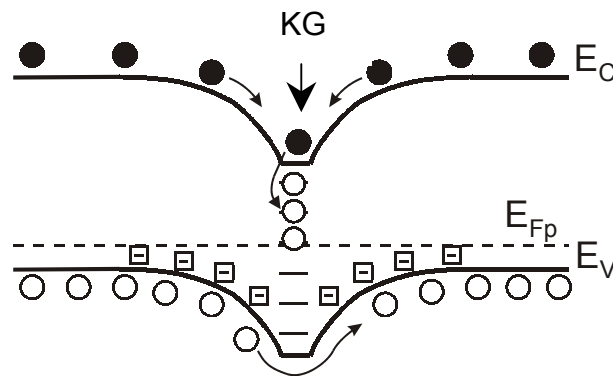
Bild 1. Dieses Banddiagramm um einer Korngrenze (KG) zeigt die Defektniveaus an der Korngrenze, in denen Ladungsträger eingefangen werden. Der Einfang von Ladungsträgern verändert die Ladung an der Korngrenze und es führt zu einer Bandverbiegung.

Die Störstellen fangen freie Ladungsträger aus den Bändern ein und bilden somit die Korngrenzladung. Diese Ladung führt zur Verbiegung der Bänder, die im Bild 1 zu sehen ist. Die entstandene Korngrenzbarriere behindert den Transport von Majoritätsladungsträgern von Korn zu Korn (im Bild 1 Löcher). Dieses Hindernis erklärt den in der Praxis gemessenen Anstieg des spezifischen Widerstands im Vergleich zu einkristallinem Material. Die Korngrenze wirkt außerdem als Senke für Minoritätsladungsträger (im Bild 1 Elektronen), die dort über die Defektniveaus mit Löchern rekombinieren. Die Korngrenzen stellen also im Vergleich zu einkristallinem Material einen zusätzlichen Rekombinationspfad

dar. Aufgrund dieses zusätzlichen Rekombinationspfades ist die Diffusionslänge von Minoritätsladungsträgern im polykristallinem Material niedriger. Die beobachtete Korngrößenabhängigkeit des Wirkungsgrades von Solarzellen spiegelt den großen Einfluss der Korngrenzrekombination wieder.

Modellhafte Beschreibung polykristalliner Solarzellen (Kapitel 3). Die über 20 Jahre gesammelte Erfahrung in der Herstellung von polykristallinem Silizium stellt einen sehr reichen Datensatz von Solarzellenparametern unterschiedlicher Korngröße zur Verfügung. Die Abhängigkeit der Solarzellenparameter von der Korngröße ist jedoch bisher nicht vollständig erklärt worden. Bereits vor einigen Jahren wurden Solarzellen aus polykristallinem Silizium mit einer Korngröße unter 1 μm mit 10 % Wirkungsgrad hergestellt. Diese Rekordwerte sind bei solch kleinen Körner schwierig zu verstehen. Diese Arbeit stellt ein Modell vor, das Solarzellenparameter von Zellen mit Korngrößen zwischen 10^{-2} bis 10^{4} μm durch eine Korngrenzrekombinationsgeschwindigkeit S_{GB} erklärt. Das Modell zeigt, dass die hohen Wirkungsgrade der feinkörnigen Zellen nur mit sehr niederen Werten von S_{GB} zwischen 100 und 1000 cm/s zu erklären sind.

Dieses Modell berücksichtigt die Rekombination von Ladungsträger in der Basis *und* in der Raumladungszone (RLZ) der Zellen. Mit der Annahme, dass die Diffusionslänge geringer als die Zelldicke ist, definiere ich eine effektive Diffusionslänge L_{eff}, die sowohl die Rekombination in der RLZ als auch in der Basis beschreibt. Diese Annahme führt zu einer Gleichung, welche die Leerlaufspannung V_{OC} und die Kurzschlussstromdichte J_{SC} mit L_{eff} verbindet. Hiermit erstelle ich also eine Methode, um L_{eff} aus V_{OC} und J_{SC} zu *extrahieren*. Zur Überprüfung dieser Methode vergleiche ich die extrahierten Werte von L_{eff} mit direkt aus der Quantenausbeute (IQE) extrahierten Literaturdaten. Bild 2 zeigt, dass die mit beiden Methoden extrahierten Werte von L_{eff} über einem Intervall von drei Größenordnungen von L_{eff} gut übereinstimmen. Die gestrichelten Linien in Bild 2 stellen die Standardabweichung der Daten von der Geraden $y = x$ dar, die einen Faktor 1.3 beträgt. Wegen der in der Praxis leichten Messbarkeit von V_{OC} und J_{SC}, bietet diese Methode ein einfaches Verfahren zur Abschätzung von L_{eff}.
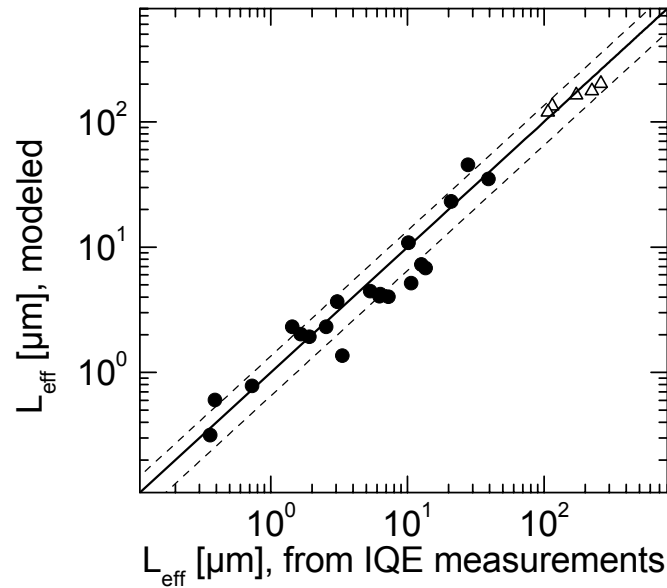
Bild 2. Dieses Bild zeigt die Übereinstimmung der aus der internen Quantenausbeute (IQE) gemessenen Werte der effektiven Diffusionslänge L_{eff} und den aus V_{OC} und J_{SC} extrahierten Werten. Die gestrichelten Linien stellen die Standardabweichung der Datenpunkte von der geraden $y = x$ dar.

Kapitel 3 stellt auch ein zweites Modell zur Extraktion von L_{eff} aus J_{SC} und der Generationsrate in der Zelle vor. Dieses Modell beruht nicht auf der Kennlinie der Zelle, sondern auf der Sammlungsfunktion von Ladungsträgern, die den Beitrag von den lichterzeugten Ladungsträgern zu J_{SC} berücksichtigt.

Des Weiteren benutze ich die vorgestellte Methode zur Extrahierung der Diffussionslänge $L_{eff,poly}$ polykristalliner Solarzellen aus Literaturdaten. Hierzu erstelle ich eine Sammlung von Werten von V_{OC} und J_{SC} polykristalliner Siliziumzellen unterschiedlicher Korngrößen und extrahiere $L_{eff,poly}$. Die Abhängigkeit von $L_{eff,poly}$ mit der Korngröße g ergibt den im Bild 3 dargestellten Zusammenhang. Die Datenpunkte zeigen einen Anstieg von $L_{eff,poly}$ mit der Korngröße. Die feinkörnigen Zellen mit $g < 1$ µm, hier durch Dreiecke dargestellt, sind *pin* Zellen; die *pn* Zellen sind mit Kreisen dargestellt. Die durchgezogenen Linien in Bild 3 stammen von einem Modell, das die Abhängigkeit der Diffusionslänge $L_{eff,poly}$ mit der Korngröße g beschreibt. Als Parameter benutzt das Modell die Rekombinationsgeschwindigkeit S_{GB} an der Korngrenze. Die eingetragenen Kurven zeigen, dass die Zellen mit $g < 1$ µm nur mit $S_{GB} < 1000$ cm/s zu erklären sind, während die grobkörnigeren Zellen meist zwischen $10^5 < S_{GB} < 10^7$ cm/s liegen.

Ursache für die relativ hohe Wirkungsgrade von bis zu 10 % der feinkörnigen Zellen ($g < 1$ μm) sind demnach die niedrigen Werte von S_{GB}. Eine solch geringe Rekombinationsgeschwindigkeit muss durch eine sehr niedrige Dichte von Defektniveaus an der Korngrenze gegeben sein. Dies führt zur Vermutung, dass die feinkörnigen Zellen besondere *strukturelle* Korngrenzeigenschaften haben, die eine geringe Defektdichte ergeben.
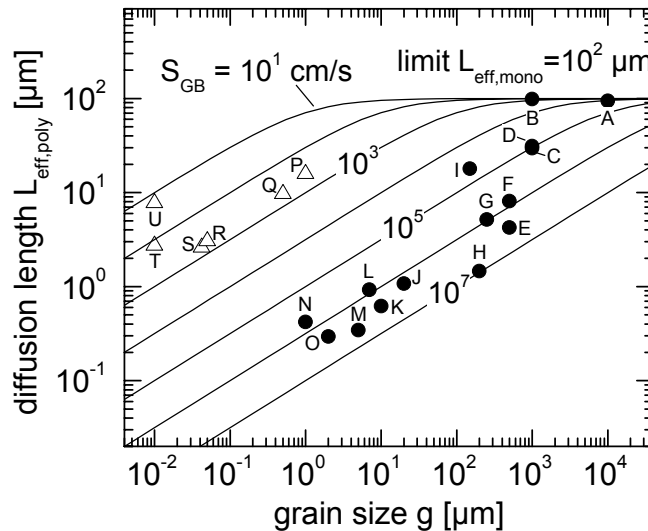
Bild 3. Die aus dem in dieser Arbeit vorgestellten Modell errechneten effektiven Diffusionslängen $L_{eff,poly}$ von polykristallinen Silizium-Solarzellen (Datenpunkte) zeigen eine Abhängigkeit von der Korngröße g. Zur Korngrößenabhängigkeit wird ein Modell aus der Literatur angewandt (Linien), was eine Rekombinationsgeschwindigkeit S_{GB} an der Korngrenze annimmt. Aus dem Bild ersieht man, dass die Zellen mit $g < 1$ μm *nur* durch niedrige Werte von $S_{GB} < 10^3$ cm/s zu erklären sind.

Eine vor kurzem publizierte Arbeit erläutert, dass die feinkörnigen Zellen eine Oberflächentextur in der {220}-Richtung zeigen. Dies führt bei dieser Publikation zur Annahme, dass viele Körner dieser Schichten [110]-Kippkorngrenzen haben könnten. Solche Korngrenzen zeigen insbesondere keine gebrochenen Bindungen und haben daher eine sehr geringe Dichte von Defektniveaus. Diese Überlegung bietet also eine mögliche Erklärung für die geringe Werte von S_{GB}.

Bisher wurde die Rekombination an der Korngrenze durch S_{GB} beschrieben, ohne den Zusammenhang zwischen Defektdichte der Korngrenzzustände und Rekombination zu erläutern. Kapitel 4 vertieft die Beschreibung der Rekombination durch die Untersuchung der *Rekombinationsrate* an der KG. Die Rekombinationsrate ist proportional zu S_{GB} und zur

Überschussladungsträgerkonzentration, wobei S_{GB} proportional zur Defektdichte sein muss.

Analytische Modelle für die elektrischen Eigenschaften von Korngrenzen (Kapitel 4). In diesem Teil der Arbeit beschreibe ich mit einem eindimensionalen Modell eines polykristallinen Halbleiters die Ladung, die Bandverbiegung und die Rekombinationsrate an der Korngrenze. Bei Beleuchtung liefert das Modell zusätzlich noch die maximale Leerlaufspannung V^0_{OC}, die als Obergrenze für die Leerlaufspannung einer Zelle gilt. Diese maximale Leerlaufspannung ist eine Funktion der Korngröße, der Defektdichte, der Dotierung N_A und der Generationsrate G. Bild 4 zeigt die Ergebnisse dieses Modells bei einer Korngröße von 1 µm und einer Defektdichte von 10^{11} cm^{-2}, bei Generationsraten zwischen 0.1 und 10 Sonnen (1 Sonne = 10^{20} cm^{-3}s^{-1}). Wir sehen, dass V^0_{OC} mit der Dotierung und der Generationsrate zunimmt. Solarzellen mit ausschließlicher Korngrenzrekombination müssten also bei Dotierungen $N_A > 5$x10^{16} cm^{-3} Leerlaufspannungen $V_{OC} > 0.5$ V liefern.

Bild 4. Die maximal erreichbare Leerlaufspannung V^0_{OC} einer Solarzelle aus polykristallinem Silizium als Funktion der Dotierung N_A und der Generationsrate G; bei einer angenommenen Korngröße von 1 µm und einer Defektdichte von 10^{11} cm^{-2}. Das Modell nimmt an, dass die Ladungsträger ausschließlich an der Korngrenze rekombinieren und zeigt eine kontinuierliche Zunahme von V^0_{OC} mit N_A. Die Bandverbiegung qV_b hat dagegen ein Maximum, welches sich mit G verändert.

Des Weiteren ersehen wir aus Bild 4, dass die Bandverbiegung an der Korngrenze qV_b ein Maximum bei Dotierungen zwischen 10^{15} und 5x10^{16} cm^{-3} zeigt. Die Bandverbiegung verringert sich mit der Lichtintensität aufgrund der

Neutralisierung der Korngrenzladung durch die lichterzeugten Ladungsträger. Diese Verringerung der Bandverbiegung bedeutet einen leichteren Transport von Ladungsträger von Korn zu Korn und eine geringere Anziehungskraft für Minoritätsladungsträger hin zur Korngrenze. Am meisten profitieren von dieser Eigenschaft dünne Schichten, da hier die Generationsraten am höchsten sind. Dieser Fall ist bei feinkörnigen Dünnschichtsolarzellen gegeben.

Bild 5 zeigt die Zunahme von V^0_{OC} mit der Defektdichte N_t und der Korngröße g, bei einer Dotierung $N_A = 10^{15}$ cm^{-3} und einer Generationsrate G = 1 Sonne. Die kontinuierliche Zunahme von V^0_{OC} mit g führt zu zwei wichtigen Aussagen: für eine erwünschte Zunahme von der Leerlaufspannung von z.B. V_{OC} = 0.1 V muss man entweder die Korngröße g um eine Größenordnung erhöhen, oder die Defektdichte N_{GB} um eine Größenordnung verringern. Der ersten Strategie folgen etwa die Herstellungsverfahren aus denen die grobkörnigen Zellen mit g > 1 μm in Bild 3 stammen. Die zweite Strategie wird durch Zellen mit g < 1 μm verfolgt. Wie ich in der vorliegenden Arbeit zeige, hat außerdem eine Erhöhung der Generationsrate G den gleichen Effekt wie eine Erniedrigung von N_{GB} um eine Größenordnung. Hiermit kann erklärt werden, dass die feinkörnigen Dünnschichtzellen mit hohen Generationsraten von 10 Sonnen eine Leerlaufspannung von etwa 550 mV liefern, sofern die Defektdichte den Wert $N_{GB} = 10^{11}$ cm^{-2} nicht überschreitet.

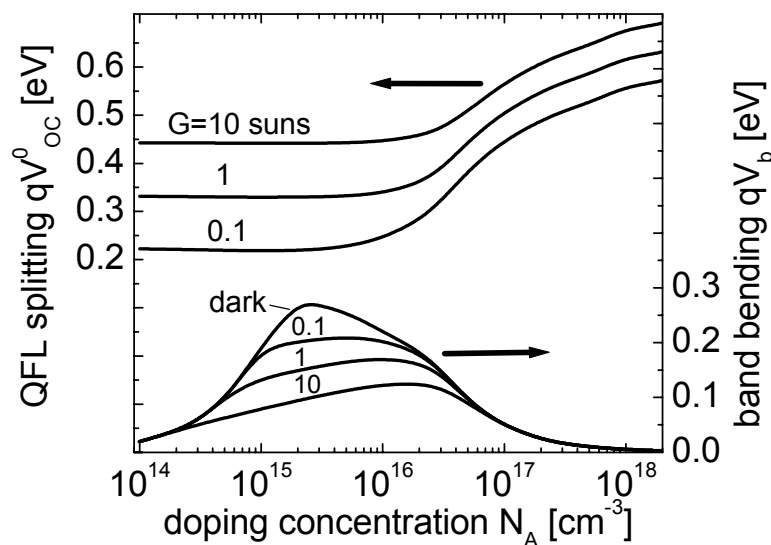
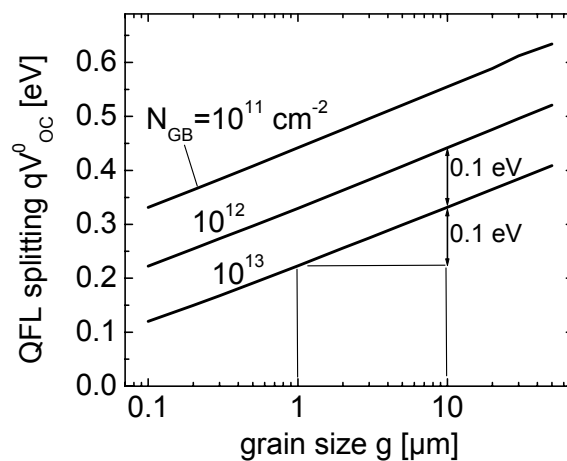Bild 5. Die maximal erreichbare Leerlaufspannung V^0_{OC} einer Solarzelle aus polykristallinem Silizium als Funktion der Korngröße g und der Dichte an Korngrenzdefekten N_{GB} zeigt, dass eine etwaige Zunahme von qV^0_{OC} um 0.1 eV eine zehnfach größere Korngröße erfordert, oder eine zehnfach geringere Defektdichte. Die Dotierung beträgt in diesem Fall $N_A = 10^{15}$ cm^{-3} und die Generationsrate G = 1 Sonne.

Das eindimensionale Modell nimmt nur unkontaktierte Körner an und ermöglicht daher keine Modellierung von Solarzellen. Zur vollständigen Beschreibung polykristalliner Solarzellen entwickle ich ein numerisches Modell.

Numerische Simulation von *pin*-Solarzellen aus mikrokristallinem Silizium (Kapitel 5). Ein numerisches Modell finiter Differenzen in zwei Dimensionen wird zur Simulation von *pin*-Solarzellen erstellt. Hierbei bezeichnet die *i-Schicht* eine sich zwischen zwei hochdotierten Schichten befindender Zwischenschicht, die aber auch dotiert sein kann. Die erste Dimension im Simulationsfeld breitet sich in die Tiefe der Solarzelle aus (von der Vorder- bis zur Rückseite), während die zweite Dimension sich über die Kornbreite erstreckt. Die wichtigste Annahme des Modells ist, dass die Korngrenze senkrecht zur Zellenoberfläche steht. An dieser einzigen Korngrenze im Simulationsfeld befinden sich Defektniveaus, die einer Shockley-Read-Hall Rekombinationsstatistik folgen. Außer der Rekombination an der Korngrenze, nehme ich auch Volumenrekombination und Rekombination an den Kontakten der Zelle an. Die für die Simulationen benötigte Generationsrate wurde numerisch für eine Standardstrahlungsleistung von 100 mW/cm^{-2} bei einem AM1.5 Sonnenspektrum und mit dem Absorptionskoeffizienten von Silizium berechnet. Bild 6 fasst die Ergebnisse der Simulationen durch die Abhängigkeit von Leerlaufspannung und Wirkungsgrad von der Dotierung der i-Schicht zusammen. Die Kreise gehören zu Simulationsergebnissen bei einer Korngrenzdefektdichte von $N_{GB} = 10^{11}$ cm^{-2} mit unterschiedlicher Rekombinationsgeschwindigkeit S_C an den Kontakten.

Bei niedrigen Rekombinationsgeschwindigkeiten an den Kontakten von $S_C = 10^2$ cm/s zeigen die Simulationen einen Anstieg von V_{OC} und η mit der Dotierung der i-Schicht bis zu einem Maximum von $\eta = 15$ %, das bei einer Konzentration von etwa 10^{18} cm^{-3} liegt. Dieses Maximum ist auf die bei hohen Dotierungen einsetzende Auger-Rekombination im Volumen zurückzuführen. Konzentriert man sich auf die Korngrenzeffekte, dann sieht man, dass die Simulationen bei geringem S_C mit dem eindimensionalen Modell aus Kapitel 4 (graue Kurve in Bild 6) übereinstimmen. Die errechnete maximale Leerlaufspannung polykristalliner Solarzellen aus Kapitel 4, das nur unkontaktierte Körner behandelt, ist somit überprüft worden.
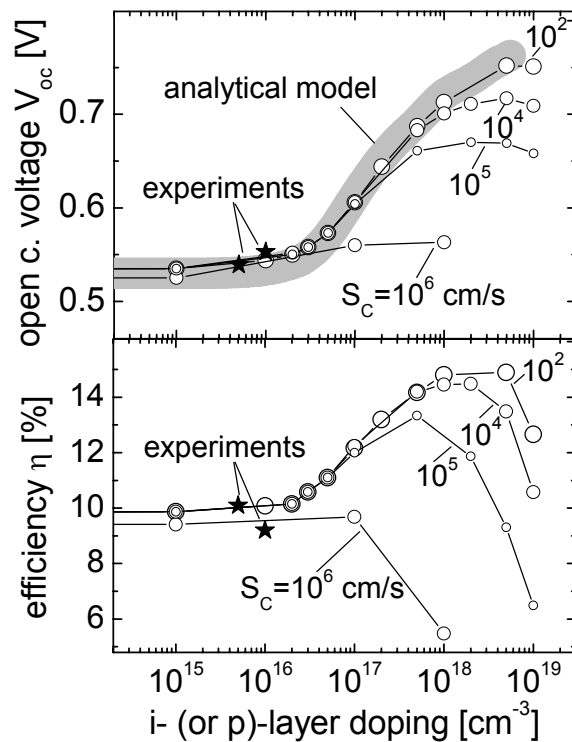
Bild 6. Die aus der zweidimensionalen Simulation errechneten Datenpunkte (Kreise) zeigen, dass Wirkungsgrade von 10 % in *pin*-Zellen mit undotierten i-Schichten und bis zu 15 % bei hohen Dotierungen erreichbar sind. Der Wert η = 15 % kann allerdings nur bei mit niedere Rekombinationsgeschwindigkeiten an den Kontakten unter S_C = 10^4 cm/s erreicht werden. Die Leerlaufspannungen V_{OC} des eindimensionalen Modells (graue Linie) stimmt mit den Simulationen bei niederem S_C sehr gut überein.

Außerdem lässt sich aus den Simulationen errechnen, dass die Rekombinationsgeschwindigkeit S_{GB} an der Korngrenze unter 1100 cm/s liegen muss, um mit *pin*-Zellen einen Wirkungsgrad von 10 % zu erreichen (vgl. Sterne in Bild 6). Dieses Ergebnis stimmt exakt mit den Vorhersagen des Modells von L_{eff} aus Kapitel 3 überein. Hieraus kann gefolgert werden, dass die feinkörnigen Rekordzellen aus der Literatur mit 10 % Wirkungsgrad, zwanghaft eine Korngrenzdefektdichte unter 10^{11} cm^{-2} haben müssen.

Analytisches Modell für die Kennlinie von *pin*-Solarzellen (Kapitel 5). In diesem Kapitel leite ich analytische Ausdrücke für die Dunkel- und Hellkennlinie der *pin*-Solarzelle her. Die Ergebnisse ergeben eine, in der Literatur bisher nicht vorhandene, analytische Darstellung der *gesamten* Kennlinie von *pin*-Zellen und *pin*-Dioden. Das Modell ist eindimensional und basiert auf der Lösung der Kontinuitätsgleichungen in der i-Schicht. Vereinfachenden Annahmen sind die Konstanz des elektrischen Feldes in der i-Schicht, die Flachheit der Quasi-

Ferminiveaus der Majoritätsladungsträger und die Gleichheit von Ladungsträgerlebensdauern und Beweglichkeiten für Elektronen und Löcher. Die Dunkelkennlinien zeigen Analogien zur bekannten Kennlinie der *pn*-Zelle mit Rekombination in der RLZ: ist die Diffusionslänge gering, so ergibt sich ein Idealitätsfaktor von n_{id} = 1.8, was vergleichbar mit dem Wert n_{id} = 2.0 des Rekombinationstromes in der RLZ einer *pn*-Diode ist. Bei höheren Diffusionslängen ist das bei *pn*-Dioden bekannte Doppeldiodenverhalten zu sehen: bei niederen Spannungen ergibt sich ein Idealitätsfaktor n_{id} = 1.8, während bei höheren Spannungen der Wert n_{id} = 1.2 vorkommt, was ähnlich zu dem Wert von n_{id} = 1.0 in *pn*-Zellen bei hohen Spannungen ist. Kapitel 5 diskutiert weitere Analogien zwischen *pn*- und *pin*-Dioden.

Unter Beleuchtung ergibt das analytische *pin*-Diodenmodell eine starke Abhängigkeit zwischen dem eingebauten elektrischen Feld und dem Kurzschlussstrom der Zelle. Die starke Abhängigkeit zwischen Feld und Kurzschlussstrom erlaubt eine recht einfache Quantifizierung der feldbedingten Ladungsträgersammelwahrscheinlichkeit von *pin*-Zellen.

Das neue, analytische *pin*-Diodenmodell erlaubt auch eine Beschreibung der Abhängigkeit des Wirkungsgrades η von *pin*-Solarzellen und vom Produkt µτ aus Beweglichkeit und Lebensdauer. Bild 7 zeigt diese Abhängigkeit bei Dünnschichtzellen aus feinkörnigem Silizium (Datenpunkte) und die Anpassung durch das Modell mittels zweier verschiedener Zellendicken *W*. Wie aus Bild 7 zu sehen ist, bietet das Modell eine sehr gute Anpassung an die Daten und stellt somit die erwünschte analytische Beschreibung der *pin*-Zelle dar. Dieses Modell dient auch im nächsten Kapitel zur Charakterisierung von Test-Dioden aus laserkristalliertem Silizium.
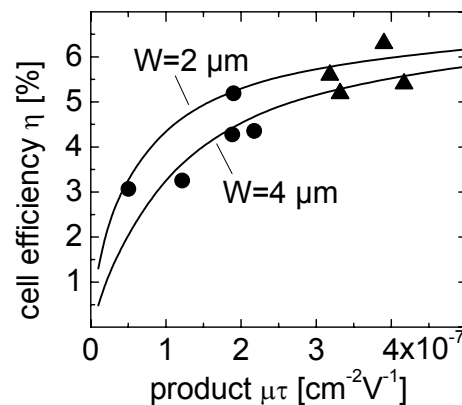
Bild 7. Die Abhängigkeit des Wirkungsgrades η von *pin*-Solarzellen vom Produkt μτ aus Beweglichkeit und Lebensdauer aus Literaturdaten (Datenpunkte) wird durch das analytische pin-Diodenmodell mit zwei verschiedener Zellendicken *W* gut angepasst (Kurven).

Laserkristallisiertes Silizium (Kapitel 6). Dieses Kapitel befasst sich mit der Präparation und der optischen und elektrischen Charakterisierung von laser-kristallisiertem Silizium. Die oft erreichte hervorragende elektronische Qualität dieses Materials ist aus der hohen Feldbeweglichkeit von Feldeffekttransistoren bekannt, die aber Bauelement- und Schichteigenschaften zusammenfasst. Die elektronischen Eigenschaften des Materials selbst sind aus der Feldbeweglichkeit von Feldeffekttransistoren nicht zu extrahieren. Zielsetzung dieses Kapitels ist daher eine elektrische Charakterisierung laserkristallisierten Schichten zu bieten, die Werte von Transportparametern in den Schichten liefern soll. Messungen des Ladungsträgertyps, des Hall-Effekts, der temperaturabhängigen Leitfähigkeit und der Photoleitfähigkeit wurden dazu durchgeführt und analysiert.

Zur Isolierung gegen atomarer Diffusion zwischen den zu kristallisierenden Schichten und Substrat werden Silizium-Nitrid Pufferschichten benutzt, auf denen die Siliziumschichten deponiert und kristallisiert wurden. Für die elektrischen Charakterisierungen werden auf den kristallisierten Schichten Metallkontakte aufgedampft. Die Messungen des Leitungstyps ergeben eine leichte p-Typ-Leitfähigkeit, die auf eine hohe n-Typ-Kompensation durch Verunreinigungsdotieratome zurückzuführen ist. Die Schichten zeigen eine starke Abhängigkeit der Leitfähigkeit von der Stromrichtung: parallel zur Scanrichtung des Lasers, ist die Leitfähigkeit bis zu 100-fach höher als senkrecht zur Scanrichtung. Dieses Ergebnis demonstriert, dass der Transport von Majoritäten

tatsächlich durch Korngrenzen dominiert ist, weil das Verhältnis von Kornlänge zu Kornbreite etwa den Wert 100 zeigt. Die Leitfähigkeit senkrecht zur Scanrichtung liegt in der Größenordnung von 10^{-4} Ω^{-1}cm^{-1}. Der Hall-Effekt liefert Beweglichkeiten zwischen 12 und 120 cm^2/Vs und eine mittlere Ladungsträgerkonzentration zwischen 4×10^{12} und 4×10^{13} cm^{-3}. Diese niedrige Konzentration entspricht einer Lage des Ferminiveaus tief in der Bandlücke. Aus der Messung der temperaturabhängigen Leitfähigkeit ergibt sich folgerichtig, dass das Ferminiveau etwa in der Bandlückenmitte sitzt. Die errechnete Bandverbiegung an den Korngrenzen liegt bei etwa 120 meV mit einer Barriereninhomogenität von 80 mV. Eine solche Bandverbiegung ergibt eine Defektdichte an den Korngrenzen von $N_t \geq$ 1.6×10^{10} cm^{-2}. Diese niedrige Defektdichte spiegelt sich auch in dem hohen Wert des $\mu\tau$-Produkts von $\mu\tau = 2.3 \times 10^{-5}$ cm^2/V aus der Abhängigkeit der Photoleitfähigkeit mit der Korngröße wider. Der hohe Wert des $\mu\tau$-Produkts spricht für eine gute elektrische Qualität der Schichten, die sich bisher nur durch die hohen Feldbeweglichkeiten der Feldeffektransistoren abschätzen ließ.

Der letzte Teil des Kapitels 6 beschreibt die Präparation und Charakterisierung von Test-Dioden aus laserkristallisierten Siliziumschichten. Diese Schichten sind auf einer dünnen Chromschicht kristallisiert, die den Rückkontakt der Diode bildet. Die gemessenen Kennlinien lassen sich durch das Modell der Kennlinie von *pin*-Dioden aus Kapitel 5 anpassen und ergeben eine eingebaute Spannung von 0.49 V und ein $\mu\tau$-Produkt von $\mu\tau = 4 \times 10^{-6}$ cm^2/V. Eine Übereinstimmung mit den Werten des $\mu\tau$-Produkts aus der Photoleitfähigkeit ist nicht zu erwarten, weil die Test-Dioden nicht auf Silizium-Nitrid, sondern auf einer Chromschicht kristallisiert sind.

Die hier erwähnten Charakterisierungen ergeben zum ersten Mal einen vollständigen Blick auf die elektrischen Eigenschaften von laserkristallisiertem Silizium. Die hohen Werte des $\mu\tau$-Produkts weisen darauf hin, dass weitere Untersuchungen der Minoritätsladungsträgereigenschaften sinnvoll wären. Solche Untersuchungen sollten sich mit der Frage befassen, ob sich laserkristallisiertes Silizium ausschließlich für Feldeffektransistoren eignet, oder ob es auch für Minoritätsladungsträgerbauelemente wie Solarzellen oder Bipolartransistoren geeignet ist.

1 Introduction

Since about 20 years, the market of photovoltaic products shows an annual growth of 15-20 % [1], and reached a remarkable 40 % growth in 2001 [2]. Despite this high increase of its production volume, photovoltaics is still far from being a common energy source. As pointed out by Goetzberger and Hebling [1], the main reason for this low market impact of photovoltaics is the high cost of photovoltaic modules, and the resulting high price per Watt solar energy.

About 85 % of the modules produced in the world are based on silicon *wafers*, i.e. on silicon slices cut off from ingots [2]. The ingots require expensive and energy-intensive preparation processes, requiring 13 KWh/Kg already to reduce silicon from quartzite [3] (without counting purification steps). In addition, the process of cutting off the wafers is accompanied by a 30 % of material loss [1], rising the cost per wafer. Thus, using as less silicon as possible is a mandatory condition to fabricate cheap photovoltaic products.

An additional reason for a low acceptance of wafer-based photovoltaics, is the unclear balance between the *negative environmental impact* associated to the fabrication of the silicon wafers, and the *environmental relief* offered by the module in its lifetime. A recent study shows that, if the ingots were obtained using non-ecological sources of electrical energy, like coal combustion, then the environmental relief (in terms of CO_2 and SO_2 emissions) offered by the photovoltaic module in its lifetime would be negligible [4]. Fortunately, silicon is obtained in countries where the electricity comes from sources that are less stressful for the environment than coal combustion. However, the wafer-based technology still comprises the drawback of needing large amounts of non-renewable energy, downgrading the ecological value of photovoltaics.

A possible solution to both, the economical and the ecological shortcomings of Si-based photovoltaics, would be to reduce drastically the amount of silicon needed for the production of a solar cell [4]. This idea led to thin-film (TF) photovoltaics, which uses Si *films* instead of wafers. The TF technology does not use ingots, it is

based on the deposition of silicon onto a substrate from the vapor phase. With a thickness between 1 and 20 μm, the films are one to two orders of magnitude thinner than the 300 μm thick wafers, achieving the required material saving. Therefore, a number of promising techniques to prepare low-cost TF silicon cells, like the chemical vapor deposition and the physical vapor deposition, are currently under development [5].

Though material consumption is reduced by TF technologies, the TF approach brings up new questions about its usability for low-cost applications. Unlike wafers, thin films prepared directly on low-cost substrates are polycrystalline. Due to grain boundaries and intra-grain defects, the recombination of carriers increases, reducing the electronic quality of polycrystalline Si compared to monocrystalline silicon. In order to overcome this problem, the direction followed by the research groups was either to:

1. increase the grain size, reducing the amount of harmful grain boundaries per unit volume, or

2. to reduce the recombination at the grain boundaries without caring about the grain size.

As pointed out by Catchpole et al. [5], approach 1 does not help from the economical point of view, because the techniques to increase grain size involve high-temperature processes that need heat-resistant substrates, which result in expensive cells. There is, however, one method that yields large grains using cheap substrates: the laser-crystallization method. Even cheap plastic substrates may be utilized as support for the silicon film [6]. The laser-crystallization uses a thin film of amorphous silicon deposited onto a substrate, which is melted and crystallized by a laser pulse. Since the crystallization takes place in a very short time interval, no heat-resistant substrate is needed. The resulting TF polycrystalline silicon shows excellent properties for applications that use small to medium areas such as TF transistors [7]. The application of this technique to large area technologies, such as photovoltaics, is still subject of investigations.

The second approach, based on the reduction of the recombination of carriers at grain boundaries, is less intuitive than the first one. By tweaking the preparation

conditions, some research groups [8] managed to produce a polycrystalline silicon from the vapor phase that shows relatively high open circuit voltages of 553 mV, indicating low recombination activity in their films. They even prepared these films using low-temperature processes and cheap, large-area glass substrates. Using their technique, laboratory-scale cells with 10 % efficiency were prepared a few years ago [8], which is a high mark considering the small grain sizes between 10^{-2} and 1 μm that result with this technique.

The first and second approaches, led to films with grain sizes ranging from 10^{-2} to 10^4 μm. There is therefore a considerably large experimental basis to obtain several types of TF silicon. However, there is little theoretical knowledge that explains the influence of grain size on cell efficiency. It is only understood that, for example, the open circuit voltage (and therefore the efficiency) of solar cells increases with grain size (See Refs. [9] and [10]). But the model of Ref. [9] cannot be utilized to fit a broad set of solar cell data, because it neglects a possible simultaneity of space-charge region and neutral region recombination. Furthermore, the model of Ref. [9] considers films with grain boundaries perpendicular *as well as* parallel to the plane of the film, which is not the case of the cells obtained with the new preparation techniques. When using the model of Ref. [10] to fit the data, we have to assume the same proportion of space-charge region and neutral region recombination for all cells under study, an assumption that cannot be made when fitting data of cells with different grain sizes and preparation techniques.

Another complication is the *np-* versus *pin*-type cell dilemma: the cells with 10 % efficiency mentioned above use a *pin*-structure, while other cells succeed only with *pn*-structures. Since there is no simple equation to the current/voltage characteristics of *pin*-cells, most debates about the convenience of *np* or *pin*-structures lack a solid theoretical basis.

There are cases where even the electronic properties of bare films are still unknown. In particular, the laser-crystallization technique succeeded in the thin film transistor technology, but surprisingly, most of the electronic properties of the basic material are unknown. The material for the transistors has always been qualified by the channel mobility of the transistors, which depends not only on the

material's transport parameters, but also on the shape and sizes of the transistor. Little is known about the transport parameters of the material itself, making its application to other fields than transistor technology unpredictable.

The aim of the present work is to shed some light on the aspects mentioned above, by giving answers to the following questions:

1.   Is it possible to understand the observed increase in cell efficiency with grain size (over the whole range of grain sizes obtained by the polycrystalline silicon technology), by modeling the grain size dependence of the cell's open circuit voltage and short circuit current?

2.   What role plays the adoption of a np/pin structure on cell efficiency? Which of these two structures is better suited for a material with large/small grains, and which one for high/low grain boundary recombination activity? Is it possible to beat the 10 % efficiency mark [8] reached with small-grained materials just by using a pn- instead of a pin-structure?

3.   What are the electronic properties of laser-crystallized silicon? What are the values of the conductivity and the minority carrier lifetime? Is it possible to prepare a good solar cell based on laser-crystallized Si?

I treat each of these questions in the following five chapters.

Chapter 2 gives the definitions and equations to model the electrical behavior of a semiconductor device. Furthermore, the chapter provides a qualitative explanation of the electrical behavior of grain boundaries. Finally, I briefly explain how a solar cell works, and show the specific features that appear in a polycrystalline solar cells.

Chapter 3 presents a one-dimensional model to explain the grain size dependence of the photovoltaic output parameters of np-type solar cells. The model considers only two parameters: the grain size, and the recombination velocity at grain boundaries. The recombination velocity is then treated in detail considering the density of defects at the grain boundary in Chapter 4, which gives also simple

models to the electrical properties of polycrystalline silicon *films*, such as the conductivity of polycrystalline films, needed in Chapter 6.

Chapter 5 presents a numerical model that simulates solar cells in two dimensions. The chapter establishes conceptual bridges to the models of Chapter 3 for solar cells as well as to the models for thin films given in Chapter 4. To provide a more simple tool for the analysis of *pin* diodes and cells than the numerical simulations, I develop a new, analytical model for the current/voltage characteristics of *pin*-type structures, and use it to fit experimental data.

Finally, I introduce the preparation and characterization of laser-crystallized silicon, in Chapter 6. The interpretation of the measurements of electrical properties are made using the models from the previous chapters.

2 Fundamentals

The electronic behavior of any semiconductor device is explained by modeling the transport, generation and recombination of charge carriers in the device. Solar cells need, additionally, knowledge of the interaction between the semiconductor and light. In a solar cell, light photons generate electron-hole pairs, increasing the carrier concentrations, and therefore affecting the charge distribution and the electronic transport in the device. We can therefore obtain the electrical output characteristics of any solar cell by modeling the charge transport and the interaction of the semiconductor with light. This chapter gives the fundamentals needed to explain the electrical characteristics of semiconductor devices, focusing on polycrystalline semiconductors and solar cells.

2.1 Charge transport in semiconductors

In most semiconductor devices, three gradients cause carrier movement: the gradient of the electrostatic potential, and the two gradients of carrier concentrations. The local charge density determines the electric field. Considering a one-dimensional system with the spatial coordinate x, Poisson's equation relates the electric field F to the charge density ρ by

$$\frac{dF}{dx} = \frac{\rho(x)}{\varepsilon_s},$$

(2.1)

where ε_s is the absolute dielectric constant of the semiconductor. The electric field F is related to the electrostatic potential ψ by $F = -d\psi/dx$. To determine $\rho(x)$, we need to know the net local charge, which is determined by the concentrations of mobile and fixed charges. The mobile charges are given by the free electron concentration n, and the free hole concentration p. The fixed charge is constituted by ionized dopant atoms, and by defects that get charged after they capture or emit carriers from or into the semiconductor's bands. The ionized donor dopants (positive), have a charge concentration N_D^+, and the ionized acceptors (negative), a concentration N_A^-. Deep defects have negative or positive charges, described by n_t and p_t, respectively.

The sum of the above charges define $\rho(x)$ by

$$\rho(x) = q\left(p - n + p_t - n_t + N_D^+ - N_A^-\right),\tag{2.2}$$

where q is the elementary charge. The densities p and n depend on the valence band energy E_V and the conduction band energy E_C respectively, and the quasi-Fermi levels E_{Fp} and E_{Fn} (QFLs) of both type of carriers. The densities p_t and n_t depend on E_V and E_C respectively, and the energy E_T of the traps. Figure 2.1 shows a band diagram of a semiconductor, indicating the different energies defined up to now.
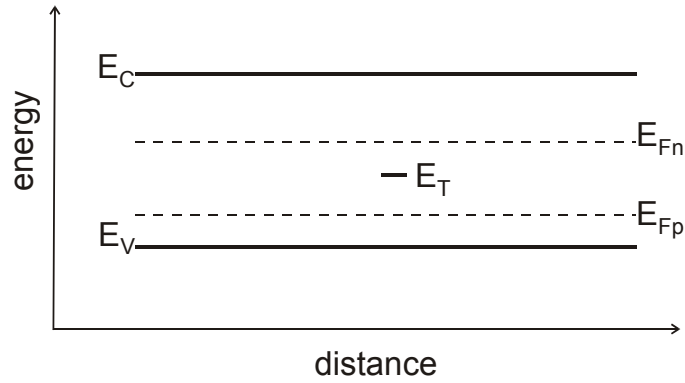
Figure 2.1: Band diagram of a semiconductor out of thermal equilibrium, showing the energies of the conduction and valence band edges E_C and E_V, respectively, the electron and hole Quasi-Fermi levels E_{fn} and E_{fp}, and a deep defect at the energy E_T.

For the situations of work the doping levels are not high enough to shift the equilibrium Fermi level close to the band edges. Assuming that $|E_F - E_{V/C}| > 3kT$, where kT is the thermal energy given by Boltzmann's constant k and the absolute temperature T, p and n are written as

$$p = N_V \exp\left(\frac{E_V - E_{Fp}}{kT}\right)\tag{2.3}$$

and

$$n = N_C \exp\left(\frac{E_{Fn} - E_C}{kT}\right),\tag{2.4}$$

where N_V and N_C are the effective densities of states in the valence or conduction band, respectively. Under thermal equilibrium conditions, i.e., in a device, which is neither subjected to excitation nor to an external voltage, but only to the radiation of its surroundings, the QFLs coincide at a unique Fermi level $E_F = E_{Fn} = E_{Fp}$.

The ionized impurity concentrations will be treated as constants throughout this work, namely N_A^- and N_D^+. Moreover, I assume that all impurity atoms are ionized, which is a common assumption that holds for most impurity atoms at room temperature. Thus, $N_A^- \approx N_A$, and $N_D^+ \approx N_D$.

The carrier concentrations at the defect levels, are given by the product between the density N_t of defect states at the energy E_t (within the forbidden gap), and an occupancy function f, yielding

$$
\begin{aligned}
p_t &= N_t f, \\
n_t &= N_t (1-f).
\end{aligned}
\tag{2.5}
$$

Under thermal equilibrium conditions, the occupancy function is the Fermi-Dirac distribution function, given by [11]

$$
f = \frac{1}{1 + \exp\left(\dfrac{E_t - E_F}{kT}\right)},
\tag{2.6}
$$

The occupancy takes the value 1 for a state occupied with an electron, and 0 for an unoccupied state. At a given temperature, any state with $E_t > E_F$ is filled with a hole (or has no electrons), and the states below E_F, are occupied by an electron (the sharpness of this behavior is regulated by the temperature T, the smaller T is, the sharper becomes f). Out of thermal equilibrium, for example when we illuminate a semiconductor or when we inject carriers artificially into it, we need the Shockley-Read-Hall (SRH) distribution f_{SRH}, which is a function of the free carrier concentrations, and the capture cross sections σ_n and σ_p for electrons and holes. The distribution function is given by [12]

$$
f_{SRH} = \frac{\sigma_n n + \sigma_p p_1}{\sigma_n (n + n_1) + \sigma_p (p + p_1)},
\tag{2.7}
$$

where the quantities n_1 and p_1 are defined by

$$
p_1 = N_V \exp\left(\frac{E_V - E_T}{kT}\right),
\tag{2.8}
$$

and

$$
n_1 = N_C \exp\left(\frac{E_T - E_C}{kT}\right).
\tag{2.9}
$$

With equations (2.3) to (2.9), the charge density needed to determine the electric field is completely defined.

The electric field and the gradients of the carrier concentrations define the currents in the semiconductor. The current densities $J_{p,n}$ at the coordinate x are described by the equations [13]

$$J_p(x) = q\mu_p pF - qD_p \frac{dp}{dx} = \mu_p p \frac{dE_{Fp}}{dx}, \tag{2.10}$$

and

$$J_n(x) = q\mu_n nF + qD_n \frac{dn}{dx} = \mu_n n \frac{dE_{Fn}}{dx}, \tag{2.11}$$

where μ is the carrier mobility and $D_{n/p}$ the diffusion constant (with the subscripts 'p' for holes, and 'n' for electrons). The component of the currents that contains the electric field, is called drift current. The component containing the concentration gradient of the carrier density is the diffusion current. These equations give the electrical current considering positive charges. The flow of electrons seen as particles is in the opposite direction as predicted by J_n from (2.10).

The diffusion and drift processes are linked by the Einstein relation, which establishes that

$$D_{n/p} = V_t \mu_{n/p}, \tag{2.12}$$

where V_t is the thermal voltage, given by $V_t = kT/q$.

2.2 Generation and recombination

Defining the electron-hole generation rate by G, and the recombination rate by R, the local continuity under steady state establishes the relationships [13]

$$\frac{dJ_p}{dx} = q(G - R), \tag{2.13}$$

and

$$\frac{dJ_n}{dx} = -q(G - R). \tag{2.14}$$

The next section explains how to obtain the generation and recombination rates.

2.2.1 Generation rate

The absorption of radiation in any material is given by the Lambert-Beer law, which predicts that at a given wavelength, the radiation is absorbed in such a way that the photon flux ϕ_{phot} decays exponentially from the surface towards the bulk of the material obeying the equation

$$\phi_{phot}(x) = \phi_0 \exp(-\alpha x), \qquad (2.15)$$

where x is the spatial coordinate measured from the surface facing to the light source towards the bulk, ϕ_0 the photon flux at $x = 0$, and α the semiconductor's wavelength-dependent absorption coefficient. The generation rate contained in Eqs. (2.13) and (2.14) is the rate determined by all external energy sources that generate electron-hole pairs, barring the 300 K black-body radiation of the semiconductor's environment. For solar cells, the rate G must be calculated from the spectrum and intensity of the sunlight, the absorption coefficient α of the semiconductor, and the optical properties of all surfaces between the absorbing layer and the surroundings. In this work, I calculate the generation rate in different ways, depending on the case under study. For exact solutions, I obtain G by numerical simulations that consider the exact absorption coefficient of the semiconductor, reflections and dispersions at surfaces, and the experimental values of the solar spectrum. Within analytical models, I take simplified expressions and values for G that are simple to handle. In that case, the values or expressions for G will be explained later.

2.2.2 Recombination rate

The recombination rate R describes the process by which the concentrations of electron-hole pairs return to their values before generation. The most important recombination mechanisms in semiconductors are

- the radiative recombination,

- the Auger-recombination, and

- the recombination *via* defect levels.

The total recombination rate R that results from all this mechanisms is given by the sum

$$R = R_{radiative} + R_{Auger} + R_{defects}. \qquad (2.16)$$

The radiative recombination $R_{radiative}$ is given by [14]

$$R_{radiative} = B\left(np - n_i^2\right),$$
(2.17)

where B is a constant that depends on the material, and n_i is the intrinsic carrier concentration. The Auger recombination rate R_{Auger} depends on two constants C_p and C_n, via the equation [14]

$$R_{Auger} = C_p\left(p^2n - p_0^2 n_0\right) + C_n\left(n^2 p - n_0^2 p_0\right).$$
(2.18)

Regarding the recombination rate $R_{defects}$ at defect levels, one has to consider that in general, there are several recombination levels in the band gap, or even a uniform distribution of defect levels. Every level has its energy E_t, density N_t and capture cross-sections σ_p, σ_n. The capture cross sections reflect the probability for a carrier to be captured by a given defect level. The expression of the recombination rate $R_{defects}$ at defect levels that I use in this work is the Shockley-Read-Hall recombination rate R_{SRH}. Considering defect levels of concentration N_t serving as recombination paths, the total recombination rate is given by [12]

$$R_{defects} \approx R_{SRH} = \sum_{k=1}^{N} \frac{np - n_i^2}{\tau_{0p,k}\left(n + n_{1,k}\right) + \tau_{0n,k}\left(p + p_{1,k}\right)},$$
(2.19)

where τ_{0p} and τ_{0n} are capture-emission lifetimes defined by

$$\tau_{0p} = \frac{1}{v_{th}\sigma_p N_t},$$
$$\tau_{0n} = \frac{1}{v_{th}\sigma_n N_t}.$$
(2.20)

From Eqs. (2.19) and (2.20), we see that the larger the defect density or the capture cross-sections, the larger is the recombination rate $R_{defects}$. The recombination rate describes two different situations:

i. the recombination at a surface (or interface), in which case N_t is given in cm^{-2}, and R in cm^{-2}s^{-1}, and

ii. for bulk recombination, the concentration of defect levels N_t is given in cm^{-3}, and R in cm^{-3}s^{-1}.

For silicon devices, especially those having low-quality material, it is sufficient to calculate the total recombination rate with R_{SRH} only, neglecting the radiative and Auger components . Therefore, I use the complete expression for R

given by (2.16) only within numerical modeling, and assume $R = R_{SRH}$, given by (2.19), within analytical models.

2.2.3 Definitions

It is convenient to define the recombination velocity S, the recombination lifetime τ and the diffusion length L, because these are quantities commonly used in analytical models. Assuming recombination of carriers taking place at a surface of a p-type semiconductor, the recombination velocity for electrons is defined by

$$S_n = \frac{R}{n - n_0}.$$

(2.21)

An analogous expression holds for the recombination velocity S_p of holes at the surface of an n-type semiconductor by replacing n by p and n_0 by p_0 in Eq. (2.21).

The recombination lifetime for minority carriers is defined as the ratio between excess carriers and the recombination rate. In a p-type semiconductor, the recombination lifetime τ_n of electrons is given by

$$\tau_n = \frac{n - n_0}{R},$$

(2.22)

being the analogous equation valid to calculate τ_p in a n-type material. These lifetimes define the diffusion length of minority carriers within a semiconductor. The diffusion length determines the quality of a solar cell, because it combines transport and recombination parameters, namely the carrier lifetime defined by (2.22) and the diffusion constant. The diffusion lengths L_p, L_n for holes and electrons, are defined by the equations

$$L_p = \sqrt{D_p \tau_p},$$
$$L_n = \sqrt{D_n \tau_n}.$$

(2.23)

2.3 Polycrystalline silicon

Grain boundaries are interfaces that separate two regions or grains of a solid, which have different crystallographic orientations. At a grain boundary (GB), the crystal lattices of both regions do not match perfectly. The resulting mismatch originates several crystallographic defects, such as vacancies, bended, strained and broken bonds, and dislocations, which constitute the GB. Additionally, impurity

atoms tend to diffuse to the GBs, where they are retained. Hence, the impurities also increase the defect density at the grain boundaries [15]. All these crystallographic imperfections originate electronic defects, which have energy levels in the energy gap of the semiconductor (See Refs. [15] and [16]). Every defect has its own energy E_t, capture cross sections, and density N_t (given in cm^{-2}).

The band diagram at the grain boundary shows several defect levels distributed over the energy within the band gap. Thus, if the variety and density of defects is high, one usually finds a continuous distribution of defect levels. Such distributions were measured in polycrystalline silicon by Hirae [17], de Graaf et al. [18], and Werner and Peisl [19]. Grovenor pointed out, however, that the presence of discrete levels, or a continuous distribution, could be induced by the measurement technique [20]. Atomistic simulations of grain boundaries in silicon showed that the defect distributions are continuous, and that levels lying deep in the gap form a sharp defect density peak [21]. In order to explain the electrical properties of polycrystalline silicon, however, it is sufficient to model the grain boundary using one or a few defects around the center of the band gap. Indeed, theories that consider only one defect level at the GBs succeeded in explaining the doping dependence of the hall mobility and conductivity in polycrystalline silicon, as shown for the first time by Kamins [22] and Seto [23]. In this work, I also make use of this simplification.

The defect levels at grain boundaries behave as traps for free carriers. The trapping behavior varies from material to material. There are basically five types of grain boundary trapping behaviors [24]. In silicon, the defect states trap electrons as well as holes; if it is n-type, the GBs will predominantly trap electrons, and holes if p-type [24]. In either case, the trapped carriers build up a charge Q_{GB} at the grain boundary, which is positive in p-type, and negative for n-type silicon.

The charging of the traps at the grain boundary implies a removal of free charges from the grain, leaving space-charge regions near the GBs. The charge density of the SCRs is given by the density of dopant atoms. Figure 2.2a, depicts this situation for a p-type material, showing the positive GBs, and the negative SCRs surrounding the GBs. The charge neutrality condition establishes the width of the SCR. In the SCR, we have an electric field, which bends the energy bands at

each side of the GB (similarly to a double metal-semiconductor contact). If we plot the band diagram along the line AA shown in part a) of Figure 2.2, we obtain the scheme of part b). There we see that at the grain boundary, we find many defect levels at different energies. Obeying the Fermi-Dirac statistics, all levels above the Fermi energy level E_F are charged positively. The diagram also shows the band bending qV_b, developed along the SCRs.

(a)

(b)
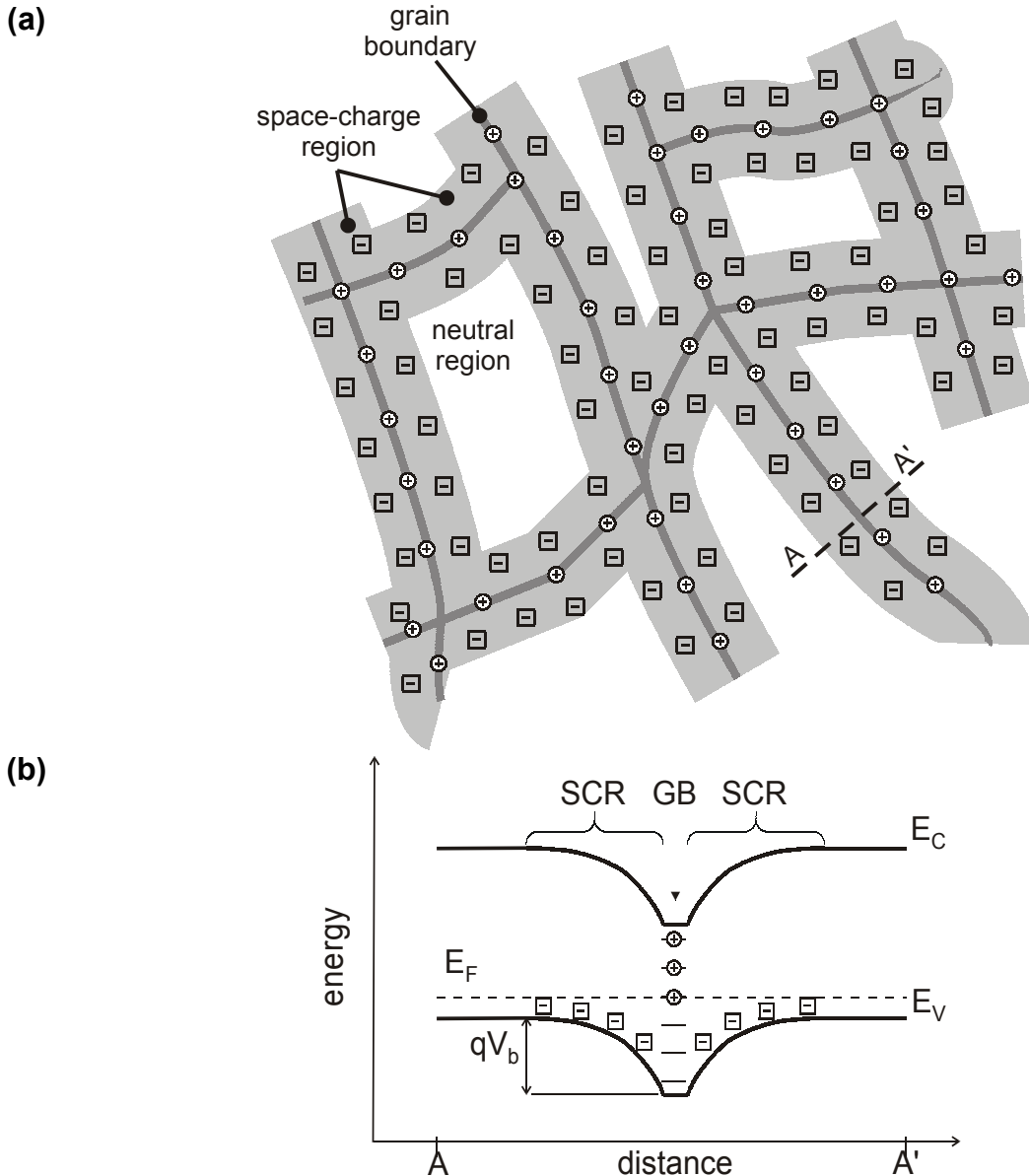
Figure 2.2: Part a) shows a schematic cross section of a p-type polycrystalline semiconductor, showing charges at the grain boundaries, and the space-charge regions that surround them. Part b) shows the band diagram along the line AA' depicted in part a), which contains a grain boundary with its defect levels in the band gap, partially filled with holes. Far away from the grain boundary, the energy of the Fermi-level E_F lies closer to the valence band, corresponding to the p-type nature. The electric field present in the space-charge region bends the band diagram downwards, with a band bending qV_b. This figure also defines the width W of the space-charge region, and the width δ of the grain boundary.

The band bending has two consequences for carrier transport and recombination. Figure 2.3 shows that *majority carriers* (holes in this case) that flow from grain to grain, must overcome a potential barrier. Kamins pointed out that the sole presence of a GB, i.e. neglecting potential barriers, perturbs the carrier flow from one grain to the next one because of the disorder and discontinuity of the crystal lattice found there [25], and the impurity atoms that diffused into the GB. The effect seen externally is an increase of the resistivity of the material. Under illumination, *minority carriers* suffer from the GB barriers, because they act as sinks for electrons (see Figure 2.3). Once they reach the grain boundary, they recombine *via* the defect levels. The external effect, for example, is an increase of the diode saturation current, and as a consequence a decrease in the open circuit voltage of a solar cell.
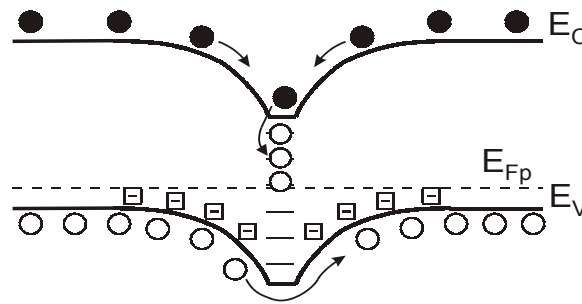
Figure 2.3 The flow of majority carriers (holes in this case) between to grains, is hindered by the potential barrier developed in the space-charge regions. This implies an increase in the resistivity of the material. For minority carriers (electrons), the potential barrier acts as a sink, enhancing the trapping and recombination of electrons through the defect levels at the grain boundary.

2.4 Solar Cells

2.4.1 Basic concepts

Solar cells convert the electromagnetic energy contained in the sunlight into electrical energy. This conversion involves basically three steps: the absorption of light, which implies the generation of excess carriers, the separation of the excess carriers, and finally the delivery of the collected carriers to the consumer or load. In practice, the absorption of light takes place within a semiconducting material. Commonly, the element that separates the carriers generated in the absorbing layer is an *np-* or *pin-* or *nip*-type junction, which is achieved by doping the absorbing

layer with donors (forming the *n*-side), and acceptors for the *p*-side. Special electrical contacts to the *n* and *p*-sides of the cell drive the generated carriers outside the cell.

Figure 2.4 shows cross sections of two basic types of solar cells. In part (a), we see an *np*-type solar cell connected to an external load. The curved arrows represent the path followed by a photon-generated electron (solid circle) and the corresponding hole (open circle). The junction separates carriers by its type, sweeping electrons towards the n-region, but retaining holes in the p-region. The *np* junction has fixed charges on each side, which cause a local electric field that separates the electrons from the holes. After separation, the carriers drift to the contacts. The contacts permit the flux of carriers from the cell to the external circuit. To enhance the optical generation in the cell, the front contact is transparent, and the back contact is reflecting.
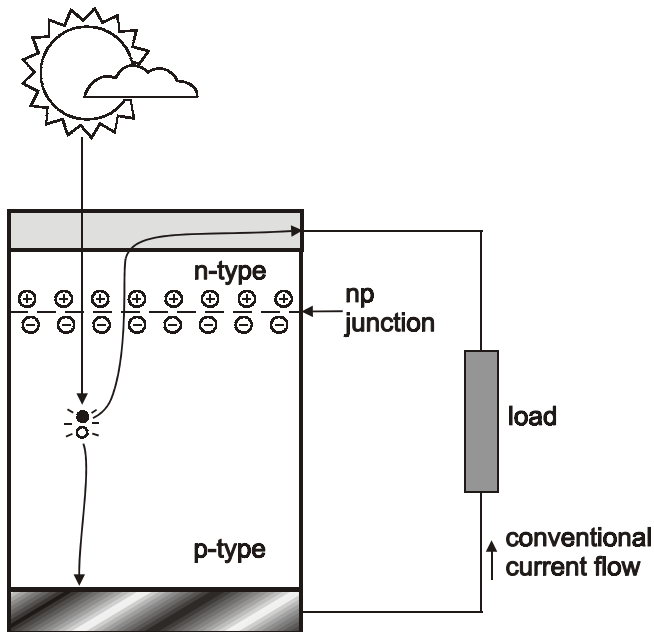
(a) np-type solar cell   (b) pin-type solar cell
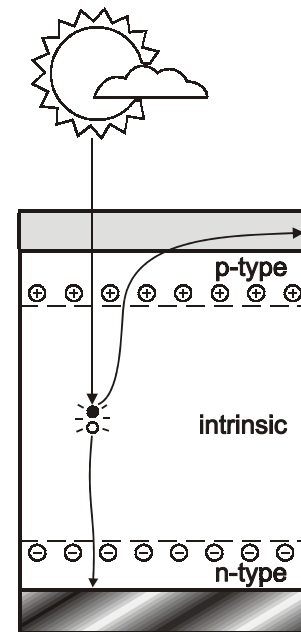
Figure 2.4: In part (a), we see an *np*-type solar cell connected to an external load. The *np*-junction separates the carriers that were generated by the light and diffused to that region without recombining. The generated carriers are extracted by a transparent front-side contact, and a reflecting back contact. Part (b) shows a *pin*-type cell. The electric field in the i-layer separates the carriers, driving them to their respective contacts.

We note that when using an *np*-type cell, the diffusion length must be long enough for all the carriers to reach the junction without recombining. After Eq. (2.23), high diffusion lengths require high recombination lifetimes and high

diffusion constants. In practice, the parameter that drastically influences the diffusion length is the lifetime, because it varies by orders of magnitude depending on the preparation process of the material, its structural perfection, and the recombination at grain boundaries, if the material is polycrystalline. In high-purity, monocrystalline Silicon, the density of recombination centers is so low that diffusion lengths of the order of 1 mm are achieved.[1] Part (b) of Figure 2.4 shows a *pin*-type cell. The intrinsic layer is the thickest layer of the cell, where most of the carriers are light-generated. The two space charge regions separated, originating a constant electric field in the *i*-layer. The electric field separates the carriers, driving them into their respective contacts. In a *pin*-type cell, the collection of a carrier depends on the diffusion length but also on the electric field, which depends on the applied voltage.

Figure 2.5 shows the band diagrams under thermal equilibrium of a *np* cell (part a) and a *nip* cell (part b), indicating the Fermi-level E_F and the built-in voltage V_{bi} in each case. Below each band diagram, we see the electric-field profiles, with the maximum electric field F_{max}.
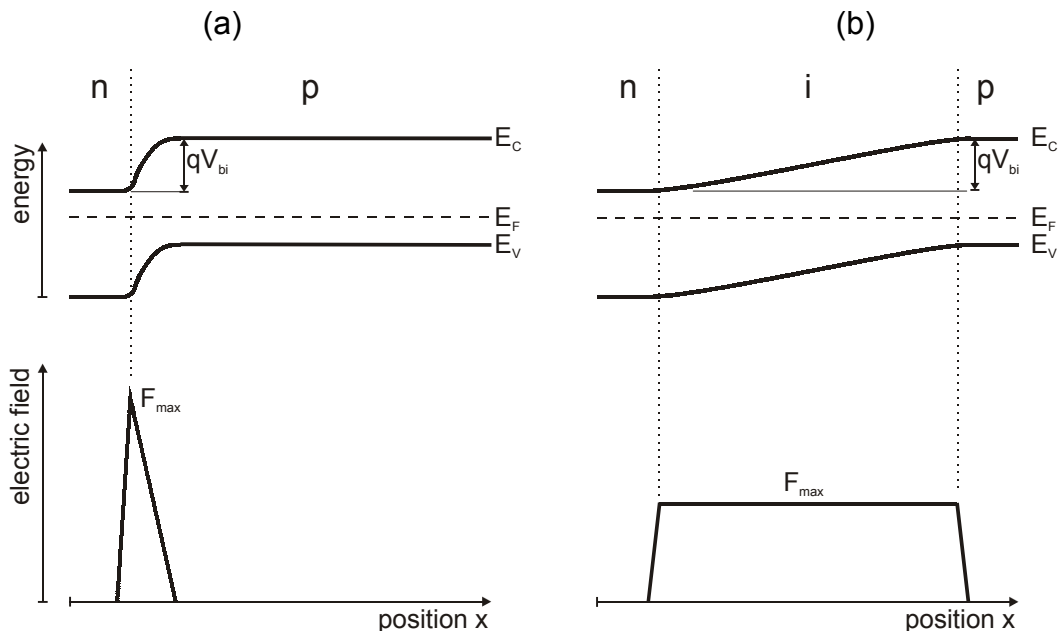
Figure 2.5: Thermal equilibrium Band diagram of a *pn* cell (part a) and a *pin* cell (part b), showing the Fermi-level E_F and the built-in voltage V_{bi}. The lower part of the figure shows the electric field (with maximum value F_{max}) in each cell as a function of the position x.

---

[1] Obtained from Eq. (2.23) with $\tau_p = 2.5\times10^{-3}$ s [26] and $\mu_p = 450$ cm^2/Vs (value given in Appendix H in Ref. [13]).

If we make an *np*-cell using a polycrystalline semiconductor, we get the structure shown schematically in Figure 2.6. The grain boundaries are represented by the irregular lines. The additional recombination sites added by the grain boundaries, reduce the performance of solar cells, and mainly the open-circuit voltage. The next chapter provides the models to understand the influence of the grain boundaries on the open-circuit voltage.

The influence of grain boundaries on the electrical behavior of a semiconductor, and in particular of solar cells, can be manipulated. The most intuitive solution to minimize the influence of grain boundaries, is to reduce its number. Minimizing the number of GBs implies a maximization of the grain size. In practice, the preparation method determines the maximum grain size and even the electrical activity of the grain boundaries.
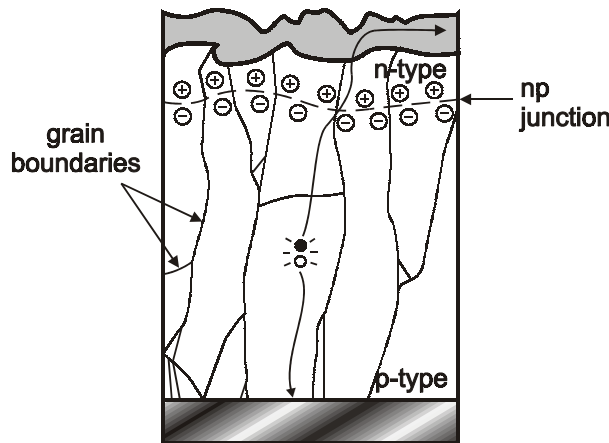
Figure 2.6: An *np*-cell in a polycrystalline material. The irregular lines represent grain boundaries, which constitute defects that harm the electrical properties of the cell.

2.4.2 Current(J)/voltage(V) characteristics

The current density J of a solar cell as a function of the voltage V is written as

$$J(V) = \sum_k J_{rec,k}(V) - J_{phot}(V) \,, \tag{2.24}$$

where $J_{rec,k}$ are the recombination currents in the cell, and J_{phot} the current provided by the generation. Each recombination current represents a particular recombination mechanism. In general, $J_{rec}(V)$ gives the diode-like characteristic observed in solar cells. For *np* junctions $J_{rec,k}(V)$ is given by

$$J_{rec,k}(V) = J_{0,k}\left[\exp\left(\frac{qV}{n_{id,k}kT}\right) - 1\right], \qquad (2.25)$$

where $J_{0,k}$ is the saturation current density, and $n_{id,k}$ the ideality factor. Both $J_{0,k}$ and n_k are constants that depend on the recombination current under consideration. Three recombination mechanisms must be considered to model the characteristics of *np* junctions: the recombination of carriers in their diffusion path, in the space-charge region, and at the interfaces between the semiconducting layers and the contacts. In chapter 5, I obtain the J/V characteristics of the *pin* cell, which shows recombination currents that are mathematically more complicated than (2.25). It turns out that neither the saturation currents $J_{0,k}$ nor the photogeneration currents are constants. Instead, these quantities depend on the applied voltage *V*.

In practice, a solar cell shows contact and internal resistances and shunting currents. The shunting currents are usually modeled by resistances connected in parallel to the solar cell, while the contact resistances are series connected. Both resistances affect the current voltage characteristic given by (2.24). The series resistance R_S reduces the measured voltage by the amount IR_S, being *I* defined by

$$I = JA, \qquad (2.26)$$

where *A* is the cell area; while the parallel resistance R_P adds a current ($V - IR_S)/R_P$. Figure 2.7 shows the equivalent circuit for a solar cell, which includes a current source to represent the generation, the diodes corresponding to the recombination currents, and the resistive elements.
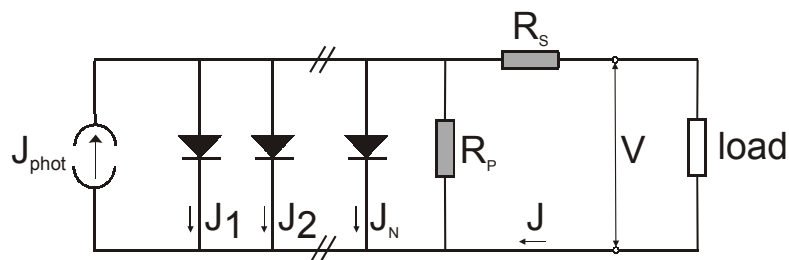
Figure 2.7: This circuit describes the electrical operation of a solar cell, where the current source delivers a current density J_{gen}, and part of this current is lost by recombination mechanisms, modeled by the diodes. Behind the resistances R_S and R_P, the load sees a voltage V.

In chapter 6, I correct the J/V characteristics measured on test cells by R_S and R_P. After that correction, I obtain the J/V characteristics with the model of the

pin cell obtained in chapter 5, and gain information about the recombination mechanisms and transport parameters of laser-crystallized silicon.

The electrical parameters that characterize a solar cell are the open circuit voltage V_{OC}, the short circuit current J_{SC}, the fill factor FF, and the efficiency η. The fill factor is the relation between the electrical power given by the product of current and voltage at the maximum power point (*mpp*) $I_{mpp}V_{mpp}$, with respect to the value $I_{SC}V_{OC}$. The values at the *mpp* must be calculated from the *I(V)* curve multiplied by *V*. The fill factor is then given by the quotient

$$FF = \frac{I_{mpp}V_{mpp}}{I_{SC}V_{OC}}.$$
(2.27)

With the optical input power P_{light}, the efficiency η of the solar cell is given by

$$\eta = \frac{I_{mpp}V_{mpp}}{P_{light}}.$$
(2.28)

3 Solar cell modeling

This chapter gives the current/voltage characteristics on *np*-cells, considering two components of the recombination currents: the current associated to the recombination in the space-charge region, and the current from the recombination in the neutral regions of the cell. I show that, under certain conditions, the current/voltage equation becomes a function of an unique effective diffusion length. Moreover, I give an equation that relates unambiguously the open-circuit voltage, the short circuit current, and the effective diffusion length. This equation constitutes a tool *to extract* the diffusion length from measured values of short-circuit current and open-circuit voltage. Additionally, I develop a second method to extract L_{eff}, considering J_{SC} and the optical absorption in the cell.

At the end of this chapter, I adapt this model to polycrystalline solar cells, explaining the experimentally observed increase of efficiency with grain size.

3.1 Efficiency limitations in polycrystalline silicon cells

The efficiency of a solar cell generally increases with increasing grain size [27]. The origin of that increase is found in the increase of the open circuit voltage, the short circuit current, and the fill factor. This behavior was first shown by Gosh et al. in 1980 [27], who put together the output parameters of *np* solar cells with grain sizes between 10^{-1} and 10^{4} µm. These authors showed that the trend was observed regardless of the preparation method utilized by the different research groups. The explanation for this increase is simple: if one increases the grain size, the amount of grain boundary area per unit volume decreases, reducing the total amount of recombination centers in the cell. The density of recombination centers determines the minority carrier lifetime, and hence the minority carrier diffusion length. Since V_{OC} and J_{SC} increase with the diffusion length, we expect that V_{OC}, J_{SC} and η increase with grain size, as observed experimentally. The observed increase of the *FF* with g is also understood along these lines, because *FF* is a function of V_{OC}.

To explain the experimental data, Gosh et al. adapted the theory for monocrystalline *np* junctions to polycrystalline cells. They replaced the minority carrier diffusion length contained in the *J(V)* equation, by an effective diffusion length that takes into account recombination at grain boundaries.

The data available at the time of Gosh's paper belonged to cells that had much lower efficiencies than today's cells. With a grain size of 100 μm, efficiencies of 7 % were achieved back in 1980 [27], while cells having the same grain size reach 16.6 %, as reported recently (see Table 3.1 below). The differences between the old an new cells comes from structural differences: the films of the 7 % efficient cells had grain boundaries parallel *as well as* perpendicular to the carrier's current flow. With the preparation techniques used nowadays, the *perpendicular* grain boundaries are eliminated on purpose, boosting the efficiency of solar cells. An extensive review on the preparation methods and the solar cells obtained with each technique was given recently (See Refs. [28] and [29]). In addition, the paper of Gosh did not consider recombination in the SCR *and* in the neutral regions of the cells simultaneously.

A grain size dependence of V_{OC}, J_{SC} and *FF* is also observed in modern poly-Si solar cells, but the model of Gosh no longer explains the experimental data! Therefore, the model *must* be reworked to explain the new experimental results. In this section, I give a model for *np* cells that explains the solar cell parameters obtained with the new technologies, and the influence of the grain size. The model follows the lines described in Ref. [30], where the open circuit voltage is modeled as a function of an effective diffusion length that contains the grain size. That diffusion length unifies the effects of the recombination in base of the cell, as well as at the contacts of it. However, the quantities left unsolved in [30] are J_{SC} and *FF*, and V_{OC} taking into account recombination in the SCR. Here I solve V_{OC} as well as J_{SC} and *FF*, and improve the model by including the recombination in the base as well as in the SCR of the cell.

3.2 Extraction of effective diffusion lengths

This section gives a general model for the J/V characteristics, which considers an effective diffusion length. The diffusion length is called effective because it contains all of the recombination processes present in the cell. By using this quantity, the theory presented here applies to any np solar cell. In the next section, I adapt the diffusion length, and hence the J/V characteristics, to a polycrystalline cell.

Considering a double-diode model of a solar cell, the current/voltage characteristics are given by [31]

$$J = J_{01}\left[\exp\left(\frac{V}{V_t}\right) - 1\right] + J_{02}\left[\exp\left(\frac{V}{2V_t}\right) - 1\right] - J_{SC}. \tag{3.29}$$

Here, the first term represents the recombination current in the base, and it assumes that $n << p$ (in a p-type base), giving an ideality factor $n_{id} = 1$. The second term belongs to the recombination in the SCR. The SCR-recombination is modeled considering SRH recombination via a single trap located in the middle of the bandgap, where n and p are assumed to have similar values, resulting $n_{id} = 2$ [31]. The saturation current densities $J_{01,2}$ depend on recombination parameters such as the effective diffusion length L_{eff} of carriers. In a *monocrystalline* material, J_{01} is a function of an effective diffusion length $L_{eff} = L_{eff,mono}$, which is given by [32]

$$L_{eff,mono} = L_n \frac{\cosh\left(\dfrac{W}{L_n}\right) + \sigma \sinh\left(\dfrac{W}{L_n}\right)}{\sinh\left(\dfrac{W}{L_n}\right) + \sigma \cosh\left(\dfrac{W}{L_n}\right)}. \tag{3.30}$$

This equation considers a solar cell with a p-type base with a thickness W, and a recombination velocity S_b at the back contact contained in σ, which is defined by $\sigma = S_b L_n / D_n$.

The current density J_{02} depends only on the diffusion length L_n of carriers, not including contact recombination [31]. In order to simplify the analysis, but without loosing generality, I make an assumption that allows to use the *same* diffusion length to calculate J_{01} and J_{02}: the value of L_n does not depend on the position in the cell (SCR or bulk), and the recombination of carriers at the back

contact does not affect strongly L_{eff}. In a monocrystalline material, this assumption imposes that the carrier diffusion length is smaller than the thickness of the cell, since, after Eq. (3.30), $L_{eff,mono}$ equals L_n within an error smaller than 20 % provided $L_n/W < 1$. The present model assumes $\underline{L_n/W < 1}$, and considers that the error made in $L_{eff,mono}$ is affordable. In this case, both current densities J_{01} and J_{02} become a function of a unique diffusion length L_{eff}. In the p-type base, the saturation current density J_{01} is given by [32]

$$J_{01} = \frac{qD_n n_i^2}{N_A} \frac{1}{L_{eff}},$$

(3.31)

where N_A is the doping density in the base of the cell. In the SCR, the saturation current density J_{02} is a function of the maximum electric field F_{max} and L_{eff}, as [33]

$$J_{02} = \frac{q\pi D_n n_i V_t}{F_{max}} \frac{1}{L_{eff}^2}.$$

(3.32)

If the doping profiles are step-like, F_{max} is given by [33]

$$F_{max} = \sqrt{\frac{2qN_A V_{bi}}{\varepsilon_s}},$$

(3.33)

where V_{bi} is the built-in voltage (see Figure 2.5).

Having defined J_{01} and J_{02} as a function of L_{eff}, we write the whole J/V characteristics as a function of L_{eff}. Thus, we express L_{eff} as a function of solar cell output parameters such as J_{SC} and V_{OC}.

3.2.1 Method to extract L_{eff} from V_{OC} and J_{SC}

At $J = 0$, we have $V = V_{OC}$, and using the definitions of J_{01}, J_{02}, and F_{max}, Eq. (3.31) is rewritten as

$$J_{SC} = \frac{qD_n n_i^2}{N_A} \frac{1}{L_{eff}} \exp\left(\frac{V_{OC}}{V_t}\right) + q\pi D_n n_i V_t \sqrt{\frac{\varepsilon_s}{2qN_A V_{bi}}} \frac{1}{L_{eff}^2} \exp\left(\frac{V_{OC}}{2V_t}\right).$$

(3.34)

From this equation, it is possible to extract L_{eff} as a function of V_{OC} and J_{SC}. Note that since N_A has an exponent of -1 in the first term, and -½ in the second term, Eq. (3.34) is a function of exponentials of $[V_{OC} - V_t\, ln(N_A/n_i)]$. The solution of L_{eff} from Eq. (3.34) is then given by

$$L_{eff} = \frac{z + \left(z^2 + 2\pi V_t J_{SC} \left(\frac{2D_n \varepsilon_S}{V_{bi}} \right)^{1/2} z^{1/2} \right)^{1/2}}{2J_{SC}}, \tag{3.35}$$

where z is given by[2]

$$z = qn_i D_n \exp\left(\frac{V_{OC}}{V_t} - \ln\left(\frac{N_A}{n_i} \right) \right). \tag{3.36}$$

Separating the known from the unknown quantities in Eqs. (3.35) and (3.36), we find that: the values of ε_S and n_i are material constants, and the influence on L_{eff} of V_{bi} in its practical range from 0.5 to 0.9 V can be neglected. Thus, we can conclude that Eq. (3.35) gives a unique relationship between the effective diffusion length L_{eff}, the open circuit voltage V_{OC}, and the short circuit current density J_{SC}, which holds for both, cells with dominating recombination in the SCR, or in the bulk.

Figure 3.1 shows the increase of L_{eff} with $[V_{OC} - V_t\ ln(N_A/n_i)]$, given by Eqs. (3.35) and (3.36) with $D_n = 10$ cm^2/s, and $V_{bi} = 0.8$ V. The curves indicate that a material with low recombination (high L_{eff}) is required to obtain solar cells with high values of V_{OC}. The plot shows two regions: the region for low L_{eff}, where the recombination in the SCR determines V_{OC}, and $n_{id} = 2$; and the region of higher L_{eff}, where V_{OC} is limited by bulk recombination, resulting $n_{id} = 1$.

The curves in Figure 3.1 suggest that, by calculating the ideality factor n_{id} at V_{OC} from the slope of a measured J/V curve, one can determine where the highest recombination takes place: in the SCR, or in the bulk. Cells with a small diffusion length, will show $n_{id} = 2$, and will have V_{OC} limited by the recombination in the SCR. By increasing L_{eff}, the generated electron-hole pairs will not recombine in the SCR but mainly in the bulk, showing $n_{id} = 1$. In the case of a measured value of $n_{id} = 1.5$, for example, L_{eff} will belong to the transition region between SCR and bulk recombination (curved part of the lines in Figure 3.1). This suggests that in order to increase V_{OC}, the experimentalist must redesign the cell or the preparation process attempting to reduce the recombination in the SCR, for example by narrowing it. If

---

[2] The equation for z can be simplified further, but it is useful to let it expressed this way.

he eventually reaches the region with $n_{id} = 1$, he has then to concentrate in the base, trying to reduce the recombination there.
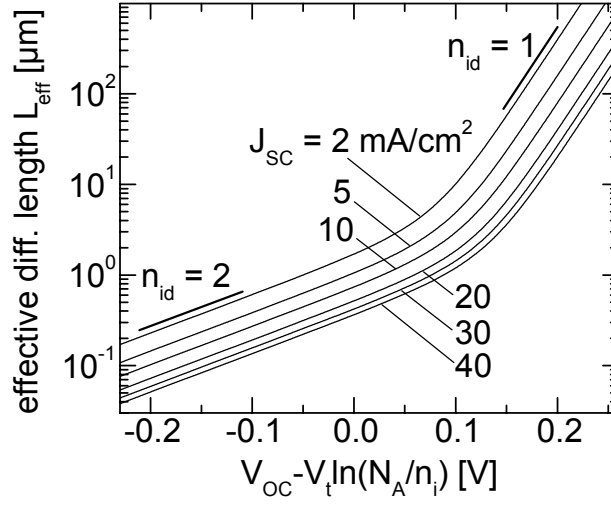

Figure 3.1: The effective diffusion length L_{eff} as a function of the open circuit voltage V_{OC}, and the short circuit current density J_{SC}, as obtained by the present model. This relationship holds for both, cells with dominating recombination in the SCR, or in the bulk. At low V_{OC} (or L_{eff}) the curves are determined by the recombination in the SCR, where $n_{id} = 2$. The recombination in the base (where $n_{id} = 1$) determines V_{OC} in cells with high L_{eff}.

Equation (3.35) is extremely useful for the experimentalist who wants to estimate L_{eff}, because J_{SC}, V_{OC}, and N_A are easy to measure. The standard technique to determine L_{eff} is much more complicated, since it is based on internal quantum-efficiency (IQE) measurements, which require an exact knowledge of the absorption constant of the material [32], making a determination of L_{eff} rather intricate.

Now I want to prove that Eq. (3.35) gives the correct value of L_{eff}. I select literature data of silicon solar cells where L_{eff} was obtained from IQE measurements, and compare them to the values of L_{eff} predicted by Eq. (3.35). To ensure a correct use of the model, I select data that meat the condition $L_{eff}/W < 1$. Figure 3.2 shows that the values of L_{eff} obtained with the present model, agree with the IQE values *over three orders of magnitude* of L_{eff}. The solid line shown in the figure gives the identity L_{eff} (modeled) = L_{eff} (measured by IQE). The dashed lines represent the least-square standard deviation of the data from the identity line, which show that the present model predicts L_{eff} with an error of 35 % (assuming that the IQE values are exact). The circles in Figure 3.2 belong to silicon epitaxial cells prepared with the ion-assisted deposition method [34], while the triangles belong to multicrystalline silicon cells [35].
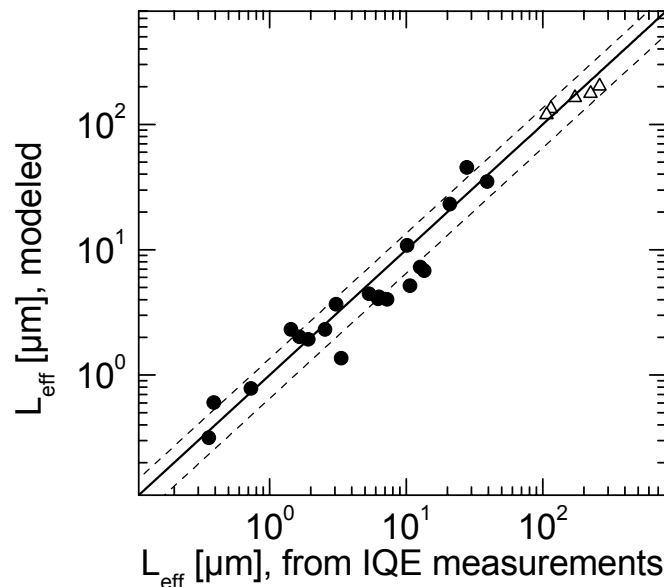
Figure 3.2: The effective diffusion length L_{eff} of silicon solar cells, determined by our model agrees with the values of L_{eff} obtained by IQE measurements, over three orders of magnitude of L_{eff}. The circles in belong to silicon epitaxial cells prepared with the ion-assisted deposition method [34], while the triangles belong to multicrystalline silicon cells [35].

3.2.2 Method to extract L_{eff} from J_{SC}

This section develops a model that shows that it is possible to describe J_{SC} as a function of L_{eff} without using the J/V equation. The short-circuit current is the sum of all collected carriers at every position of the cell. Carriers generated by the light near the junction than others deep in the base, will more likely be collected and contribute to J_{SC}. Thus, the short-circuit current density depends on the thickness W of the base[3], L_{eff}, and the generation rate G. In Appendix A, I show that it is a reasonable approximation to express J_{SC} by the equation

$$J_{SC} = \int_0^W \exp\left(-\frac{x}{L_{eff}}\right) G(x) dx . \tag{3.37}$$

The generation rate depends on the spatial coordinate x, with the origin ($x = 0$) placed at the np junction. The exponential term in (3.37) is the collection efficiency f_C of the cell. At the junction ($x = 0$), f_C is 1, indicating that all carriers contribute to J_{SC}. When we go from the junction to the rear of the cell by increasing x, the collection efficiency decreases because the minority carriers recombine before

---

[3] Which is almost equal to the cell thickness, because the emitter is very narrow in practice.

reaching the junction. This recombination vs. collection process is weighted by the value of L_{eff}.

Figure 3.3 shows J_{SC} to increase with both W and the ratio L_{eff}/W, as calculated from Eq. (3.37). The generation rate to evaluate these curves was calculated assuming AM1.5 irradiation, some 'light trapping' provided by a reflector at the rear of the cell, and an antireflecting coating on the front. Appendix A gives more details on the calculation of $G(x)$. Figure 3.3 shows that if the diffusion length exceeds the cell thickness ($L_{eff}/W > 1$), J_{SC} saturates, indicating that almost all the carriers generated by the light are extracted.
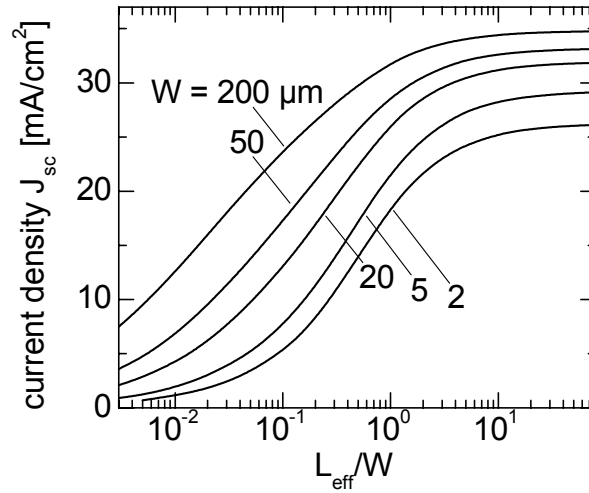
Figure 3.3: The short circuit current density J_{SC} of a solar cell is improved by increasing the ratio L_{eff}/W, or simply by increasing the cell thickness W to absorb more light.

Figure 3.3 gives the whole physical picture of J_{SC}: the increase of J_{SC} with W reflects that more photons are absorbed in thicker cells, while the increase of J_{SC} with L_{eff}/W reflects that the collection-recombination balance is more efficient at high L_{eff}/W. Thus, in order to improve J_{SC}, it is sufficient to have high values of L_{eff}/W rather than L_{eff}, as in the case of V_{OC}.

Additionally, if we have a material with high density of recombination centers (low L_{eff}), we can still achieve a good J_{SC} by *reducing* W, increasing the value of L_{eff}/W. Certainly, with low values of W, we force a closeness between the generated carriers and the junction, enabling the carriers to reach the junction. This increase of J_{SC} takes place only if we provide additional light trapping in order to compensate for the smaller absorption caused by the lower thickness.

Comparing both methods to extract L_{eff}, we note that it is much less certain to extract L_{eff} from J_{SC} (method 2), than obtaining L_{eff} from the double diode model (method 1). The difficulty in method 2 lies in the fact that the light trapping and the absorption coefficient may vary from cell to cell. In silicon films with small grains, even the grain size increases light absorption, since the GBs serve as light scattering centers [36]. Figure 3.3 considers generation rates with no special light trapping artifacts or enhanced absorption at scattering centers.

The two methods to extract L_{eff} described here are utilized in the next section to analyze polycrystalline solar cell data.

3.3 Effective diffusion length in polycrystalline material

In a *polycrystalline* material, we define a diffusion length $L_{eff,poly}$, which contains an additional recombination process: the recombination at the grain boundaries (GBs). The recombination at GBs incorporates two quantities into our analysis: the grain size g, and the recombination velocity S_{GB} of carriers at the GBs. The knowledge of S_{GB} is important because it *quantifies* the GB recombination activity. If we had a functional dependence between g, S_{GB} and $L_{eff,poly}$, we were able to calculate S_{GB} from any polycrystalline cell by extracting L_{eff} (using the methods developed in this chapter) and measuring g. In Ref. [37], the diffusion length $L_{eff,poly}$ was calculated considering the diffusion and recombination of minority carriers in the base of a *pn* cell. The three-dimensional model assumes square, columnar grains, with no GBs perpendicular to carrier flow. With the recombination of carriers inside the grains described by $L_{eff,mono}$, the diffusion length $L_{eff,poly}$ is given by

$$L_{eff,poly} = \frac{L_{eff,mono}}{\sqrt{1 + \frac{2S_{GB}L_{eff,mono}^2}{D_n g}}} \ , \tag{3.38}$$

which includes the grain size g, and the recombination velocity S_{GB} at the grain boundaries. This equation shows us that if we have a large-grained material (high g), $L_{eff,poly}$ approaches the limit given by the monocrystalline value $L_{eff,mono}$. That behavior is physically correct because there are few grain boundaries per unit volume. For $L_{eff,poly} < 0.8L_{eff,mono}$, $L_{eff,poly}$ can simply be expressed by $L_{eff,poly} =$

$\sqrt{D_n g / 2 S_{GB}}$. In Figure 3.4, the solid lines show the increase of $L_{eff,poly}$ with g and

S_{GB}, from Eq. (3.38). The double logarithmic axis reveal the slope of ½. For the

design of solar cells, this slope implies that if we want to obtain an increase of one

order of magnitude for $L_{eff,poly}$, one has to increase g by two orders of magnitude! The

solid lines in Figure 3.4 saturate at the value of $L_{eff,mono}$ at the chosen value for

$L_{eff,mono} = 10^2$ μm.
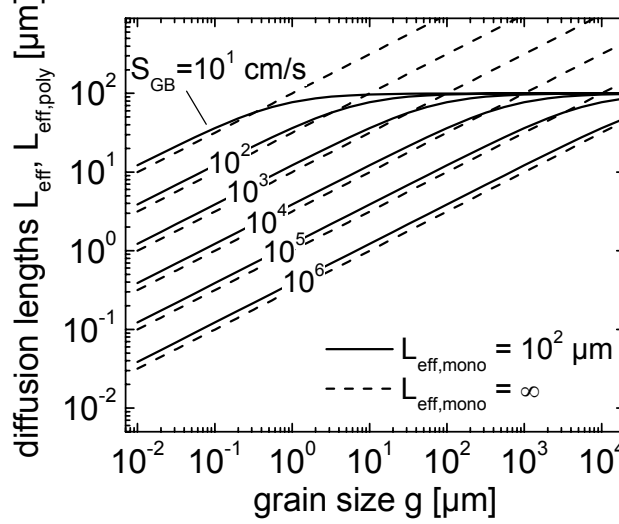
Figure 3.4: Solid curves show that the diffusion length in polycrystalline silicon increases
with grain size, and with the surface recombination velocity S_{GB}, showing a limit value
given by the diffusion length $L_{eff,mono}$ without grain boundaries. The dashed lines assume
$L_{eff,mono} = \infty$.

Knowing $L_{eff,poly}$ *via* L_{eff}, enables one to obtain values for the minimum

diffusion length $L^0_{eff,mono}$ in the grains, and the maximum recombination velocity

S^*_{GB}. Thus, assuming no grain boundary recombination ($S_{GB} = 0$), we get $L^0_{eff,mono} = L_{eff,poly}$. If the recombination at GBs dominates $L_{eff,poly}$, which is equivalent to assume

$L_{eff,mono} = \infty$, then Eq. (3.38) defines S^*_{GB} as

$$S^*_{GB} = \frac{gD_n}{2} \frac{1}{L^2_{eff,poly}} .$$
                                                                        (3.39)

This equation indicates that by extracting L_{eff}, and knowing g, we can directly

extract information about the recombination at the grain boundaries in our solar

cell. In Figure 3.4, the dashed lines are calculated with $L_{eff,mono} = \infty$. The value of the

parameter near each dashed line corresponds to S^*_{GB} from Eq. (3.39).

3.4 Application to polycrystalline silicon cells

This section extracts L_{eff} from V_{OC} and J_{SC} from a vast polycrystalline silicon cells data set, with grain sizes varying from 10^{-2} to 10^{4} μm. Then I model the L_{eff} data with Eq. (3.38), showing the grain size dependence of L_{eff} in polycrystalline silicon cells. Table 3.1 lists the data extracted from the literature of the past eight years.

Table 3.1: Experimental polycrystalline silicon solar cell parameters extracted from the literature. The geometrical quantities given are the area A, the cell thickness W, and the grain size g. The doping density N_A corresponds to the p-type base of the cells. The electrical parameters, given under AM1.5 illumination conditions, are the efficiency η, the open circuit voltage V_{OC}, the fill factor FF, and the short circuit current density J_{SC}. Cells denoted as pvn-type have low doped and n-type middle-layers.

cell	cell type	Ref.	A [cm^2]	W [μm]	g [μm]	N_A [cm^{-3}]	η [%]	V_{OC} [mV]	FF [%]	J_{SC} [mA/cm^2]
A	np	[38]	4	60	10^4	2×10^{16} [a]	16.5	608	77	35.1
B	np	[39]	1	100	10^3	2×10^{16} [a]	16.6	608	82	33.5
C	np	[40]	1	72	10^3	2×10^{16} [b]	9.3	567	76	21.6
D	np	[40]	1	30	10^3	2×10^{16} [b]	11	570	76	25.6
E	np	[42]	1	300	500	2×10^{16} [b]	9.95	517	7.2	27.1
F	np	[42]	1	300	500	2×10^{16} [b]	11.1	538	72.4	28.5
G	np	[41]	1	500	250	2×10^{16} [b]	10.7	527	69	31.1
H	np	[44]	1	49	200	2×10^{17}	8.2	525	66	23.8
I	np	[43]	1.3	30	150	3×10^{16}	8.3	561	74	20.1
J	np	[45]	?	330	20	2×10^{16} [b]	4.3	430	64	16.7
K	np	[46]	0.01	4.2	10	4.3×10^{17}	6.5	480	53	25.5
L	np	[48]	1	15	7	1×10^{17}	5.2	461	64	17.5
M	np	[44]	1	15	5	2×10^{17}	2.8	368	59	12.8
N	np	[47]	0.17	15	1	1×10^{17}	5.3	400	58	23
O	np	[49]	1	20	1-3	2×10^{17}	2.0	340	59	10.1
P	pvn	[50]	?1	2	≈0.5	2×10^{16} [b]	10.1	539	77	24.35
Q	pvn	[51]	1	5.2	1	2×10^{16} [b]	9.2	553	66	25
R	pin	[53]	0.7	2	0.05	2×10^{16} [b]	7.5	499	68.7	22
S	pin	[52]	0.25	2.1	0.042	2×10^{16} [b]	9.5	500	68	28
T	pin	[54]	0.25	2.5	≈0.01 [55]	2×10^{16} [b]	8.6	500	66	26.2
U	pin	[56,57]	0.33	2	≈0.01	2×10^{16} [b]	8.5	531	70	22.9

a) this value is an estimate that corresponds to commonly utilized doping levels.
b) value estimated from the resistivity values between 1-2 Ωcm (p-type material), given in the paper corresponding to each cell.

3.4.1 Extraction of L_{eff} from V_{OC} and J_{SC}

Figure 3.5 shows the increase of L_{eff} with g, where the values of L_{eff} were calculated with the data of Table 3.1 using Eq. (3.35). All the circles belong to np-

type cells, and all triangles to *pin-* or *pvn-* cells. The solid lines give $L_{eff,poly}$ from

Eq.(3.38), with $D_n = 10$ cm^2/s, $L_{eff,mono} = 10^2$ µm, and $V_{bi} = 0.8$ V. This value of V_{bi} is an

estimate that agrees with commonly found values in silicon cells. As explained in

section 3.2.1, the exact value of V_{bi} of each cell is not needed to extract L_{eff}.
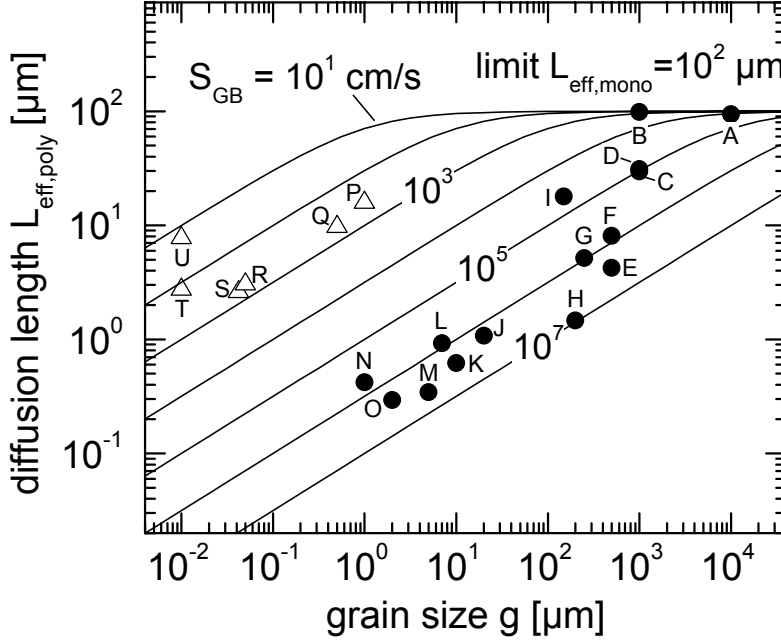

Figure 3.5: Data points give the diffusion lengths extracted from the data of Table 3.1 using Eq. (3.35). Circles belong to *np* cells, while the triangles use a *pin* structure. The overall increase of L_{eff} with the grain size g, indicates that the recombination at the grain boundaries generally determines L_{eff}, and hence the solar cell parameters. The lines model L_{eff} considering the recombination velocity S_{GB} at the grain boundaries.

Associating the data points to the solid lines in Figure 3.5, we distinguish two groups of data with different ranges of S_{GB}:

i) cells with $g > 1$ µm, have values of S_{GB} between 10^5 and 10^7 cm/s,

ii) for the nano- and microcrystalline cells, where $g < 1$ µm, the data is only understood with S_{GB} between 10^1 and 10^3 cm/s.

Despite the fact that the present model assumes *np* junctions and not *pin* junctions, the difference of S_{GB} between the two regions is large. Are the low S_{GB} values found for the *pin* cells misleading because the model does not apply to them? The answer to this question is given by the numerical simulations of *pin* cells given in chapter 5. The simulations show that S_{GB} must certainly have values between 300 to 1100 cm/s in those *pin* cells (at a grain size of around 1 µm).

Since the triangles of Figure 3.5 belong to cells with thicknesses between 2 and 10 μm, and the values of L_{eff} lie in the same range, we could suspect that the use of Eq. (3.35), which holds for $L_{eff}/W < 1$, is misleading in these cells. This would imply that the values of S_{GB} predicted by the model for the cells with $g < 1$ μm would be incorrect. Nevertheless, the numerical simulations of *pin* cells given in chapter 5, are in agreement with the values of S_{GB} predicted by the present model.

3.4.2 Extraction of L_{eff} from J_{SC}

In this section, the second method to extract L_{eff} is utilized. From Figure 3.3, I determine graphically L_{eff} from the values of J_{SC} and W of Table 3.1, and model it with $L_{eff,poly}$. The data points in Figure 3.6 show the resulting grain size dependence of L_{eff}, as extracted from J_{SC}. The solid lines are given by $L_{eff,poly}$ from Figure 3.4, which assume a limit value of 10^2 μm. All the circles belong to *np*-type cells, while the triangles are *pin* cells. The model predicts that all the cells have values of S_{GB} between 10^1 and 10^6 cm/s. Similarly to the $V_{OC}(g)$ plot of Figure 3.5, most of the small-grained cells (stars), have much lower recombination velocities than the cells in the range $g > 1$ μm.
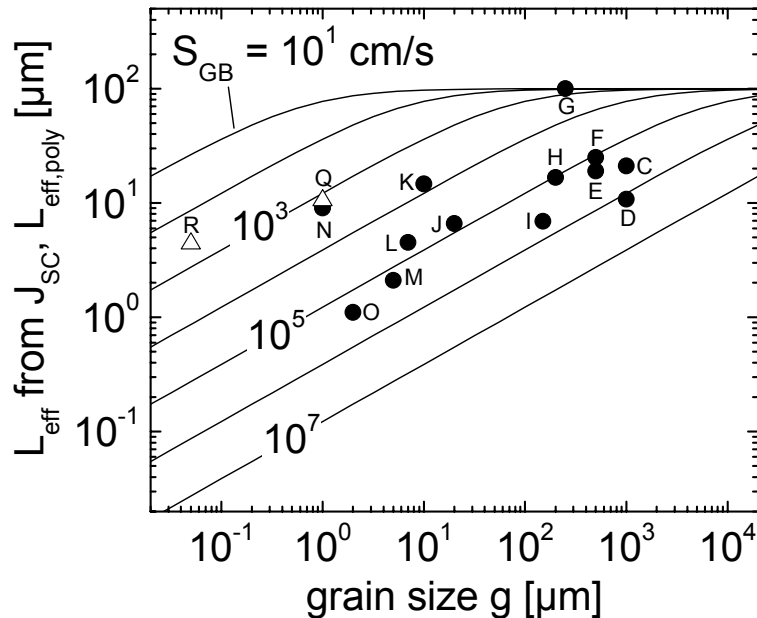

Figure 3.6: The diffusion length L_{eff} extracted from the values of the short circuit current density J_{SC}, shows an increase with the grain size g. The lines correspond to the model for $L_{eff,poly}$ given by Eq. (3.38).

Some data points (especially most cells with $g < 0.1$ μm) were omitted in Figure 3.6, since the extraction of L_{eff} from J_{SC} yielded $L_{eff}/W >> 1$, where the present model does not apply. By comparing the values of L_{eff} of Figure 3.6 (method 2) with those shown in Figure 3.5 (method 1), we note that both methods give different values of L_{eff}. The present method yields values that are up to an order of magnitude larger. It is possible that such values are overestimated because the generation rate profiles I calculated for the curves of Figure 3.3 have too small values for some cases. Indeed, most cells with $g < 0.1$ μm yielded false values of L_{eff} because nanocrystalline silicon has a higher absorption coefficient than the assumed monocrystalline values [36]. Among the large-grained cells, the present method gives a misleading L_{eff} for example in the cell of Ref. [38], which uses a front surface with pyramidal texturing, increasing the generation rate. Such light trapping artifacts where not contemplated in this work.

These statements indicate that the extraction of L_{eff} and hence S_{GB} *via* J_{SC} for many different cells, is not reliable if one considers only one light-trapping scheme (as done here). A correct estimation of L_{eff} *via* method 2, requires an exact knowledge of the light trapping in each cell under study. This makes method 2 more case dependent, and thus less general, than method 1, which does not need any knowledge about light trapping. Therefore, I assume that the correctly modeled L_{eff} as a function of g is that obtained with method 1 (Figure 3.5).

3.4.3 Fill factor

The *FF*-analysis is simple because the *FF* is exclusively dependent on n_{id} and V_{OC}, regardless of J_{SC}. However, unlike V_{OC} and J_{SC}, the fill factor is strongly affected by the series resistance R_S of the cell. With R_S, the fill factor takes the form [58]

$$FF = FF_0\left(1 - r_S\right),\tag{3.40}$$

where FF_0 is the fill factor with no parallel or series resistances, obtained from J_{mpp} and V_{mpp}, V_{OC} and J_{SC}, all calculated using Eq. (3.29). In Eq. (3.40), r_S is a relative characteristic resistance, given by

$$r_S = \frac{R_S / A}{V_{OC} / J_{SC}}.\tag{3.41}$$

Figure 3.7 shows the increase of *FF* with V_{OC} found in the experimental data of Table 3.1 (triangles and circles), and the solid curves calculated with Eqs. (3.29), (3.40) and (3.41). The data point 'K' shows a very low *FF*, which may be explained by the high series resistance of several Ohms reported by the authors [46].[4]

The procedure to obtain each point of these curves consists in choosing a value of L_{eff}, and utilize Eq. (3.29) to calculate J_{SC}, V_{OC}, J_{mpp} and V_{mpp} to determine *FF*, at every r_S. The lowest values of *FF*, for example, result from considering the least values of L_{eff} (since low value of L_{eff} give low values of J_{SC}, V_{OC}, J_{mpp} and V_{mpp}). The parameters utilized here are again $D_n = 10$ cm^2/s, $L_{eff,mono} = 10^2$ μm, $V_{bi} = 0.8$ V, $N_A = 2\times10^{16}$ (equal to the most common values of Table 3.1). Calculations with different values of V_{bi} and N_A left the curves shown in Figure 3.7 almost unchanged.
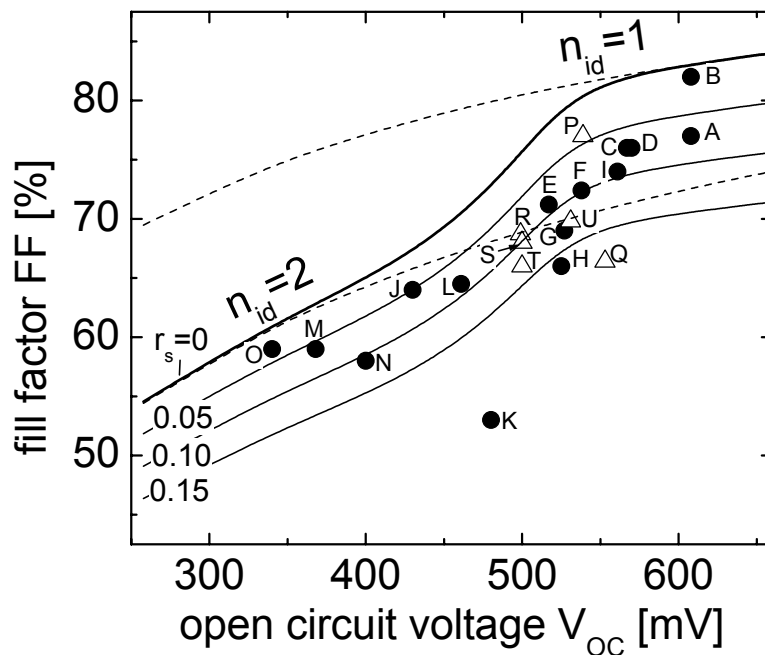
Figure 3.7: The data points show that fill factor increases with the open circuit voltage, and decreases with the characteristic resistance r_s. The circles belong to *np* cells, while the triangles are *pin* cells. The double-diode model (solid lines) is the combination of the single diode model considering recombination in the base ($n_{id} = 1$), and recombination in the space-charge region ($n_{id} = 2$), shown individually by the dashed lines. The single-diode model gives a correct value of *FF* only if the cells have $n_{id} \approx 1$, or $n_{id} \approx 2$. The double diode model explains that from $V_{OC} = 400$ mV, the cell's strongest recombination region shifts from the space-charge region to the base. The good fit to the data is only explained by the double diode model.

---

[4] However, they did not report the value of R_S.

The dashed lines in Figure 3.7 correspond to a single-diode approach. These were calculated at $r_S = 0$ with either the SCR-recombination ($n_{id} = 2$) or the bulk recombination ($n_{id} = 1$) currents. The curve with $n_{id} = 2$ neglects the term of bulk recombination current, while the curve with $n_{id} = 1$ neglects the SCR-recombination current (See Eq. (3.29)). The dashed lines show that *FF* approaches the double diode model on its extremes. However, the single-diode models do not fit the data! This finding, together with the good fit to the data of the double diode model (solid lines), strongly indicates that *only* the double-diode equation explains correctly *np*-cells. The commonly assumed single-diode model is only valid to calculate the whole J/V characteristics provided one of both recombination terms in Eq. (3.29) is negligible, which is unknown *a priori*.

The double-diode model explains how the effective diffusion length controls the fill factor: a solar cell with a small diffusion length, suffers from SCR-recombination, showing $n_{id} = 2$. As seen in Figure 3.7, the SCR-recombination limits the *FF* to the range $50 - 60$ %. No cell with high SCR-recombination can reach a higher fill factor than 60 %! Furthermore, as the diffusion length increases, the double diode model gives the range of V_{OC} where the *critical* region of recombination *shifts* from the SCR to the base. This occurs between $V_{OC} = 400$ and $V_{OC} = 500$ mV. A further increase of L_{eff} shifts completely the critical recombination region to the base, in which case *FF* reaches between 70 and 80 %. To resume this results, we can say that the closer a cell comes to $n_{id} = 1$, the highest chances to yield a high efficiency it will have.

This observations allow us to interpret the position of the triangles shown in Figure 3.7. Since the triangles lie in the range of moderate to high voltages and fill factors, which can only be reached with moderate to large values of L_{eff}, I arrive at the same conclusion of the previous analyses: S_{GB} must be low in the cells with $g < 1$ μm.

3.5 Conclusions

The modeled data leave an important question unanswered: how is it possible that the small-grained *pin* cells have such low values of S_{GB}? An explanation for this

is given in Refs. [30] and [59], where it was predicted that the low S_{GB} comes from *structural* differences between the cells with $g < 1$ µm and with $g > 1$ µm. The pattern found to make that estimation is that *all* the cells with $g < 1$ µm, were reported to have a {220} surface texture. With that information, the low S_{GB} is explained as follows: *"The measured {220}-texture implies a (110)-oriented surface for most of the grains. A large number of the columnar grains must therefore be separated by [110] tilt grain boundaries. Symmetrical grain boundaries of this type are electrically inactive because they contain no broken bonds"* [30]. The background behind this argument is that in general, an interrupted crystal lattice (like a grain boundary) shows energy states in the band gap. These states constitute the recombination centers. However, if a silicon atom of the GB uses all of its four bonds, and if these bonds are not too stressed, no energy states appear in the gap. That is exactly what happens in the case of [110] tilt boundaries, as explained in [30]. Therefore, as a result of the formation of a {220} surface texture, we get mostly [110] tilt boundaries, with a very low defect-level density. The modeling of cell data given in this chapter supports an occurrence of low defect densities at the GBs in the small grained cells *via* the low values of S_{GB} predicted.

The next chapter goes into the details of the grain boundary recombination velocity, which was only given as a parameter here. The influence of the grain size and the defect density on V_{OC} will be shown.

4 Models for grain boundaries

In the previous chapter, the recombination velocity S_{GB} was introduced to describe the recombination at grain boundaries in a simple way. The physical background of the recombination velocity is described by the equation $S_{GBn} = R_{GB}/(n - n_0)$, considering electrons as minority carriers (see Eq. (2.21)). Here, R_{GB} is the areal recombination rate at the GB, while n and n_0 are the electron concentrations at the GB and at the grain center, respectively. Assuming a single defect level in the center of the energy gap (i.e. $n_1, p_1 << n, p$) of a p-type material under low injection conditions (i.e. $n << p$), the SRH recombination rate R_{SRH} at the GB is given by

$$R_{SRH} \approx \frac{n - n_0}{\left(v_{th} \sigma_p N_t \right)^{-1}}$$

(4.1)

Thus, in this case of a single defect in the center of the gap, it is possible to express S_{GB} by the equation

$$S_{GB} = v_{th} \sigma_p N_t ,$$

(4.2)

which shows that the recombination velocity S_{GB} at the GB is proportional to the defect density N_t at the GB. Although this definition can be made only with one defect level, a distribution of defects leads also to an equation where S_{GB} is proportional to N_t [61] (provided the capture cross sections of each defect level σ_n and σ_p are equal).

In this chapter, I solve R_{GB}, n and n_0. This analysis enables to calculate the band bendings and the splitting of the Fermi-levels. Both quantities are then taken to calculate the maximum open-circuit voltage, and the conductivity of a polycrystalline film.

4.1 Grain boundaries in silicon

4.1.1 Band bending and maximum open circuit voltage

The model considers one-dimensional grains, i.e. a sequence of monocrystalline grains separated by grain boundaries. The grains have no contact to an external circuit, and no current flows out of the grains. The upper part of

Figure 4.1 shows such a one-dimensional polycrystal, where all grains are assumed to have the same size. Since the resulting structure is periodic, it is sufficient to consider the region that extends from one grain center to the next, covering exactly the grain size g. The lower part of the figure shows the band diagram of the modeled region assuming p-type material, introducing the QFLs with energies E_{Fp} and E_{Fn}, and the widths δ and W of the grain boundary and the SCRs, respectively. The rightmost part of the band diagram introduces the splitting qV^0_{OC} of the QFLs, supposed constant throughout the grain, and the quantity $q\zeta$. As shown in Ref. [62], the assumption of flat QFLs is valid at generation rates occurring under daylight illumination (above 0.1 Sun). It makes sense to utilize the symbol qV^0_{OC} for the energy difference between the quasi-Fermi levels, because, as explained in the next sections, this quantity corresponds to the maximum open circuit voltage a solar cell can reach.

To solve the band bendings and the splitting of the QFLs, we need to write Poisson's and the continuity equations throughout the band diagram of Figure 4.1. The analysis has two parts:

i) the equilibrium analysis, where the material is in the dark, and

ii) out of equilibrium, e.g. when we generate electron-hole pairs using light.

Under equilibrium, only one Fermi-level is present, resulting in $E_{Fp} = E_{Fn}$ (see section 2.1). Thus, we only need to solve Poisson's equation. Out of equilibrium, where $E_{Fp} \neq E_{Fn}$, we need to solve the coupled Poisson and continuity equations for the extra unknown we introduced.
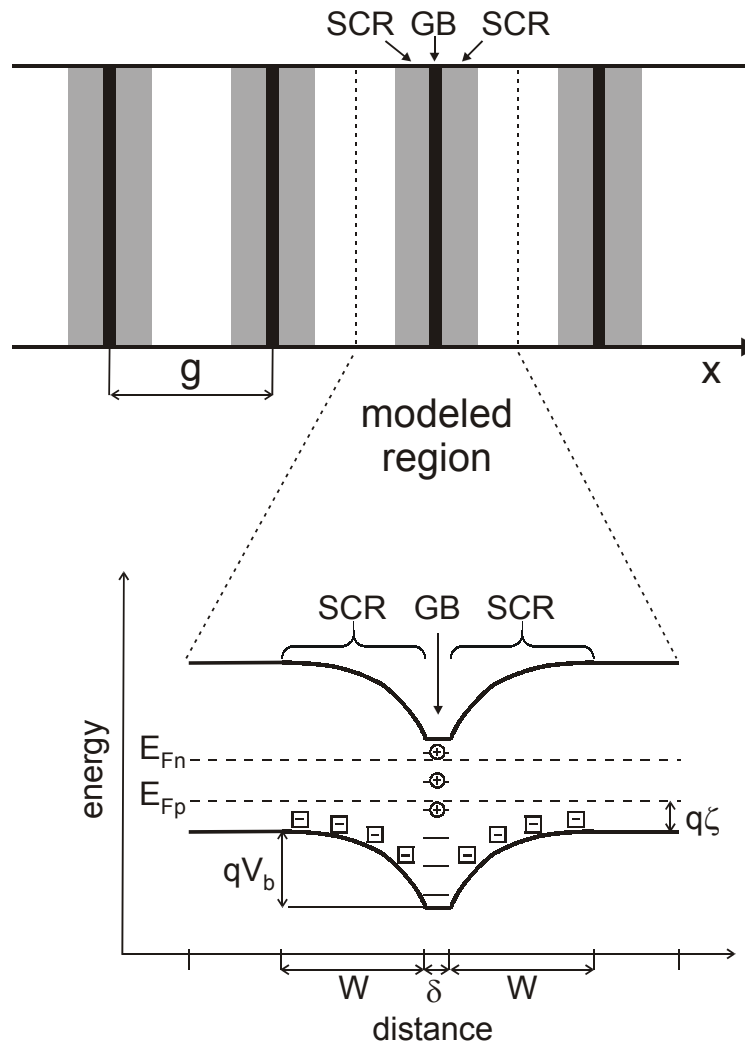
Figure 4.1: One-dimensional picture of a polycrystalline material. Assuming that all grains have the same size, it is sufficient to take the region between the dotted lines to model the electrical properties of the film. The band diagram defines some variables assuming a p-type material.

4.1.2 Electrostatics

To solve Poisson's equation, we have to determine the space-charge density at every position x. Out of the SCRs, the net charge is zero. In the SCRs, assuming that they are *completely depleted*, we have no free carriers, and the charge is given by the dopant ions. Throughout this chapter, I assume p-type material with a doping density N_A, and that all acceptors are ionized, i.e. $N_A = N_A^-$. The amount of charge Q_{GB} at a grain boundary is given by the density of defects, and by the available free charge within the grains, fixed by N_A. To solve Poisson's equation, I assume that the width of the grain boundary is negligible, i.e. $\delta \approx 0$. Thus, the

charge at the GB is an areal charge (in As/cm^2), and the trap density N_t of defect levels has units of cm^{-2}. With all these considerations, the charge neutrality condition for one grain establishes that the areal charge Q_{GB} at the grain boundary must equal the charge (of opposite sign) in the two adjacent SCRs. This condition is given by the equation

$$Q_{GB} = 2qWN_A .\tag{4.3}$$

This equation is valid until the SCR reaches the center of the grains, i.e. until $W = g/2$. In that case, the whole grain is *depleted*, and there are no carriers left to charge the GB. This situation of *total depletion*, is described by the condition $Q_{GB} = qgN_A$, which, replaced in Eq. (4.3) gives the total depletion condition

$$W = \frac{g}{2} .\tag{4.4}$$

If the width of the SCR is smaller than $g/2$, the carrier-capture process stopped before the whole grain was depleted. In that case, all traps are charged, being the limiting quantity the defect density N_t, and we have

$$qN_t = 2qWN_A .\tag{4.5}$$

Having all the charges defined, Poisson's equation becomes

$$\frac{dF}{dx} = -\frac{qN_A}{\varepsilon_0\varepsilon_S} .\tag{4.6}$$

To solve the electrostatic potential Ψ, and the band bending qV_b, we need two boundary conditions for Eq. (4.6): the electric field is zero at the border of the SCRs and, for convenience, $\Psi = 0$ at the borders of the SCRs. Integrating twice Eq. (4.6), the band bending qV_b results in [23]

$$qV_b = \frac{q^2 N_A W^2}{2\varepsilon_0\varepsilon_S} .\tag{4.7}$$

If we have completely depleted grains, $W = g/2$ and Eq. (4.7) predicts that the band bending increases linearly with both N_A and g,

$$qV_b = \frac{q^2 N_A g^2}{2\varepsilon_0\varepsilon_S} .\tag{4.8}$$

On the other extreme, if all traps are filled, Eq. (4.5) gives $W = N_t/2\,N_A$. Replacing this width in Eq. (4.7), we find that qV_b is proportional to $1/\,N_A$ and independent of grain size, following the expression

$$qV_b = \frac{q^2 N_t^2}{8\varepsilon_0 \varepsilon_S N_A}.$$ (4.9)

Between the two extremes of low and high dopings, the actual value of Q_{GB} is unknown *a priori*. The band bending is given by Eq. (4.7), but W must be solved from Eq. (4.3) and a convenient expression of Q_{GB} that contains the sum of the charges of every defect state. The charge of every defect results from the distribution function f multiplied by the density of states found at the defect energy E_t. Assuming N positively charged defects and M charged negatively, the total charge becomes

$$Q_{GB} = q\sum_{i=1}^{N} N_{t,i}(1-f_i) - q\sum_{k=1}^{M} N_{t,k} f_k.$$ (4.10)

In this situation, the band bending is obtained solving numerically Eqs. (4.3), (4.7) and (4.10). Figure 4.2 shows schematically the influence of grain size and doping density on qV_b. For completely depleted grains, we observe the linear dependence of qV_b on N_A. At very high dopings, the band bending qV_b decreases with $1/N_A$. Between the two extremes, we find a maximum. I give quantitative results for qV_b as a function of N_A in the next sections.
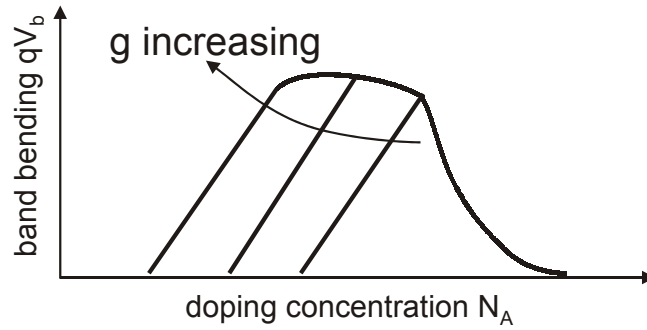

Figure 4.2: The band bending towards a grain boundary shows a maximum when plotted against the doping concentration. At high values of N_A, the band bending qV_b disappears because the space charge regions needed to balance the charge at the grain boundary are very narrow. In the other extreme (at very low values of N_A, qV_b) is negligible because there is no sufficient free charge in the grains to fill the grain boundary. Between both extremes, we have the maximum of qV_b. The width of the maximum is controlled by the grain size.

If one has an energetically continuous distribution of defect states, Q_{GB} must be calculated similarly as in (4.10), but with an integral expression containing the energy distribution of the defect level density in units of $cm^{-2}eV^{-1}$. As shown in a previous work [62], assuming a continuous distribution of defect levels does not change the results of qV_b and its qualitative dependence on N_A and g. Moreover,

including the free carriers in the space charge region has no influence over all the practical range of doping concentrations, i.e. for $N_A > 10^{14}$ cm^{-3} in polycrystalline silicon [62].

4.1.3 Fermi level pinning

The quantity $q\zeta$ shown in Figure 4.1 denotes the distance between the Fermi-level and the band edge of majority carriers. At the grain boundary, $q\zeta$ differs from its value in the center of the grain, exactly by qV_b. At low or at very high dopings, where we have low values of qV_b, the value of $q\zeta$ at the GB approaches the value in the middle of the grain. Thus, for intrinsic material, the Fermi-level approaches the gap center, resulting in $q\zeta \approx E_g/2$ at any position in the grain. For highly doped material, $q\zeta$ is usually smaller than 0.1 eV, corresponding to the position of the Fermi-level given by the doping density. At moderate dopings, $q\zeta$ differs strongly between its value at the GB and in the grain center, due to the significant band bending (see Figure 4.1). In the middle of the grain, $q\zeta$ lies between the valence band and the Fermi-level, corresponding to the moderate doping level. At the grain boundary, $q\zeta$ is still large, like in the intrinsic case, due to the high value of qV_b. This constancy of $q\zeta$ for the wide range of dopings (from intrinsic to moderate dopings), is called "Fermi-level pinning". The Fermi-level at the GB is *pinned* to a fixed position, at about $E_g/2$ above the valence band in p-type silicon. The energy at which the Fermi-level gets pinned is given by the energy of the traps within the bandgap. In silicon, the value $q\zeta \approx E_g/2$ is reached because there is a significant density of trapping states near gap center. If the levels were shallower, the pinning position would also be more shallow.

4.1.4 The grain boundary under illumination

Upon illumination, the generated carriers use the defect levels as recombination sites. Additionally, the states at the GB trap generated carriers, modifying the charge Q_{GB}. Assuming that the recombination at GBs obeys SRH statistics, the charge at the GB must be calculated using (4.10) but replacing f by f_{SRH} (see chapter 2). The continuity equation, which considers the recombination, provides the additional equation needed to solve the additional Fermi-level. To simplify the problem, I neglect any recombination inside the grains, i.e. an infinite

diffusion length inside the grains $L_{eff,mono} = \infty$. This approach is mainly valid for relatively low grain sizes (below 10 μm in silicon), because in electronic-grade material, the number of defects per unit volume inside the grains is surely much smaller than the defect density at the grain boundary. Since $L_{eff,mono} = \infty$, there is no recombination inside the grains, implying that the QFLs are flat throughout the grain, giving $J_p(x) = J_n(x) = 0$, after Eqs. (2.10) and (2.11). Integrating the continuity equation (2.13) for holes between $x = 0$ and $x = g/2$, we find

$$0 = gG - R_{GB} .\qquad\qquad(4.11)$$

This equation says that all the light-generated carriers, flow to the grain boundary and recombine there with a rate R_{GB}. This recombination rate is fixed by G and the grain size g. For a given G, an increase of g means a decrease of the recombination rate because the GB area per unit volume decreases. The recombination rate must be calculated using the Shockley-Read-Hall expression for every defect level. Under illumination, the carrier densities increase. This increase is expressed by the splitting of the quasi-Fermi levels. The higher the generation rate, and the lower the recombination rate, the higher becomes qV^0_{OC}. In fact, qV^0_{OC} is an indirect way to obtain the recombination rate, since R_{SRH} is proportional to $exp(qV^0_{OC}/kT)$ [63].

Since it is possible to write the quantities n, p, n_1 and p_1 intervening in R_{SRH} (see sections 2.1 and 2.2.2) as a function of the unknowns qV_b and qV^0_{OC}, both quantities must be solved using Eqs. (4.3), (4.7), (4.10) and (4.11). Figure 4.3 shows qV_b and qV^0_{OC} in polycrystalline silicon with $g = 1$ μm, as a function of the dopant atoms concentration N_A. The carrier generation rate G is the parameter taken to calculate the different curves, measured in suns (1 sun = 10^{20} cm^{-3}s^{-1}). The calculation of G is described in section 5.1. The different values of G are taken because, as shown below, useful information about the behavior of the GB recombination can be extracted from an analysis at different illumination intensities. The calculations involved in Figure 4.3 consider five acceptor and five donor-type defect levels distributed symmetrically around the gap center with 100 meV between each other, having an acceptor and donor-type defect at each energy value. Each defect level has a concentration $N_t = 10^{11}$ cm^{-2} (resulting in a total concentration of 10^{12} cm^{-2} counting the 10 defects). The QFL splitting is low at low doping concentrations, because the function R_{SRH} has a maximum value for Quasi-

Fermi levels that enclose the defect levels [63]. Indeed, at low dopings the QFL of majority carriers lies closer to the gap center (and hence to the defect levels, which lie around the gap center) than at higher doping levels. Additionally, the Fermi-level pinning below a certain value of N_A makes that qV^0_{OC} stays at its minimum value below that doping value, as seen in Figure 4.3. The whole behavior of qV^0_{OC} is determined by the band bending, because it controls the pinning.
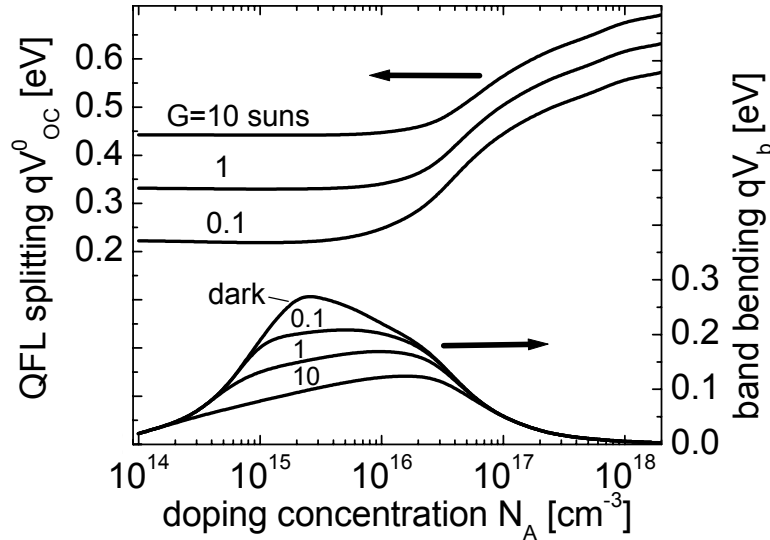

Figure 4.3: The QFL splitting, which can be thought as the maximum open circuit voltage a solar cell can reach, shows its lowest values at low doping concentrations. The increase of qV^0_{OC} in about 0.2 eV from $G = 0.1$ to 10 suns, shows that the concentration of light strongly determines the open circuit voltage of a solar cell.

Figure 4.3 shows also that the band bending qV_b decrease with the generation rate, because the generated carriers flow towards the grain boundary, interacting with the defect levels by occupying them, or recombining with other carriers. The occupancy of the defects means that the GB charge will be partly neutralized, which results in a decrease of the band bending. Hence, the whole effect is proportional to G, because the higher is G, the higher is the neutralization, and the lower the resulting qV_b.

From Figure 4.3 we can say that, as a rule of thumb, at *low doping levels*, qV^0_{OC} increases around 0.1 eV for every order of magnitude increased in G. At *high doping levels*, we only obtain 0.05 eV (for the same increase in G). This result is important for the design of solar cells with polycrystalline silicon: with its high light trapping ($> G$), thin-film solar cells profit from this increase of qV^0_{OC} with G, enabling the realization of solar cells with higher V_{OC}'s than thick cells.

Now I discuss how qV^0_{OC} changes with grain size and defect density. The same calculus method as in the previous analysis is utilized, but considering N_t instead of G as parameter. The number, type, and energetic position of the defect levels at the GB utilized in this case are the same as those of Figure 4.3. Since these calculations consider 10 defects in total, we have a total GB defect density N_{GB} = $10N_t$. Figure 4.4 shows a linear increase of qV^0_{OC} with $log(g)$, calculated at a generation rate G = 1 sun,[5] and with the values of N_{GB} indicated near each line. These curves are calculated with a doping level $N_A = 10^{14}$ cm^{-3}, which places us at the left part of Figure 4.3, where total depletion is present.

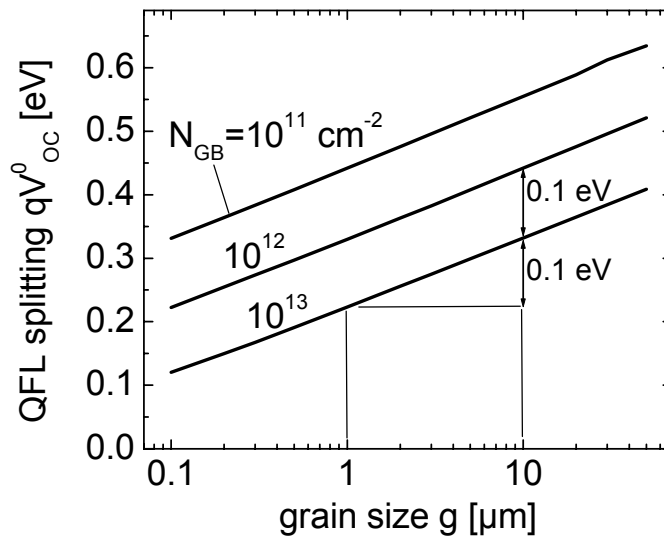Figure 4.4: The splitting of the Quasi-Fermi levels qV^0_{OC} (calculated with G = 1 sun) depends linearly on $log(g)$. The lines have a slope of 0.1 eV per order of magnitude increased in g. A decrease by one order of magnitude in the total defect density N_{GB} has the same effect as increasing the grain size by an order of magnitude. To obtain the maximum qV^0_{OC}, one can either reduce the defect density at the grain boundaries, increase the grain size, or both.

As shown in Figure 4.4, the lines give a slope of 0.1 eV by order of magnitude increased in g. A decrease in N_{GB} (or N_t) of one order of magnitude, increases qV^0_{OC} by the same amount than increasing g by an order of magnitude. This behavior has a simple physical explanation: for a given defect density N_t, increasing the grain size means a reduction of grain boundary charge *per unit volume*, which has the same effect as reducing N_t at a fixed g. Thus, a solar cell's open-circuit voltage

---

[5] In a 10 μm-thick silicon layer, this value is reached for example by shining 100 mW/cm^2 with a photon energy of 1.3 eV. Such photon energies close to the bandgap of silicon of 1.12 eV must be chosen in order to obtain the spatially homogeneous generation rate required by the present model.

profits from an increase of g, and also from a reduction of N_t. These two alternatives were discussed in chapter 3, where the open-circuit voltage of solar cells increased with g, and also with a low recombination velocity S_{GB}, which implied low values of N_t.

As shown in section 5.1.3, the linearity of qV^0_{OC} as a function of N_t or N_{GB} (on a logarithmic scale), does not hold strictly at doping levels $N_A \gg 10^{14}$ cm^{-3}, because of the increasing influence of the band bending qV_b on the recombination rate R_{GB}. However, the qualitative result is the same at high values of N_A: large grains and low defect densities are needed to reach high values of qV^0_{OC}.

The next section considers that we contact the poly-Si to an external circuit, producing a current flow of carriers along grains. The resistivity that arises from that current shows strong differences when compared respect to a monocrystalline material.

4.1.5 Resistivity of a polycrystalline material

The transport of carriers from one grain to its neighbor has three stages: the first one is the flow through the neutral part of the grain, secondly through the SCR, and thirdly through the GB. Thus, to obtain the resistivity of a polycrystal, the continuity equations must be solved considering the equivalent circuit shown in Figure 4.5.

neutral region   SCR   GB
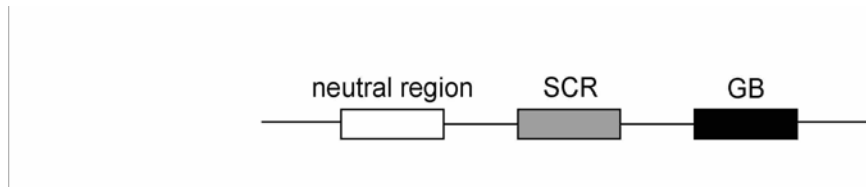
Figure 4.5: Equivalent circuit to model the resistivity of a polycrystalline grain.

In the neutral region, the resistivity ρ is given by the mobility μ_p of majority carriers (considering p-type material) and the hole concentration p_0, by the equation

$$\rho = \frac{1}{q\mu_p p_0} .$$
(4.12)

In the present model, I neglect the resistivity of the neutral part, which is a reasonable assumption for moderately to highly doped material. In low-doped

material this assumption has no sense, since there is no neutral region inside the grains.

Here I consider the width δ of the grain boundary, which defines the GB as a region with specific transport parameters. As noted by Grovenor [20], the most common assumption is that the boundary is a narrow region of high defect density and particular transport parameters. Under this assumption, the GB has its own carrier density and mobility.

Assuming that the voltage applied to each grain boundary is smaller than V_t, i.e. under the so-called small signal regime, the solution of Poisson's and continuity equations define the resistivity ρ by the equation[6]

$$\rho = \frac{1}{q\mu_{pGB}p_{GB}}\frac{\delta}{W} + \frac{1}{q\mu_p p_0}\frac{\sqrt{\pi}erfi\left(\sqrt{V_b/V_t}\right)}{2\sqrt{V_b/V_t}}, \tag{4.13}$$

where μ_{pGB} and p_{GB} are the mobility and the hole concentration *at* the GB, respectively, and p_0 the concentration of holes in the middle of the grain. The resistivity has two terms: the first one corresponds to the grain boundary, while the second term belongs to the SCR. In grains with small SCRs, the ratio δ/W is large, and Eq. (4.13) predicts that the GB dominates the resistivity. To understand the SCR component, we have to give a look at the function containing the ratio V_b/V_t in Eq. (4.13). Figure 4.6 shows a plot of this function (solid line). At small values of V_b, the function tends to 1, which means that the SCR resistivity is given by $1/q\mu_p p_0$, which is the value of the resistivity in a neutral grain. At high band bendings, the function increases sharply and goes parallel to $exp(V_b/V_t)$, which is given by the dashed line.

In chapter 6, I model the grain size dependence of the resistivity of laser-crystallized silicon using Eq. (4.13).

---

[6] Obtained from Ref. [64], by replacing properly the Dawson's integrals by the error function *erf*.

$$\frac{\sqrt{\pi}}{2} \frac{erfi\left(\sqrt{V_b/V_t}\right)}{\sqrt{V_b/V_t}}$$
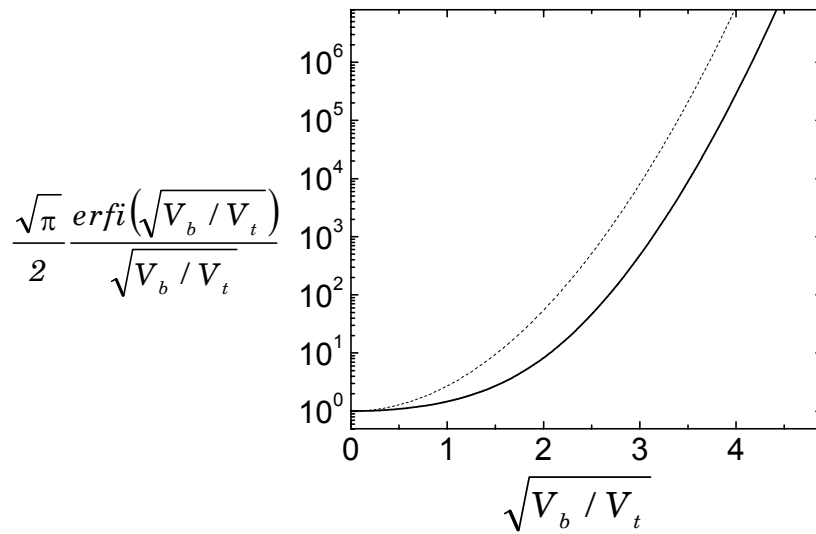
Figure 4.6: The resistivity of the space-charge region near grain boundaries in poly-Si is proportional to the function plotted here (see Eq. (4.13)). The higher the band bendings (high V_b), the higher are the values of this function, and the resistivity increases according to Eq. (4.13). The dashed line is given by the function $exp(V_b/V_t)$, for comparison.

The resistivity explained so far considers an infinitely thick polycrystalline material. The situation in practice is that one has a film of material, with a thickness usually of the order of a micrometer. Surprisingly, this finite thickness is rarely considered in publications that study the resistivity of thin-film silicon. In the next section, I treat the problem of the resistivity of a thin film.

4.2 Transport in thin polycrystalline films

Thin films show higher resistivity than bulk material due to surface scattering. When analyzing resistivity data in thin poly-Si films, one has to find out if the material's resistivity is masked by surface effects or not. During my work I prepared thin films of laser-crystallized silicon with thicknesses between 100 and 400 nm. In this section, I investigate if surface effects on resistivity can be neglected or not.

The electrical resistivity in any conducting media is determined by the scattering events suffered by electrons or holes. In semiconductors, carriers scatter with lattice atoms, impurities, and with other carriers [65]. The *scattering time* τ is an average time between two scattering processes occurred to the same carrier. In that time, a carrier traveling at a mean velocity v through a bulk semiconductor,

travels a mean distance $l = \tau v$, defined as the *mean free path*. The resistivity of the semiconductor is proportional to the scattering time (or, to the mean free path).

At semiconductor surfaces, we find reordered atoms, segregated impurities and oxides, which are all sources for carrier scattering. Surface scattering will then increase the resistivity of the surface-layer system. For semiconducting films of sufficient thickness, the amount of carriers near the surfaces is negligible compared to the bulk carrier density, and the measured resistivity becomes nearly equal to the bulk value. If, however, the film thickness is of the order of the mean free path in the bulk, most of the carriers reach the surface in their random movement, and suffer scattering there. The measured resistivity is then a function of the film thickness d. A study of these effects is given in textbooks [67], showing that surface scattering effects are negligible if $l/d << 1$. The mean free path will now be calculated for the laser crystallized films used in this work. Considering the bulk carrier mobility μ_p and carrier concentration p, the mean free path is given by

$$l = \mu_p \frac{h}{q} \sqrt[3]{\frac{3}{8\pi} p} \; . \qquad\qquad (4.1)$$

Since the films characterized are undoped, the carrier concentration is rather low. Therefore, considering $p \leq 10^{16}$ cm^{-3}, and even with a high value $\mu_p = 1000$ cm^2/Vs, the mean free path becomes $l \leq 4.4$ nm. With a film thickness of 100 nm, we obtain $l/d \leq 0.044$, and the condition $l/d << 1$ is satisfied. This result implies that surface scattering effects can be neglected.

Surfaces can also affect carrier transport if one considers electrical fields present at surfaces. Such electrical fields appear when bulk carriers get trapped at defect states at the surfaces, charging them and leaving a SCR towards the bulk (similarly to the charging of a grain boundary). Normally, this charging leads to a band bending and a variable carrier concentration from surface to bulk. The reduction of the number of carriers near the surface, increases the measured resistivity. However, since the films studied are very thin, and undoped, no significant band bendings can build up, making this effect negligible.

5 Simulation and modeling of *pin* solar cells

This chapter presents a numerical model for polycrystalline *pin* solar cells. The aim of the simulations is to understand how the excellent efficiencies obtained with fine-grained, *pin* solar cells of Table 3.1 could be reached. The principal elements incorporated by the model are three: grain boundaries with defect levels in the band gap, contacts where carriers are extracted but also recombine, and a spatially-dependent generation rate profile (in the previous chapter, we considered only a spatially homogeneous generation rate). The simulations allow me to compare the doping dependence of V^0_{OC} obtained from the QFL splitting, with the actual V_{OC} in solar cells, and to establish *limits* to η and V_{OC} in cells with recombination at contacts. Secondly, I elaborate a new *analytical* model for the current/voltage equation of the *pin*-cell. The model is then utilized to fit experimental data of fine-grained solar cells.

5.1 Numerical model

5.1.1 Geometry and boundary conditions

Figure 5.1 shows the geometry of the *pin*-cell. The two contacts enclose the semiconducting layers. The top contact is transparent, while the bottom contact is a light-reflecting aluminum contact. Thus, we have two highly doped (p^+, n^+) layers next to the contacts, and an intrinsic (i), or low doped (p-layer) in the middle. The left edge constitutes the grain boundary, which is assumed to be a flat surface, and the right edge is the grain center.

The boundary conditions for electrons and holes at all the four edges of the domain are the following:

1. At the interface between the p^+ or n^+ layers to the contacts, carriers have a contact recombination velocity S_C. The electrostatic potential at these surfaces is set according to the bias V at one contact, and to the reference potential at the other one.

2. The grain center, at $x = g/2$, is a symmetry surface, imposing that the spatial derivatives of the carrier concentrations and the potential must be zero along that edge.

3. At the grain boundary ($x = 0$), the carrier concentrations and the electrostatic potential are given by the recombination rate R_{GB}, and the charge Q_{GB} of the defect states. Previous simulations considered a spatially constant surface recombination velocity along the grain boundary line (See Refs. [72] and [73]). Edminston et al. criticized the lack of physical rigorousness in this assumption, and simulated np cells considering a spatially dependent surface recombination velocity [74]. The present model considers also a spatially dependent surface recombination rate and charge obeying Shockley-Read-Hall (SRH) statistics. The recombination centers are five acceptor and five donor-type defect levels distributed symmetrically around the gap center with 100 meV between each other, having an acceptor and donor-type defect at each energy value. The density N_t of each defect is assumed equal. Since we have 10 defects, the total GB defect density is $N_{GB} = 10N_t$.
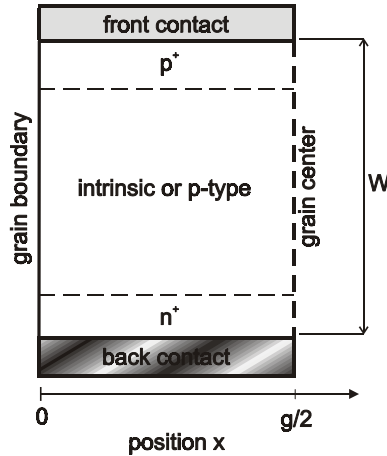

Figure 5.1: Model of the *pin* solar cell assumed in the simulations, showing the grain boundary at $x = 0$, the grain size g, and the cell thickness W.

For the recombination within the grains, I assume a SRH field enhanced recombination model [75] with a single trap located at the gap center, radiative- and Auger recombination. The field enhanced SRH recombination is a modified version of the SRH recombination. It allows minority carriers to tunnel quantum-mechanically from the bands to the recombination center in the gap. This tunneling

can only take place in regions where the valence and conduction bands are spatially close to the recombination center, such as high electric field regions (i.e. space-charge regions) [75]. The equation of this recombination rate is formally equal to R_{SRH} given by Eq. (2.19), but considering field-dependent capture cross sections. At zero field, the capture cross sections assume their standard values (see below). The profile of the optical generation rate in the device is obtained with the optical simulator for solar cells SUNRAYS, as explained in Appendix A. I assume an illumination intensity of 100 mW/cm^2 under an AM1.5 global spectrum. Light trapping is considered by an aluminum back-contact reflector. The carrier mobilities within the grains are modeled with the well-known doping- and electric field-dependent models for monocrystalline silicon [76]. The parameters for all simulations presented here are $W = 1.14$ μm, $g = 3$ μm, capture cross sections $\sigma_n = \sigma_p = 10^{-15}$ cm^2 (at zero-field) for the defect levels at the GB as well as in the bulk, and a thermal velocity of 10^7 cm/s. The doping density at the p^+- and n^+-layers is 10^{19} cm^{-3}.

To solve the semiconductor equations in the two-dimensional space, I developed a simulator that uses the finite difference method. The idea behind the technique is to replace the continuous material by a spatially discrete number of points, and to calculate all the required variables at these points. Figure 5.2 shows a typical finite difference mesh utilized to simulate the *pin* cell of Figure 5.1. To permit a refinement of the calculations in some regions of the cell where the variables vary strongly, such as the grain boundary or at the junctions, the spacings between mesh points are not constant. At each point *(i,,j)*, we have a particular *x*-spacing a_i and *y*-spacing b_i. This mesh has 20 divisions in the *x*-direction (index *i*), and 70 divisions in the y-direction (index *j*), giving a total of 1400 mesh points. The matrices involved in the solving process have $1400^2 \times 1400^2 = 1.96$ million elements. Since these matrices are sparse, i.e. they contain much more zeros than non-zero elements, the solving process is done by sparse-matrix solvers. The computer and programming language utilized to perform the simulations need about a second to solve each matrix. The total calculus time to calculate a complete J/V curve ranges between 1 and 2 hours.
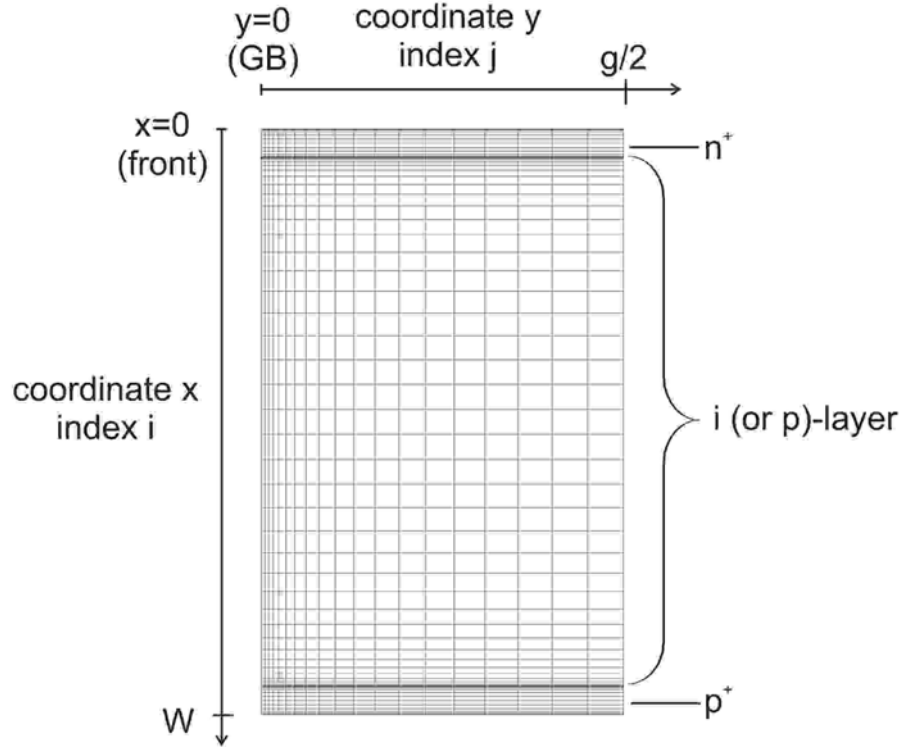
Figure 5.2: Finite difference mesh utilized in this work to simulate *pin* cells in two dimensions. The mesh spacings refine at regions such as the grain boundary (GB) to allow a higher numerical accuracy in that region.

The unknowns at each point *(i,j)* of the mesh are three: the electrostatic potential $\psi_{i,j}$, and both carrier concentrations $n_{i,j}$ and $p_{i,j}$. To solve numerically the semiconductor equations, we must adopt a 'discretized version' of each equation, where the variables are expressed at each mesh node *(i,j)*. The discretization of Poisson's equation is based on a first-order Taylor-series expansion of the derivative of the electrostatic potential ψ at each mesh point. For example, the first derivative of the potential in *x*-direction at the mesh point *(i,j)* is given by $(\Psi_{i+1,j} - \Psi_{i,j})/a_i$. The discretized Poisson equation is then given by [76]

$$\frac{\dfrac{\Psi_{i+1,j} - \Psi_{i,j}}{a_i} - \dfrac{\Psi_{i,j} + \Psi_{i-1,j}}{a_{i-1}}}{\dfrac{a_i + a_{i-1}}{2}} + \frac{\dfrac{\Psi_{i,j+1} - \Psi_{i,j}}{b_j} - \dfrac{\Psi_{i,j} + \Psi_{i,j-1}}{b_{j-1}}}{\dfrac{b_j + b_{j-1}}{2}} =$$
$$-\frac{q}{\varepsilon_s}\left(p_{i,j} - n_{i,j} + p_{t_{i,j}} - n_{t_{i,j}} + N_{D_{i,j}}^+ - N_{A_{i,j}}^-\right) \qquad (5.2)$$

The truncation error done by discretizing this equation is proportional to a_i^2, b_i^2 [76].

The two-dimensional continuity equations for electrons and holes at the mesh node (i,j) are given by [76]

$$\frac{1}{q}\text{div}\mathbf{J}_{n\,i,j} = -\left(G_{i,j} - R_{i,j}\right), \text{ and}$$

$$\frac{1}{q}\text{div}\mathbf{J}_{p\,i,j} = \left(G_{i,j} - R_{i,j}\right), \tag{5.3}$$

where the current densities $\mathbf{J}_n$ and $\mathbf{J}_p$ are two-dimensional vectors. The expansion of these equations expressing each component of $\mathbf{J}_n$ and $\mathbf{J}_p$ as a function of ψ, n and p escape to the aim of this chapter. They may be consulted for example in Ref. [76]. Here, I show only a part of this expansion process. The discretization of the continuity equation for electrons, for example, is written as [76]

$$\frac{1}{q}\left(\frac{J_{n,x_{i+1/2,j}} - J_{n,x_{i-1/2,j}}}{\dfrac{a_i + a_{i-1}}{2}} + \frac{J_{n,y_{i,j+1/2}} - J_{n,y_{i,j-1/2}}}{\dfrac{b_j + b_{j-1}}{2}}\right) = -\left(G_{i,j} - R_{i,j}\right), \tag{5.4}$$

where, for example, the x-component at $(i+1/2,j)$ is given by

$$J_{n,x_{i+1/2,j}} = -qV_t\left(\mu_{n\,i+1,j} + \mu_{n\,i,j}\right)\frac{n_{i+1}B\left(\dfrac{\Psi_{i+1,j} - \Psi_{i,j}}{V_t}\right) - n_i B\left(\dfrac{\Psi_{i,j} - \Psi_{i+1,j}}{V_t}\right)}{a_i}, \tag{5.5}$$

being $B(u)$ Bernoulli's function, given by $B(u) = x/[\exp(x)\text{-}1]$. The use of the Bernoulli function instead of a linear Taylor-series expansion to express the derivatives involved in J_n, is known as the *Scharfetter-Gummel Approach*. This approach avoids numerical instabilities that would take place if the electron concentrations were allowed to vary linearly between two mesh points [76]. The truncation error of Eq. (5.7) is proportional to a_i, b_j [76].

The solving process starts estimating values for $\psi_{i,j}$, $n_{i,j}$ and $p_{i,j}$ at all points, and replacing these estimates in the discretized Poisson and continuity equations. After replacing the estimates, the right-hand side of the semiconductor equations at a given point, give a different value as the left-hand side, providing the error of the estimations. The simulation program minimizes that error, using a Newton-Raphson algorithm. Specific details concerning the simulation technique itself are explained, for example, on page 203 in Ref. [76].

5.1.2 Doping level of the i-layer

In *pin* solar cells, it is common to refer to the i-layer as a low-doped layer, rather than rigorously to an intrinsic layer. The advantage of doped layers is not clear up to now. Beaucarne et al. showed that V_{OC} increases by doping the base of their *pn* solar cells made from fine grained silicon of 12 μm thickness [71]. Researchers of fine-grained Si cells at Neuchatel obtained their best results taking a nearly intrinsic i-layer, avoiding any doping [68]. In contrast, the cells made at Kaneka Corp. have an i-layer doping between 10^{15} and 10^{16} cm^{-3}, according to their measurements and simulations (See Refs. [69] and [70]). There are therefore contradictory statements in the literature about the benefits of doping for V_{OC} or η. The model presented here solves this situation, by simulating cells with increasing i-layer doping.

5.1.3 Simulation results

Figure 5.3 shows that V_{OC} *increases* with the doping of the i- (or p)-layer. The parameter of each simulation curve is the recombination velocity S_C at contacts. These simulations were obtained with a thickness $W = 1.14$ μm, a grain size $g = 3$ μm, and the defect densities and energies described above. The bulk defect density N_{BULK} is set to $N_{BULK} = 10^{14}$ cm^{-3} in these simulations. The advantage of increasing the doping to reach high values of V_{OC} is based on the shift of the QFL for holes to the valence band due to the doping, which implies a reduced SRH-recombination at the recombination centers *around gap center*. The smaller recombination rate leads to the high V_{OC}.

However, Figure 5.3 shows also that at high doping densities the cells are very sensitive to contact recombination S_C: at high S_C values of 10^6 cm/s, until an i (or p)-layer doping of about 5×10^{16} cm^{-3}, the cells remain efficient; but with higher dopings, η decreases. How can we explain that decrease? Note that if one increases the doping of the i-layer to the value of either the p^+ or n^+ layers (i.e. to 10^{19} cm^{-3} in our case), a *np* junction at the front side of the cell is formed. In this case, the electric field is present only in the depletion region of the *np* junction. The thickness of the depletion region is much smaller than the depletion region of the *pin* cell, which was conformed by the i-layer. Thus, the carrier collection by the electric field

is weaker and is easily affected by S_C. As a consequence, at large S_C-values, the values of the short circuit current density J_{SC} and V_{OC} degrade, resulting the poor efficiencies shown in Figure 5.3. Although S_C was taken *equal* for the back and front contacts, simulations[7] performed using *unequal* front and back S_C showed that the contact that actually harms V_{OC} is the back contact. The explanation for this is that minority carriers generated deep in the cell must travel a longer distance to reach the junction than those generated in the thin n-type front layer, increasing the probabilities to recombine at the back contact.
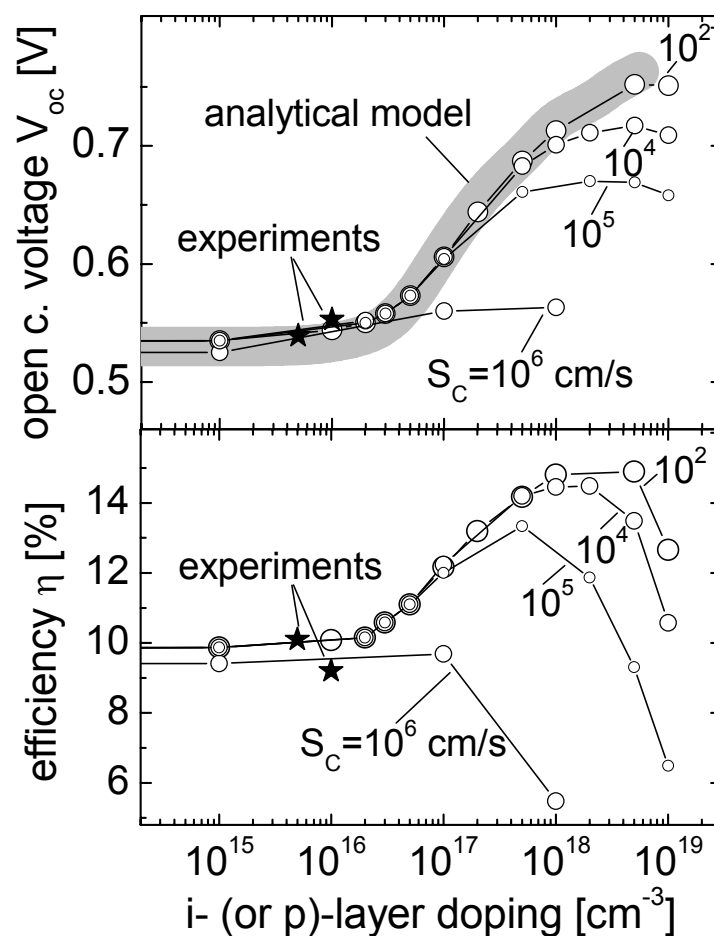

Figure 5.3: cAt low values of the recombination velocity at contacts S_C, the best cells are found at a doping of the i- (or p)-layer of about 10^{18} cm^{-3}, reaching an efficiency $\eta = 14.8$ %, and an open circuit voltage $V_{OC} = 0.75$ V at $S_C = 100$ cm/s. If such low values of S_C cannot be reached, it is safer to stay at low doping densities (below 10^{16} cm^{-3}), where η reaches $\eta = 10$ %, as confirmed by the experiments (stars). The thick solid line comes from the analytical model for qV^0_{OC} of chapter 4, showing a very good agreement with the simulations.

---

[7] performed also with the simulation program developed in this work.

Figure 5.3 shows that maximum cell efficiencies η = 14.8 % and open circuit voltages V_{OC} = 0.75 V are obtained at S_C = 10^2 cm/s and dopings around 10^{18} cm^{-3}. At this doping level, the cell must already be understood as a *np*-type cell, because the electric field extends only over a narrow region at the front of the *np* junction formed. At the maximum efficiency point, the simulations give a short circuit current density J_{SC} = 24.9 mA/cm^2, a fill factor *FF* = 79.6 %, and an ideality factor n_{id} = 1.21. The maximum efficiency is mainly limited by the short-circuit current density that can be extracted from this 1.14 μm thin cell. However, this small thickness enables the high V_{OC} (this behavior was explained in Ref. [77]). Behind the maximum of η shown in Figure 5.3, V_{OC} and η drop due to the increasing Auger and radiative recombination in the bulk.

What output parameters would the record solar cell (with η = 14.8 %) have with no GB recombination? A simulation of the same cell with no GB recombination (N_t = 0 cm^{-2}) yielded $η^0$= 17.4 %, V^0_{OC} = 0.80 V, J^0_{SC} = 25.4 mA/cm^2, and FF^0 = 84.4 % (here, the superscript '0' indicates the condition of zero GB recombination). As explained in Ref. [78], the limit value V^0_{OC} is given by the Auger recombination process, being V^0_{OC} = 0.80 V possible at 10 suns in this thin cell. Since the absence of the grain boundary turns the problem one-dimensional, it was possible to verify the value of $η^0$ with the one-dimensional commercial simulation program PC1D [88]. A comparison of both simulations show an absolute deviation smaller than 0.22 % in efficiency.

The thick, grey curve in Figure 5.3 shows the results obtained from the simple one-dimensional model for qV^0_{OC} presented in chapter 4, which assumes isolated grains *without any contacts or junctions*, and only GB recombination. This curve was calculated assuming the same grain size and defect states at the grain boundary as used in the numerical simulations mentioned above. The generation rate (considered to be spatially constant within the model of chapter 4) was set to the spatial mean value of the actual generation rate profile needed in the simulations. Despite the strong simplifications involved in it, we observe an excellent agreement between the simulations with low S_C, and the results of the simple model of chapter 4.

Turning to the behavior of the grain boundary, the simulations corresponding to Figure 5.3 revealed that the band bendings qV_b at the GB remain very low, implying that the GB barriers are low. These low GB barriers are consequence of the high generation rate of the order of 10 suns, typical for such thin cells with light trapping; and the low defect density. The maximum value of the band bending under illumination is 95 meV, and 160 mV in the dark (at a p-layer doping of $p = 10^{16}$ cm^{-3}). As shown by the stars in Figure 5.3, the experimental data from Ref. [69] (filled circles) agree with the simulations. The low defect density of 10^{11} cm^{-2} chosen for the simulations, implies low recombination velocities S_{GB} at the GB (see Eq. (4.2)). Only such low values of S_{GB} can explain the high open circuit voltage, and excellent efficiency of the experimental data. The simulations give a spatial mean of S_{GB} that ranges with doping from 1100 to 300 cm/s, at i-layer dopings from 10^{15} and 10^{16} cm^{-3}, respectively. These values are in agreement with the theory presented in chapter 3, which predicted S_{GB} to be around 1000 cm/s for these fine-grained *pin*-cells.

Figure 5.4 shows the dependence of V_{OC} and η on the total GB trap density N_{GB} ($N_{GB} = 10N_t$). The simulations assume a thickness $W = 1.14$ μm, a grain size $g = 3$ μm, and an i-layer doping of 5×10^{16} cm^{-3}, with the same amount, type and energetic position of the GB defects utilized in the previous simulations. In order to analyze the effect of the recombination in the bulk and at the grain boundary alone, the contact recombination velocity S_C was set to a low value $S_C = 100$ cm/s. The parameter utilized here is the bulk trap density N_{BULK}. As expected, we observe that an increase in N_{GB} and N_{BULK} reduces V_{OC}, due to the higher recombination rate. Consequently, the efficiency η also decreases with N_{GB} and N_{BULK}, as shown in Figure 5.4. As shown in Figure 5.4, an absolute increase of 3 % in efficiency is achieved by reducing the defect density from $N_{GB} = 10^{11}$ to 10^{10} cm^{-2}, at low values of N_{BULK}.

The grey continuous line in Figure 5.4 comes form the analytical model for qV^0_{OC} of chapter 4, calculated assuming the same grain size and amount and position of defect states at the GB of the numerical simulations. The generation rate is equal to the spatial mean value of the actual generation rate profile needed in the simulations.
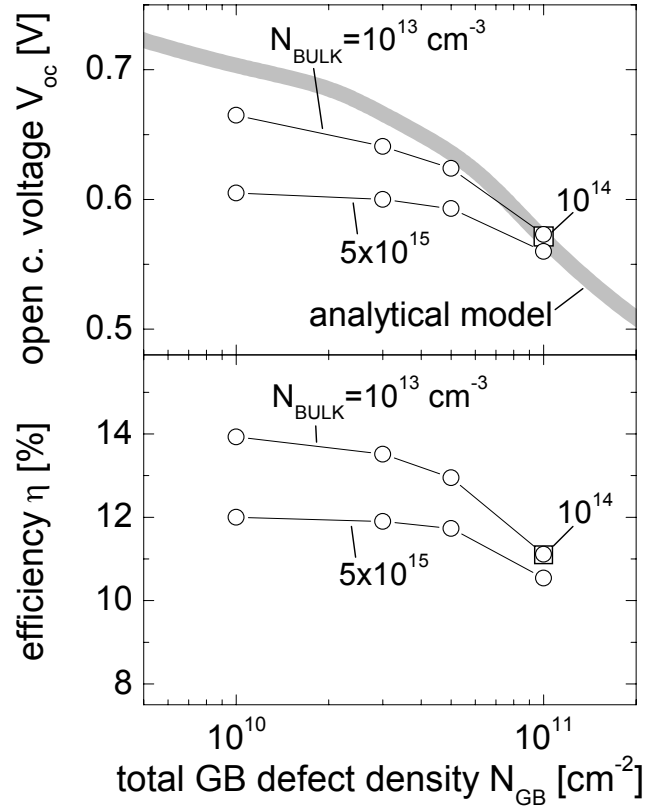
Figure 5.4: These simulations open circuit voltage V_{OC} and cell efficiency η in a 1 μm thick cell with a grain size of 3 μm, show that V_{OC} and η decrease with the grain boundary defect density N_{GB} and with the bulk defect density N_{BULK}. At *high* values of N_{GB}, N_{BULK} shows only a weak influence on V_{OC} and η. At *low* values of N_{GB}, N_{BULK} dominates V_{OC} and η. The grey continuous line comes form the analytical model for qV^0_{OC} of chapter 4, establishing the limit of V_{OC} at $N_{BULK} = 0$.

Figure 5.4 also shows that at the *highest* bulk defect density $N_{BULK} = 5x10^{15}$ cm^{-3} and $N_{GB} < 5x10^{10}$ cm^{-2}, V_{OC} (and therefore η) is almost independent of N_{GB}, indicating that bulk recombination dominates the output parameters of the cell. If N_{BULK} is *low*, for example at $N_{BULK} = 10^{13}$ cm^{-3}, we find a dependence of V_{OC} on N_{GB}. If $N_{GB} > 5x10^{10}$ cm^{-2}, the influence of N_{BULK} on V_{OC} and η vanishes, and at $N_{GB} = 10^{11}$ cm^{-2}, almost no influence of N_{BULK} is observed. At this GB defect density, the cell's output parameters are ruled by the grain boundary alone (provided N_{BULK} does not exceed too much the value $N_{BULK} = 5x10^{15}$ cm^{-3}). The value of N_{GB} at which this changeover from bulk to GB recombination occurs, must depend on the grain size, and the bulk trap density. This is the changeover explained in section 3.3 with the model for $L_{eff,poly}$: at high values of the bulk diffusion length $L_{eff,mono}$, i.e. low N_{BULK}, $L_{eff,poly}$ (and therefore V_{OC} and η) is only dominated by the GB recombination

parameters and the grain size. At low values of $L_{eff,mono}$ (high N_{BULK}), $L_{eff,poly} \approx L_{eff,mono}$, independently of the GB recombination parameters and the grain size.

Now we analyze the ideality factors of the simulated cells. The following analysis of n_{id} is made with ideality factors extracted from the J(V) curves corresponding to the simulations with $S_C = 10^2$ cm/s of Figure 5.3. The simulations reveal that the ideality factors n_{id} (calculated at $V = V_{OC}$) show a *minimum* that depends on the p-layer doping. Figure 5.5 shows a decrease of n_{id} with the doping level from $n_{id} \approx 1.8$ to $n_{id} \approx 1.2$, and then a rapid increase reaching $n_{id} \approx 2.0$ at the highest doping level. Simulations with doping levels below 10^{15} cm^{-3} (not shown in Figure 5.5), also showed $n_{id} = 1.8$. It is possible to explain the observed behavior of n_{id} with doping using the double-diode model presented in chapter 3: at low doping levels, the cells are *pin*-type, i.e. the cells are mainly a space-charge region (SCR). In this case, the double-diode model predicts a value of the ideality factor $n_{id} = 2$, which is close to the value provided by the simulations of $n_{id} = 1.8$. The discrepancy between both values stems from the fact that the double-diode model describes *pn* junctions, and not *pin* junctions. The next section proves that $n_{id} = 1.8$ is indeed a typical value for *pin* cells. Turning to Figure 5.5, we observe that as the doping increases, we obtain a *np* junction, and n_{id} reaches a minimum value $n_{id} = 1.2$ at a doping around 10^{18} cm^{-3}. Since, according to the double-diode model, $n_{id} = 1.0$ if the cell is dominated by bulk recombination, the value $n_{id} = 1.2$ indicates that there is a slight influence of the SCR recombination on the J(V) curves of the modeled cells.

Figure 5.5 also shows that n_{id} increases at higher dopings than 10^{18} cm^{-3}, reaching $n_{id} = 2.0$ at 10^{19} cm^{-3}. In this case, the double-diode model suggests that this value reflects a high recombination in the SCR. Why does the SCR play such an important role being the SCR so small at high doping levels? At high doping levels, the field-enhanced SRH recombination in the SCR becomes important because of the high electric field in the SCR. This recombination mechanism explains therefore the value $n_{id} = 2.0$ given by the simulations. We may suspect that since Auger recombination does also play an important role at high doping levels, the value $n_{id} = 2.0$ could be caused by this recombination mechanism. However, this is not the case, since a *np* cell dominated by Auger recombination must show $n_{id} = 1.0$ [79]. Therefore, we conclude that $n_{id} = 2.0$ is fixed by the SCR recombination.
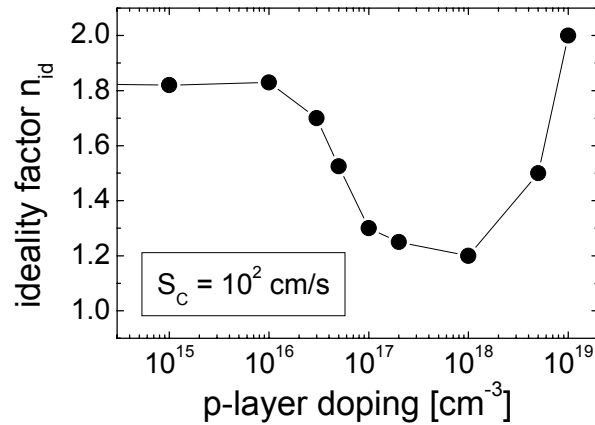
Figure 5.5: Ideality factors n_{id} extracted from the current/voltage characteristics of the simulations shown in Figure 5.4, at a contact recombination velocity S_C = 100 cm/s. The ideality factor n_{id} has a minimum of n_{id} = 1.2 at a doping of 10^{18} cm^{-3}.

As a closing (but important) remark to the present discussion, I show that n_{id} is related to η. Observing Figure 5.5 and Figure 5.3, we note that the minimum of n_{id} takes place at the same doping level of the maximum efficiency η! This finding strongly supports the results found in chapter 3 with the simple double-diode model, which show that the highest values of V_{OC}, *FF* (and therefore η) are only obtained when n_{id} approaches the value n_{id} = 1.0.

5.2 The analytical current/voltage equation of the *pin*-cell

Some models for the J(V) equation of the *pin* solar cell arose in the past (See Refs. [80] and [81]). However, these models were subjected to different limitations. Crandall derived a model for amorphous silicon (a-Si) solar cells and established simple relations between cell output parameters and material properties [80]. He pointed out that his solution for the cell's current cannot be used to calculate the complete current/voltage characteristic because it neglects diffusion currents. Okamoto et al. formulated a more general model for a-Si cells that considered both, drift and diffusion currents [81]. However, their current/voltage characteristic has not a closed form, and the solutions must be found numerically, losing the physical insight achievable using closed-form expressions.

This section provides a general expression for the current/voltage characteristics of a one-dimensional *pin*-cell. The J/V characteristics presented here

do not require numerical solution. I also find expressions for the saturation current density and collection efficiency of *pin*-cells, establishing analogies to the expressions commonly used to describe *pn* solar cells.

5.2.1 Assumptions

There are five simplifications of the present model:

1. the diffusion lengths L and lifetimes τ are equal for electrons and holes,

2. the ratio JW/μ is low,

3. the electric field in the intrinsic layer is spatially constant,

4. the generation rate G is spatially constant throughout the i-layer, and

5. the i-layer has no doping.

Figure 5.6 shows the assumed band diagram. Under thermal equilibrium, the electron (minority carrier) concentration n_{p0} in the p-type layer, and the hole concentration p_{n0} in the n-type layer, are given by $p_{n0} = n_{p0} = n_i^2/N_d$, where n_i is the intrinsic concentration of the given semiconductor and N_d the doping density of the n- and p-layers (considered to be equal for both layers).
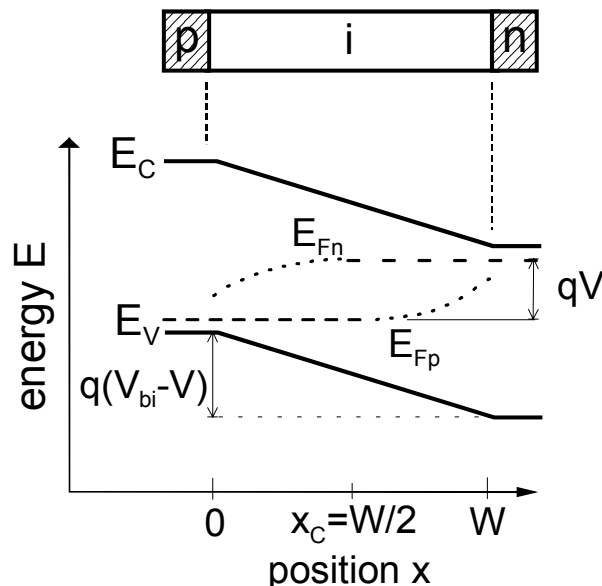

Figure 5.6: The *pin* diode with an intrinsic layer of thickness W under forward bias V. At the position x_C it holds $n = p$, assuming the same effective density of states for electrons and holes. The applied voltage V reduces the energy difference between the n and p layers by an amount qV, which is also the amount the quasi-Fermi levels for holes E_{Fp} and for electrons E_{Fn} get separated. The dashed lines indicate the quasi-Fermi levels which are assumed to be flat. The dotted lines symbolize the parts of E_{Fp} and E_{Fn}, which have to be calculated.

The built-in voltage V_{bi} is given by $V_{bi} = 2V_t \ln(N_d/n_i)$ [82]. This potential difference causes an electric field F in the intrinsic layer. I assume that no charges are present in the i-layer, implying that F is constant through the i-layer and vanishes in the doped layers. Thus, the electrostatic potential energy varies linearly through the i-layer and remains constant outside of it. The band diagram shown in Fig. 1 reflects these considerations. In thermal equilibrium, the internal electric field F has the value $F_0 = -V_{bi}/W$.

Together with the assumption of an uniform electrical field and equal values of the effective density of states at the valence- and conduction-band edges, the condition $n = p$ defines the coordinate x_C, resulting $x_C = W/2$. Figure 5.6 shows the position of x_C. Considering the Boltzmann equations for n and p, the product np at x_C is then $np = n^2 = n_i^2 exp(V/V_t)$, giving $p(x_C) = n(x_C) = n_i exp(V/2V_t)$ [83].

If a forward bias voltage V is applied to the junction, the resulting potential difference within the i-layer is $(V - V_{bi})$. Hence, the applied voltage V lowers the electric field, and the QFL splitting is given by the amount qV, as shown in Figure 5.6.

An important simplification I make, is that the quasi-Fermi level E_{Fn} of electrons is approximately flat as long as the electron concentration n exceeds the concentration p of holes. This means that E_{Fn} = constant for $n > p$ and, vice versa, E_{Fp} = constant if $p > n$. Following the arguments published by Sah, Noyce and Shockley [84], and Rhoderick and Williams [85], we find that the majority carrier QFL is nearly flat, *as long as* the ratio JW/μ is not too high: for example, if we have a *pin* diode with $W = 5$ μm, and the injection current that results at the point $V = 600$ mV, this requirement would imply $\mu > 0.1$ cm²/Vs.[8]

We are now able to derive the current/voltage characteristics. The current densities that will give us the current/voltage characteristics are, proportional to the slope of the quasi-Fermi levels [83]. Having this proportionality between currents and slopes of the QFLs in mind, we assume that the regions of space where their slope is negligible do not contribute to the cell's current (dashed lines in

---

[8] This value was obtained with numerical simulations performed with the program PC1D [88].

Figure 5.6). The current is then determined by the quasi-Fermi levels of minority carriers, where the slopes of E_{Fp} and E_{Fn} are different from zero. Figure 5.6 shows with *dotted lines* the part of E_{Fp} and E_{Fn} with non-zero slope, denoting that they are yet unknown. Calculating the quasi-Fermi levels is equivalent to calculate the carrier concentrations. For electrons as minority carriers, i.e. when $x < W/2$, the steady-state continuity equation for electrons can be written as

$$G - \frac{n(x) - n_0(x)}{\tau} + D\frac{d^2 n(x)}{dx^2} + \mu F \frac{dn(x)}{dx} = 0 \qquad (5.6)$$

where the recombination rate $R(x)$ has been replaced by $[n(x)-n_0(x)]/\tau$ (see Eq. (2.22)).

To obtain the total current, we need to solve also the majority carrier current, which is neglected in the present approach. To compensate for this error, the total current is approached as the sum of the two minority carrier currents at each side from the center of the cell. Thus, the assumption of equal diffusion lengths for electrons and holes, together with the homogeneous generation rate, enables to solve J for one carrier type and simply multiply the result by 2 to obtain the total current due to both carrier types. The comparisons between simulated and modeled J/V characteristics shown below, indicate that the total current predicted by the model has only a small error.

The two boundary conditions for the solution $n(x)$ have to be determined. The first boundary condition concerns the value of $n(x_C) = n_i exp(V/2V_t)$ that results from the assumption E_{Fn} = constant for $x \le x_C$. The second boundary condition states that an extra-current due to interface recombination is present at the p/i interface, at $x = 0$. With a surface recombination velocity S, the recombination current density at this interface is $qS(n(0)-n_{p0})$ (see Eq. (2.21)). The generation rate G is zero at this interface because its thickness is zero. In real cells, this surface recombination takes place at the contacts instead of the p/i- (and also i/n) interfaces as supposed here.

The solution of Eq. (5.6) for $n(x)$ is given by

$$n(x) = A + C_1 exp(\lambda_1 x / W) + C_2 exp(\lambda_2 x / W) \qquad (5.7)$$

which contains the constants A, C_1 and C_2, determined by the boundary conditions, and the dimensionless Eigenvalues λ_1 and λ_2

$$\lambda_{1,2} = -\frac{V - V_{bi}}{2V_t} \pm \sqrt{\left(\frac{W}{L}\right)^2 + \left(\frac{V - V_{bi}}{2V_t}\right)^2} \tag{5.8}$$

We see that the Eigenvalues λ_1 and λ_2 contain the diffusion length, the physical dimensions of the cell and the potential difference through the i-layer. As can be seen from Eq. (3), the Eigenvalue λ_1 is much larger than λ_2 at voltages smaller than V_{bi}. Thus, we can already expect that λ_1 dominates most of the current/voltage characteristics of the *pin* diode.

With *n(x)*, the recombination rate $[n(x)-n_0(x)]/\tau$ is determined. The integral of the generation-recombination rate from *x = 0* to *x = W/2* added to the current due to recombination at contacts $qS(n(0)-n_{p0})$, gives the total electron current, satisfying continuity. In Appendix B, I describe the mathematical procedures to obtain the solution of the electron concentration and use it to get the current/voltage characteristics. Next I present simplified expressions for the current density *J* that hold provided the parameter ranges given in Table 1 of Appendix B are not violated.

5.2.2 Current/voltage characteristics: dark case

For the voltage range $0 < V < V_{bi}$, the current density *J* is given by

$$J = \frac{2qn_iW}{\tau}\left[\frac{1}{\lambda_1} + \frac{S\tau/W}{1 + SW/D\lambda_1}\exp\left(-\frac{\lambda_1}{2}\right)\right]\exp\left(\frac{V}{2V_t}\right) \tag{5.9}$$

This expression is dominated by the eigenvalue λ_1, contained in an exponential term. It is not possible to define an unique diode ideality factor n_{id} (like in *pn*-cells) since it is not possible, in general, to separate *V* from λ_1. However, one can calculate the ideality factor from the slope of a semilogarithmic plot of the J(V) curve. Similarly to the double-diode equation in *pn* diodes given in chapter 3, these J(V) curves show that in general, n_{id} depends on voltage and diffusion length (see Figure 5.7). The ideality lies between 1.8 at low voltages, and 1.2 at high voltages. At small diffusion lengths, the value of n_{id} is 1.8, independent of *V*. The plots of Figure 5.7 use $S = 10^6$ cm/s, $W = 2$ μm, and $N_d = 10^{18}$ cm^{-3}.
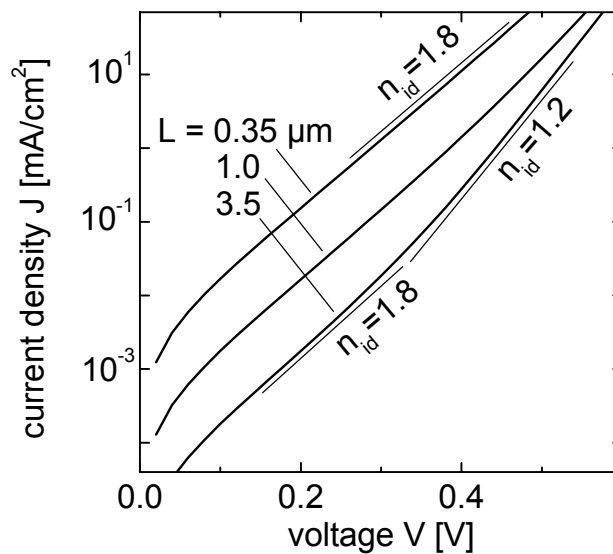
Figure 5.7: The dark current/voltage characteristics show different diode ideality factors n_{id} depending on voltage and diffusion length L. For high values of L and low voltages, n_{id} takes the value 1.8, which becomes 1.2 at high voltages. With small diffusion lengths, we have $n_{id} = 1.8$ independently of voltage. These plots assume $n_i = 10^{10}$ cm^{-3}, $S = 10^6$ cm/s, $W = 2$ μm, and $N_d = 10^{18}$ cm^{-3}.

If we have the case V ≈ 0, the current density shows two components: a positive and a negative one. It makes sense to attribute the negative term to the saturation current density J_0. In its most simplified version, which considers cells thicker than about 500 nm for the case of silicon, and a built-in voltage greater than 0.7 V, J_0 becomes

$$J_0 = \frac{2qn_iV_t}{\tau F_0}.$$ (5.10)

This equation says that the value of J_0 is inversely proportional to the electric field F_0 in equilibrium, evidencing the dominance on transport of the electric field at low forward biases. Interestingly, the saturation current density from the space charge region in a *pn* diode given by Eq. (3.32) shows an analogous expression to Eq. (5.10). This analogy reflects the drift origin of both currents, found in the *pin-* as well as in the SCR of the *pn* diode.

5.2.3 Current/voltage characteristics: under illumination

The full expression of J(V) in this case is given by Eq. (B.12), and a simplified version is Eq. (B.13). In this section I give a simple expression for the short-circuit current density J_{SC} of the cell and relate V_{OC} to J_0 and J_{SC}. The short-circuit current density J_{SC} reduces to

$$J_{SC} = qGW \frac{\exp(\lambda_2/2) - 1}{\lambda_2/2} , \qquad (5.11)$$

where the eigenvalue λ_2 must be evaluated using $V = 0$, according to short-circuit conditions. The short-circuit current depends on both, the absorption coefficient of the material and the light trapping of the cell (contained in G); and the electronic quantities L and F_0, found in λ_2. When L tends to zero, no photocurrent can be extracted. When L tends to infinity, the current reaches a maximum value J_{max}. The value J_{max} is qGW, being GW the total amount of carriers the light generated in the i-layer. Equation (5.11) is consistent with this physical observation, since λ_2 tends to zero when L tends to infinity. Since L has finite values in practice, J_{SC} reaches only a fraction of J_{max}. This observation enables us to define the quotient containing λ_2 in Eq. (5.11) as the collection efficiency f_C, given by

$$f_C = \frac{\exp(\lambda_2/2) - 1}{\lambda_2/2} \qquad (5.12)$$

To get more insight into the collection efficiency, Figure 5.8 shows plots of f_C as a function of L/W. As seen from this plots, f_C depends on the values of the built in potential V_{bi}. This feature accounts for a bias dependent collection of the *pin*-cell, a feature that is not present in *pn*-cells, because the collection is based on diffusion in *pn*-cells.
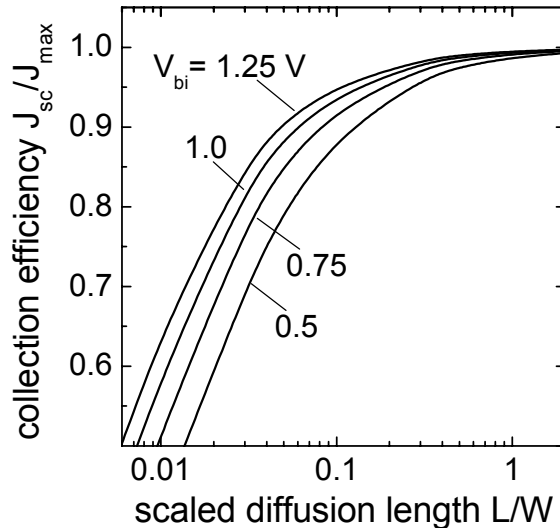

Figure 5.8: The collection efficiency depends strongly on the scaled diffusion length, given by L/W. With these different values of V_{bi} we observe the bias-dependent collection efficiency of the *pin*-cell. (The values of V_{bi} indicated are obtained assuming a thermal voltage $V_t = 25$ mV).

From Figure 5.8 we can also say, for example, that values of J_{SC} greater than 90 % of J_{max} are maintained if $L/W > 0.1$, avoiding greater losses in cell efficiency. This finding reflects the fact that *pin* cells are successful in delivering photocurrents even in low-quality materials, since the requirement $L/W > 0.1$ is a rather loose restriction.

5.2.4 The $\mu\tau$-product

It is useful to continue the analysis of the light characteristics from another point of view, describing the influence of the product $\mu\tau$ on the output characteristics of the *pin*-cell. The $\mu\tau$ product is a commonly measured quantity using a variety of techniques, and it is considered as an important characterizing parameter in a-Si, and recently also in nanocrystalline Silicon thin film solar cells [87]. The relation of the $\mu\tau$ product to cell parameters such as J_{SC} and V_{OC} is direct since $L = \sqrt{D\tau}$, which can be expressed as $\sqrt{V_t\mu\tau}$ using Einstein's relation.

Within the present model, there is no closed-form expression for V_{OC}. Nevertheless, we can relate V_{OC} to parameters that depend on $\mu\tau$ (or L) such as J_{SC}, and on τ such as J_0. Similarly to the *pn*-cell, V_{OC} holds a proportionality to J_0 of the form $V_{OC} \propto V_t ln(J_{SC}/J_0)$. However, in contrast to the *pn*-cell, Figure 5.9 shows that this relationship is somewhat more case-dependent in the *pin*-cell. The strict proportionality $V_{OC} \propto V_t ln(J_{SC}/J_0)$ holds mainly at low values of W and V_{OC}. This observations allow us to say that J_0, directly correlates with the open circuit voltage of *pin* solar cells. The low values of J_0 required to obtain high V_{OC}'s can be reached with high values of the built-in field F_0. However, and in contrast to *pn*-cells, the improvement in V_{OC} can *only* be reached if the cell is thin, since, as seen from Figure 5.9, thick cells show a saturation of the V_{OC} curves, meaning that lowering J_0 does not improve V_{OC}.
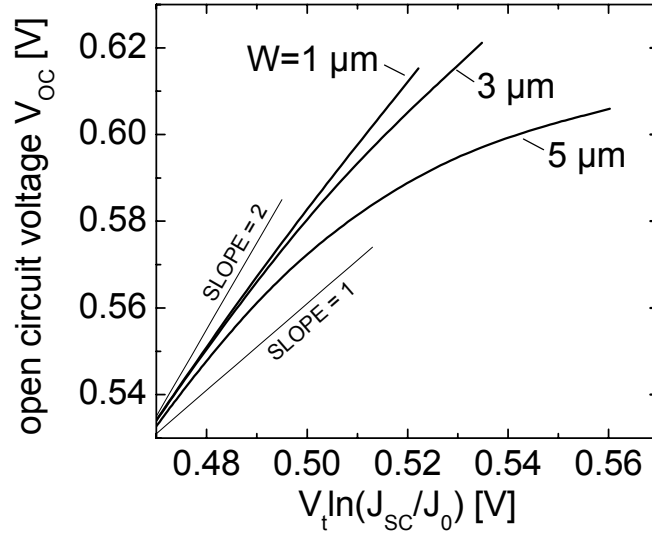
Figure 5.9: The relation between the quantity $V_t ln(J_{SC}/J_0)$ and V_{OC} shows that J_0, and thus τ (see text), is directly correlated with V_{OC}, similarly to a *pn*-cell. However, if the thickness W of the cell increases, this proportionality vanishes.

5.2.5 Comparison with experiments

I measured dark current/voltage characteristics on *pin*-cells of µc-Si prepared at Kaneka Corporation at different temperatures and fitted them with Eq. (5.9). The cells were prepared by deposition of microcrystalline silicon on glass substrates with the CVD method, as described in Ref. [8]. Figure 5.10 shows that the model (solid lines) fits the data (symbols) very well, and using realistic parameters (see below).

To minimize the number of fit-parameters to put in the *J(V)* equation, I measured some of the quantities of Eq. (5.9). The thickness W, measured with a surface profiler, is W = 1.3 µm, and the doping of the p- and n-layers using voltage/capacitance profiling[9] at different frequencies and temperatures is $N_d \approx$ 3.2×10^{16} cm^{-3}. This low value can be attributed to the carrier density at the p/i and i/n interfaces rather than at the highest doping levels deep in the p- and n-layers. Indeed, fits of the *J(V)* characteristics that use higher doping densities became worse.

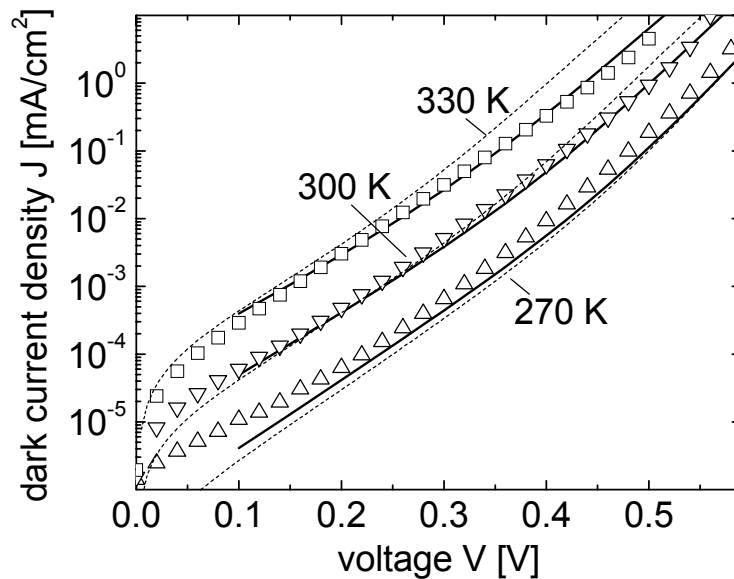[9] The voltage/capacitance method is described on page 41 in Ref. [14].

Figure 5.10: Plot of the measured dark current/voltage characteristics of microcrystalline silicon *pin* diodes prepared with the CVD method [8]. The current/voltage curves, measured at different temperatures (symbols), are fitted by Eq. (5) (solid lines). The dotted lines are PC1D simulations performed using exactly the same parameters as our fits and 70 nm thick p- and n-layers, showing a good agreement with the results obtained with our model.

With the values of W, N_d and n_i, only three parameters are necessary to fit the current/voltage curves: the recombination velocity S, the carrier lifetime τ and the diffusion constant D. All the fits in Figure 5.10 use $S = 10^5$ cm/s, $\tau = 0.6$ μs and $D = 5$ cm^2/s (i.e. a diffusion length $L \approx 17$ μm). The carrier lifetime of 0.6 μs, implies a high material quality, and high V_{OC}. The high L/W ratio ensures a high J_{SC}, analogously to the *pn*-theory of chapter 3. This explains the high efficiencies of up to $\eta = 10$ % reached by the *pin* cells prepared at Kaneka [11].

In order to crosscheck the results of the fits, I simulate the current/voltage characteristics using the numerical simulator PC1D [88] using the same parameters as the fits. Despite the differences between the simple model presented here and the simulations, we find the good agreement shown in Figure 5.10 with dotted lines. The PC1D simulations use a p- and n-layer with a thickness of 70 nm, and consider SRH recombination at the intrinsic Fermi-level energy, with a lifetime of 0.6 μs. Observing the simulation results, I corroborated that the majority quasi-Fermi levels remained flat, enabling a comparison between the J/V curves of the present model and the simulations.

Turning to the light characteristics, I investigate the dependence of cell output parameters under illumination on the μτ product. The symbols in Figure 5.11 stem from a recent experimental work that shows how the efficiency of nanocrystalline silicon *pin* solar cells increases with μτ [89]. The solid lines in Figure 5.11, calculated with the model, explain the experimental data satisfactorily.

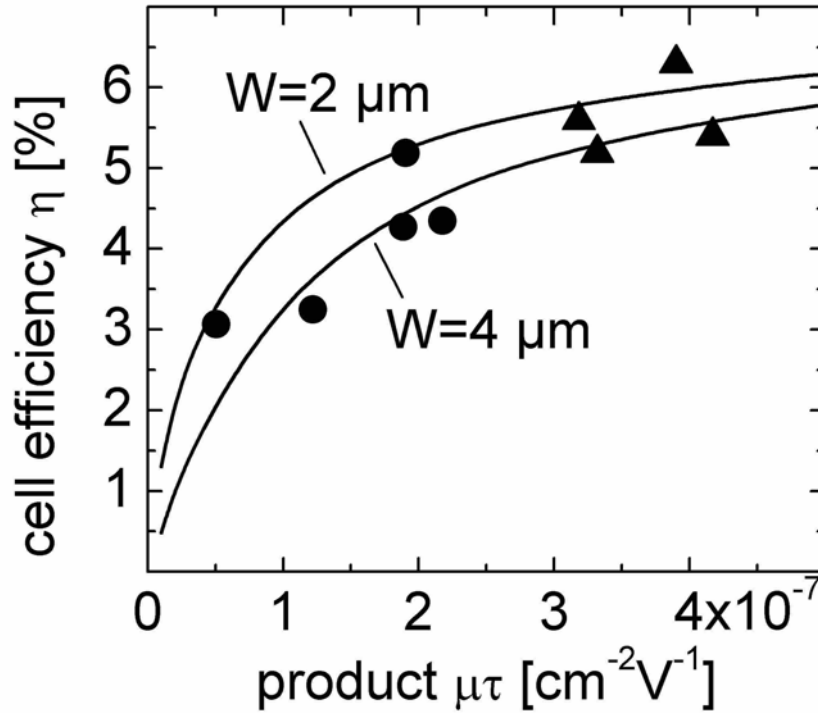Figure 5.11: The measurements of cell efficiency η of *pin*-cells of fine-grained silicon correlated to the μτ product (symbols) agree well with the analytical model (solid lines). These curves use $N_d = 10^{18}$ cm^{-3}, $D = 10$ cm^2/s, $S = 10^6$ cm/s and two different thickness W as parameters. The circles are experimental values of cells with $W = 3.5$ μm and the triangles stem from cells with W between $W = 2$ and $W = 2.5$ μm.

The evaluation of the current/voltage characteristics involved in Figure 5.11 use $N_d = 10^{18}$ cm^{-3}, $D = 10$ cm^2/s, $S = 10^6$ cm/s, and values of the homogeneously assumed generation rate G that account for about the same short-circuit current that have the cells of the experimental data. Two different values of the thickness W are assumed, $W = 2$ and 4 μm. The calculation procedure consists in varying the lifetime τ, and calculate at each value of τ the J/V characteristics, obtaining η. The μτ-product in each case, is calculated with the equation $μτ = V_t D τ$.

5.3 Conclusions

The numerical model explains that the high efficiency η reached by the microcrystalline silicon *pin*-cells can be reached *only* with low defect densities, in agreement with the conclusions extracted from the simple model presented in chapter 3: at small grain sizes, only a low grain boundary recombination activity permits good efficiencies. It also solves the question about the convenience of using a doped i-layer: at low doping densities, a moderate efficiency up to 10 % is ensured. Higher efficiencies η up to η = 15 % and open circuit voltages V_{OC} = 0.75 V can *only* be achieved with low recombination contacts and doping levels of up to 10^{18} cm^{-3}. These results agree with the predictions of the model for V_{OC} as a function of the doping level chapter 4, which considers one dimensional, isolated grains. We should be aware of the fact that the geometry in Figure 5.1 assumes a grain boundary plane that is *perpendicular* to the surface of the solar cell. Only with a material that shows such grain boundaries could one achieve the values predicted. Nevertheless, the assumption of the perpendicular grain boundary goes hand-in-hand with the columnar grain structures achieved with modern preparation techniques. A possible reason for the absence of experimental data showing high efficiencies in thin, highly doped cells, could be that the low contact recombination velocities require special treatments of the contact/semiconductor interfaces, adding more steps to the solar cell processing.

The analytical model of the *pin*-cell, which gives a closed-form of the whole current/voltage characteristics for the first time, shows to be a proper tool to understand the behavior of *pin*-cells. It shows that many trends observed in *pn* junctions, such as the increase of V_{OC} with the saturation current densitiy, or the dependence of J_{SC} on the ratio L/W, are also present in the *pin*-cell. This unifies the understanding of the operation of a solar cell, regardless of pin or *pn*-type structure. The final part of this chapter, uses the J/V equation to fit dark- as well as light-measurements of *pin* solar cells J/V characteristics. The model explains with realistic parameters the increase of cell efficiency with $\mu\tau$-product found experimentally by other research groups.

6 Laser-crystallized silicon

Among the techniques to prepare thin-film silicon without using wafers, the crystallization is a widely spread technique. Crystallization is an indirect way to obtain polycrystalline silicon from amorphous (a-Si)- or nanocrystalline (nc-Si) layers, deposited for example onto glass by chemical vapor deposition. A simple crystallization approach is the solid-phase crystallization, which consists in annealing the films at temperatures well below the melting point for many hours, obtaining a polycrystalline film [90]. Other techniques use heating lamps to reach the melting point of the amorphous silicon, which implies the use of heat-resistant substrates [44]. Laser-crystallization makes use of laser-light pulses to melt the silicon locally, inducing crystallization. In general, the resulting films show high electronic quality, with excellent homogeneity over large areas, and even using ordinary glass substrates. An early work that demonstrated that this technique delivers high-quality films was published by Shah, Hollingsworth and Crosthwait in 1982, showing that microresistors made with this technique had better quality and uniformity over large areas than some polysilicon films prepared with the low-pressure chemical vapor deposition method [91]. From that time, laser crystallized silicon (lc-Si) is used by the electronic industry to obtain thin-film transistors (TFTs) for flat-panel displays. At present, the large progress in microelectronics demands even better electronic quality, which could also be reached by lc-Si films. Recently, TFTs with remarkably high channel mobilities of up to 510 cm^2/Vs were reported [92].

The electronic quality of lc-Si has always been estimated by the channel mobility in TFTs, which depends not only on the material properties but also on other factors such as the dimensions of the channel. Despite its importance for microelectronics, there is almost no knowledge about the fundamental transport and recombination parameters of the *material*, such as the minority carrier lifetime and bulk mobility. Knowing the minority carrier lifetime would enable us to determine if minority carrier devices such as bipolar transistors, diodes and photodiodes can be prepared using lc-Si. Therefore, the question addressed in this

chapter is if lc-Si is also suitable for *minority carrier* devices, and it will be answered in this chapter by means of photoelectrical characterizations.

Laser-crystallization of silicon is normally performed on transparent insulating substrates, which offer the following advantages: they are suited to the flat-panel display technology, they are bad heat conductors (avoiding losses of thermal energy), and they do not absorb the laser light we want to drive into the semiconducting layer. However, from the point of view of making an electron device, it could desirable to have conducting layers between the substrate and the crystallized film, which can serve as contacts. Here, I address the question if it is possible to realize such a crystallization, showing that one can obtain laser-crystallized silicon on conducting layers as well. I prepared bare lc-Si films on conducting layers, as well as test diodes.

6.1 Preparation

6.1.1 Heating a semiconducting layer with laser pulses

Heating of an amorphous silicon (a-Si) layer to its melting point of about 1100 K is reached by irradiating the sample with visible light. The goal is to generate phonons (i.e. lattice vibration quanta), since, the higher the phonon energy, the higher the lattice temperature. How can one generate phonons using light? The laser light excites electrons to high energy values above the conduction band edge, which gain kinetic energy. The electrons dissipate that kinetic energy by interacting with the atoms of the lattice, relaxing to the edge of the conduction band. That interaction of electrons with atoms implies the emission of phonons. The processes associated to light absorption and phonon generation that arise upon light excitation are shown in Figure 6.1. The photon energy $h\nu$ of the light is chosen to be well above the band gap of Si. The leftmost process shown is the band-to-band absorption, where light is absorbed by bound electrons (in the valence band), generating electron-hole pairs. Since the electron energy *after* the absorption process is higher than the equilibrium energy in the conduction band (nearly the energy of the band edge at room temperature), the electrons will seek equilibrium and fall to the edge of the conduction band. In that relaxation process, they emit

some phonons, heating the lattice. The free electrons in the conduction band also absorb light, as shown in Figure 6.1. They end up with high (kinetic) energies, producing electron-electron scattering that will make them loose energy, relaxing to lower energies. The relaxed electrons build up an electron plasma at some energy value. Following Figure 6.1, the electrons of this plasma can either recombine with holes or relax to the band edge, which is the main phonon source in the whole heating process. The recombination with holes takes place *via* different processes. Only one of these contributes to phonon emission, namely the Auger recombination. In the Auger recombination mechanism, an electron gains the energy freed in a recombination process, as shown in Figure 6.1. After excitation, the excited electrons emit phonons.
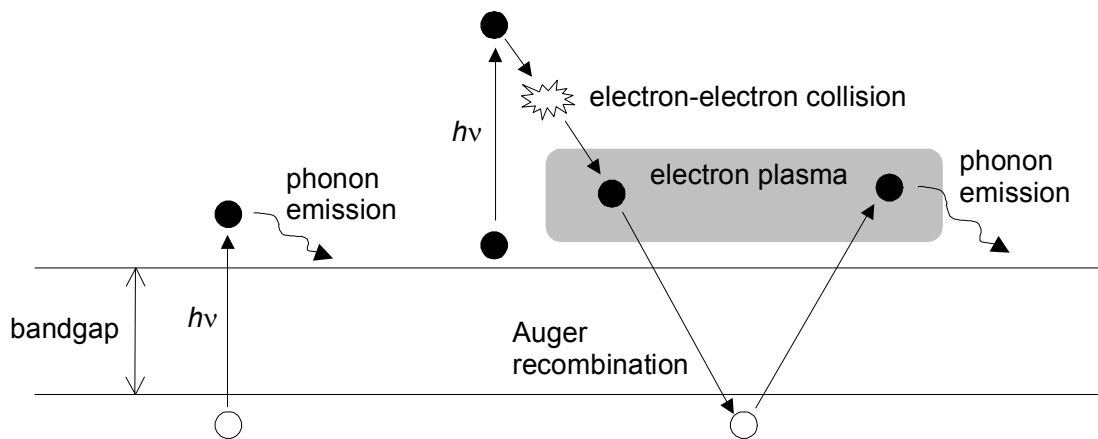

Figure 6.1: This band diagram shows the processes that occur when a semiconductor is heated with light, having an energy $h\nu$ greater than the band gap E_g. The leftmost process shown is the band-to-band absorption. The excited electron emits some phonons (with a relatively small lattice heating) when it relaxes to the conduction band edge. Secondly, we have an electron in the conduction band absorbing a photon, which gains kinetic energy and collides with other electrons, relaxing to an electron plasma at lower energies. From the plasma, it either recombines through an Auger process, freeing a valence band electron that emits phonons later, or it directly emits phonons when relaxing to the conduction band. Both processes increase the lattice temperature since phonon emission is present.

The Auger processes, as well as the phonon emission cascades, have lifetimes of about 1 ps, much faster than the 10 to 500 ns long laser pulse. Therefore, if the light power is sufficient, these fast-heating processes will melt the material during a single laser pulse [93].

Once the material is melted and the laser pulse vanishes, a large amount of heat is transferred by conduction from the melted film to the substrate, which did not get heated by the pulse (either because it does not absorb the laser light or

because it is much thicker than the film). When the temperature of the liquid Si is lower than its melting point, nucleation seeds appear. These seeds are the only starting point for the crystallization, since the amorphous substrate (glass, for example) does not offer crystallization seeds.

6.1.2 Sequential lateral solidification process

Several different techniques are utilized to crystallize materials over large areas using laser beams. Most of them crystallize only a portion of the film, and then displace either the beam or the substrate to crystallize the contiguous areas. In the frame of the present work, the *sequential lateral solidification* (SLS) process has been adopted (See for example Refs. [92] and [94]). The idea behind this process is to generate grains that serve as seeds for further crystallizations applied spatially and temporarily displaced from the previous crystallization event. Figure 6.2 sketches a layer being crystallized with the SLS-process. Part (a) shows a view on the crystallized film after a single pulse. With the laser used in this work, the crystallized area is 5 μm wide and 150 μm long ellipse, corresponding to the area of the laser beam focused onto the substrate. As explained by Dassow in Ref. [94], the marginal sector of the ellipse shows small grains, which are the ones that crystallize first because this area is the most undercooled. They serve as seeds for the large grains at the SLS-region indicated in the figure. The large grains grow only for sufficiently high light powers. In the center, we obtain small grains because it is the less undercooled region.
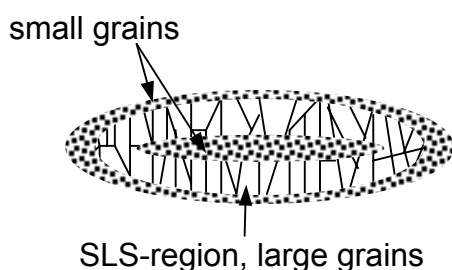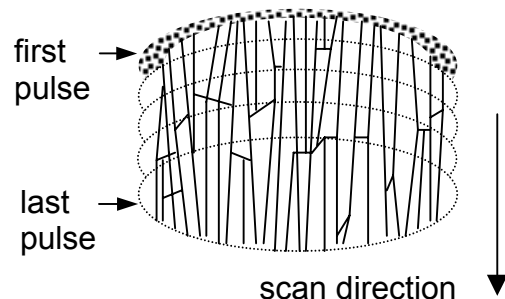
Figure 6.2: (a) shows the result of a single pulse crystallization, where small grains at the border crystallize first and serve as seed for the larger grains. The center of the crystallized area shows also small grains because it is the less undercooled part of the pulse. (b) shows a scan after five laser pulses that were displaced in the scanning direction, using the large grains of each earlier crystallized region as seeds for the new forming crystallites.

Figure 6.2(b) shows the same film after applying five laser pulses shifted slightly between each other. The shift between every pulse is carefully chosen, in order to achieve that every melted area comes in touch with the region of large grains generated by the previous pulse, using those grains as growth seeds. Thus, the large grains continue growing downwards the scan direction. This process of displacing the pulses properly is the actual Sequential Lateral Solidification. The Nd:YVO$_4$ laser utilized in the present work yields elongated grains that are 1x(10…100) μm^2 in size.[10] After the sample is scanned in the vertical direction, the substrate is displaced laterally and a new scan begins, thus covering all the area of the sample.

Dassow observed that when crystallizing with the SLS-process, the grain width depends directly on the a-Si thickness, the laser power and the pulse frequency [94]. Nerding et al. [95], explained this behavior by observing that the smaller the film thickness, the laser power or the pulse frequency, the higher the quenching rate is. A high quenching rate means fast crystallization and small grains. From the technological point of view, such high quenching rates means that one is able to tailor the grain width, which is an important feature for research purposes. In this chapter, for example, I investigate the dependence of the electrical conductivity with grain size, which provides information on the physical transport parameters of the grain boundaries in lc-Si.

The crystallization on insulators has the benefit of using glass substrates that isolate thermally the film during the crystallization, and permit also its use in the flat-panel display technology. The next section investigates the crystallization of silicon on conducting substrates, which is aimed at the preparation of *vertical* microelectronic devices, such as diodes or solar cells.

6.1.3 Crystallization of silicon on conducting layers

Intuitively, we note that in order to drive all the available heat into the a-Si, the underlying layers should be rather isolating, not conducting. In order to make the crystallization on conductors possible, we need to fulfill two conditions:

---

[10] The crystallization parameters are discussed below.

 i. the heat loss from the melt to the substrate must be sufficiently low, permitting the lowest possible quenching rates.

 ii. the conducting film must preserve its electric properties after crystallization.

These conditions are attained by selecting the right thickness and choosing an adequate conductor. We select the conductor by comparing several metals with regard to the following aspects:

1. Melting point. The melting point of the conductor must be higher than the melting point of silicon at 1685 K [93].

2. Thermal conductivity. Low thermal conductivity is desired, to ensure that the heat transfer from the melt to the substrate is minimal.

3. Thermal expansion coefficient. For an operating device that combines layers of different materials, the conductor must expand similarly to the substrate (glass) and to silicon. If they expand differently, the films will experience interface stresses that will generate structural damages (cracks). This criterion limits the selection to a few conductors.

4. Solubility in silicon. Most metals dissolved in Si are unwanted impurities. They produce energy levels in the band gap that harm the electrical properties of Si. The lower the solubility of metals in silicon, the higher will remain the purity of the lc-Si.

Table 6.1 lists the melting point, thermal conductivity, and thermal expansion coefficient of some metals and Si. The thermal expansion coefficient is given at room temperature. The most compatible to Si are vanadium and chromium. Due to its good adhesion to glass, chromium is a standard masking material in electronics. Molybdenum shows a much higher thermal conductivity than Cr and V. Chromium was selected because its solubility in silicon is much lower than that of many metals [96] (However, due to grain boundary diffusion, the solubility of metals in fine-grained silicon should be higher than the c-Si values indicated there).

A final aspect to consider is the formation of silicides. Most silicides are semiconducting, and appear at semiconductor/metal contacts, affecting the electronic transport through those interfaces [98]. When using chromium, the most

common silicide formed is $CrSi_2$. In our case, it should not be expected that $CrSi_2$ appears during the laser crystallization, since the time given is too short (about 50 ns). Instead, silicides will form before crystallization, after the deposition of a-Si, when tempering the a-Si layers on Cr to extract hydrogen (which causes 'microexplosions' during crystallization in air). Tempering was performed at about 400°C for some hours, a temperature and time that permit some formation of $CrSi_2$ [99]. With the formation of $CrSi_2$, the Cr thickness will decrease. The chromium thickness (measured with a surface profiler) decreases after tempering. The experiments performed in this work indicated that about 10 nm of chromium get consumed by tempering. After experimental observations on formation of thin-film $CrSi_2$, the silicide formed should then be about 30 nm thick (see page 94 in Ref. [99]).

Table 6.1 Thermal properties of silicon and selected candidate metals to serve as base layers for crystallization. The metals presented have a higher melting point than silicon, an expansion coefficient compatible with Si, and low thermal conductivities. Molybdenum was discarded because of its high thermal conductivity (compared to vanadium and chromium), and its too low expansion coefficient with compared to silicon.

	melting point [K]	expansion coefficient[1] $[10^{-6}\ K^{-1}]$	thermal conductivity[2] $[Wm^{-1}K^{-1}]$
silicon	1685	7.6	430
molybdenum	2888	5.1	87.7
vanadium	2175	8.3	29.5
chromium	2133	6.5	45.5

[1] valid for the range 273-373 K.
[2] values extrapolated to the melting point of silicon, from Ref. [97].

Among the non-metallic conductors, I also prepared some lc-Si samples on ZnO, a standard conducting material to make transparent contacts on solar cells. The thicknesses of ZnO can be larger than any metal's thickness because it has a lower thermal conductivity than them [100].

6.1.4 Experimental crystallization setup

Figure 6.3 shows the crystallization equipment used in this work [94]. The substrate is held by an x-y table. A cylindrical and a spherical lens focus the laser beam onto the substrate, making the beam's cross-section elliptic. A stepping motor that uses the signal provided by an auto-focus control system moves the spherical

lens, keeping the focus if the table eventually vibrates. Using the x-y table, the scanning is performed by displacing vertically the substrate for every scan. After a vertical scan, it is displaced horizontally, thus covering all the area to be crystallized.
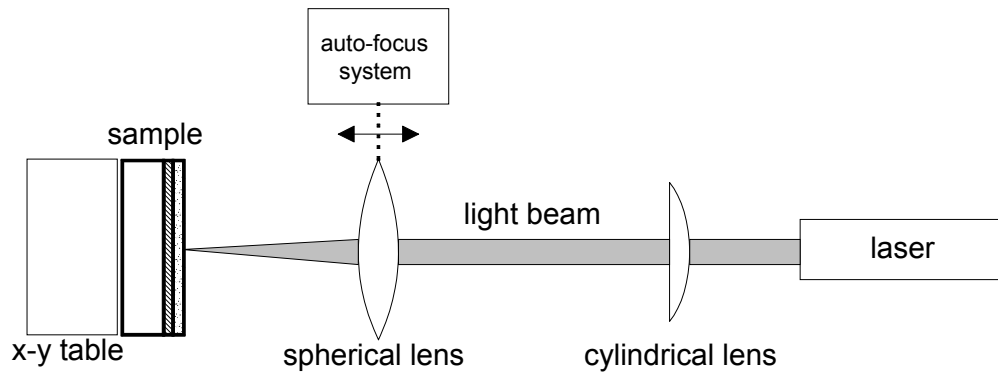

Figure 6.3: Experimental arrangement utilized in this work for laser crystallization using an Nd:YVO$_4$ laser. The sample is put onto an x-y table that moves it to make the scans. The auto-focusing system keeps the focus by moving the spherical lens.

The power laser used is a commercial Nd:YVO$_4$ laser, which works at up to 100 KHz, and delivers 750 mW light power (at 20 KHz). Dassow showed that compared to an excimer laser, which works at higher powers but lower frequencies, the Nd:YVO$_4$ laser yields much higher crystallization rates, making it particularly attractive for large area applications needed in electronics technology [94]. The Nd:YVO$_4$ laser has a wavelength of 1064 nm, which is divided by two using a frequency doubler, resulting in 532 nm wavelength. The cross section of the laser beam used is about 5 µm wide, and the SLS-region is about 1 µm wide. The vertical displacement Δx between two pulses is set to 0.5 µm to ensure overlapping of the melt with the SLS-region of the previous pulse. For a pulse frequency f = 20 KHz and Δx = 0.5 µm, the required vertical scan velocity becomes 10 mm/s. This set of parameters is taken in the present work (if not indicated otherwise).

Two types of films were crystallized: a-Si on SiN or glass, and a-Si on chromium and ZnO. The substrate was always Corning glass. Figure 6.4 shows both types of films and typical values of their thicknesses. The SiN layer is utilized as diffusion barrier, to avoid diffusion of impurities from the glass to the substrate during the melting process.

(a)   (b)

a-Si (~200 nm)

SiN (~200 nm)   Cr (~50 nm)
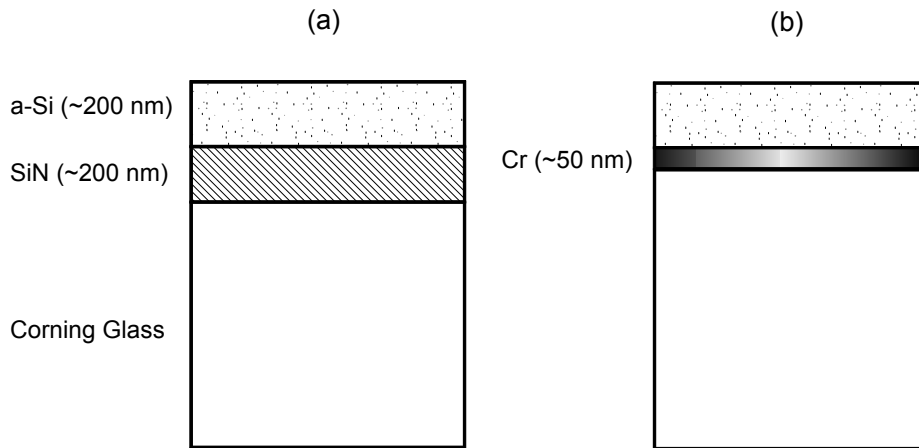
Corning Glass

Figure 6.4: Part (a) shows a sample with a SiN buffer layer (or directly on glass) and part (b) uses a chromium layer. The substrate is always Corning glass. Typical values of the layer thicknesses are given.

6.2 Structural characterization

This section briefly describes the structure of the crystallized layers, focusing on homogeneity (or uniformity). The uniformity is investigated by means of grain sizes and widths, and the statistical distribution of grain widths. For a description of other structural properties, such as texture, and grain boundary types, I would like to refer to the thesis of Dassow [94].

Results of laser crystallization of silicon on conducting layers are also shown here, with special focus on chromium-based layers. As we will see, the grain sizes obtained using Cr are similar to the obtained with crystallizations on insulators, and the films on Cr show better uniformity.

6.2.1 Grain sizes and shapes

In order to permit a measurement of the grain sizes, we first need to make the grain boundaries visible. Secco etching is a method specifically designed to reveal defects in silicon, making grain boundaries visible under the microscope. Figure 6.5 shows a picture taken with an optical microscope after etching a lc-Si film. This 300 nm thick film uses a SiN buffer layer and is crystallized at 20 KHz, 750 mW laser power and a shift of 0.5 μm between pulses. The dark, vertical lines, are the grain boundaries made visible after etching. The width of the grains is about 1 μm, while the length is several 10 μm. Figure 6.5 shows the grain widths to

be similar in the pictured area. This uniformity in grain width over large sample areas is a key advantage offered by SLS-grown layers.
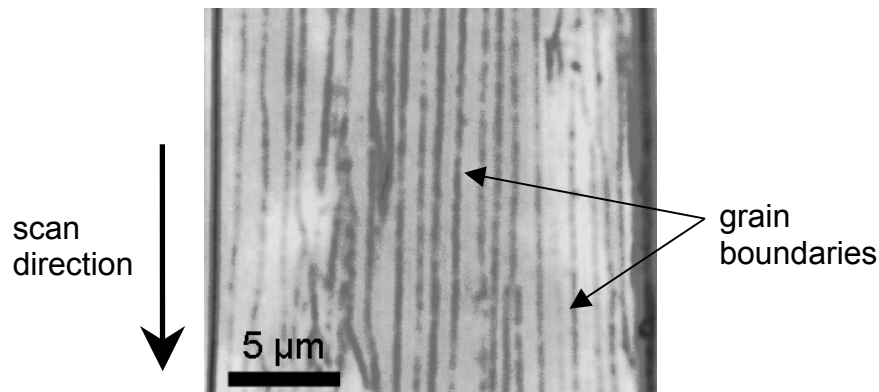

Figure 6.5: This optical microscopy image of a Secco-etched film shows long, elongated grains obtained with laser crystallization of a-Si. The grain boundaries are represented by the darker lines. Typically, the grains are about 1 μm wide and several 10 μm long.

A closer look at the films enables Transmission Electron Microscopy (TEM). Figure 6.6 shows a TEM[11] image of a lc-Si film (with SiN layer), where we can identify grain boundaries, and an intersection where a new grain is born. The dark, curved lines are produced by the local mechanical stresses of the film. They arise spontaneously in the sample preparation process required for TEM microscopy. Point defects are not observed, which means that the defect density in the grains must be very low.
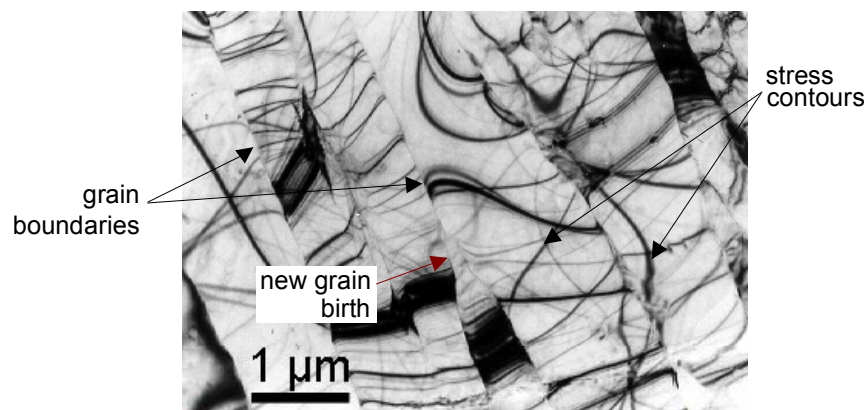

Figure 6.6: This TEM image of a laser-crystallized film shows the actual shape of the grains, the grain boundaries. We also identify an intersection of three grain boundaries where a new grain is born. The dark curves are stress contours originated from sample preparation.

---

[11] The TEM analysis presented here was performed by Melanie Nerding, from the *Lehrstuhl für Mikrocharakterisierung* at the Erlangen University. I would like to gratefully thank her for our succesful cooperation and fruitful discussions.

Figure 6.7 shows TEM images of lc-Si films crystallized on conducting layers. Part (a) belongs to a film crystallized on a 30 nm thick chrome layer on glass, while the film depicted in part (b) uses a 200 nm thick ZnO layer on glass.[12] We see that the shape and size of the grains is not altered with respect to the layer crystallized on a SiN buffer layer. Why do the grains grown on such different substrates look similar? Concerning the crystallization process, the growth is independent of the substrate chosen because it is *lateral* and based on the presence of crystallites of the previous scan, not relying on seeds from the substrate.

(a) with chromium layer   (b) with ZnO layer
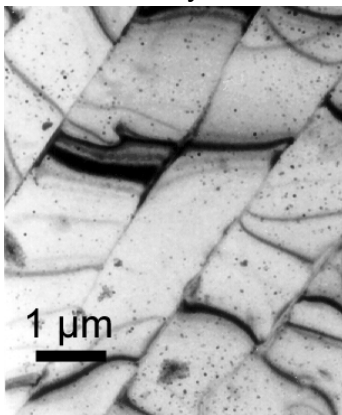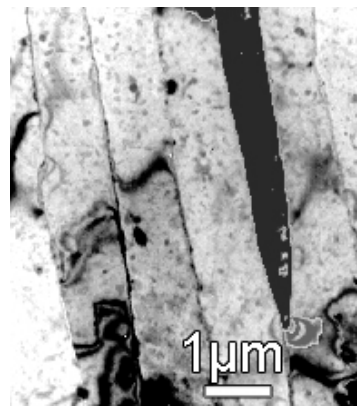

Figure 6.7: Transmission electron microscopy images of laser crystallized silicon on different conducting substrates, where film (a) has a 30 nm thick chromium layer, and film (b) uses a 200 nm thick ZnO film. Both crystallizations lead to grain sizes and shapes very similar to crystallized silicon on SiN.

The crystallized films show preferential textures, which can be obtained from analysis of Electron Back-Scattering diffraction patterns. For films crystallized directly on glass, the texturing depends on film thickness [101]. However, films with a SiN layer show textures that are independent of film thickness, and the surface normal coincides with the crystallographic <111> direction, while the scanning direction coincides with the <110> direction. The same orientations are observed in layers crystallized on chromium.[13]

---

[12] The Zinc-Oxide was deposited by Kay Orgassa using a radio frequency sputtering system. I would like to thank him for his cooperation.

[13] M. Nerding, personal communication.

6.2.2 Grain size distributions

The measurement of the width g of the grains over a large crystallized area, allows for a statistical analysis of grain sizes. Firstly, this statistics is necessary to obtain a median grain width g_{med}, which characterizes the crystallized film structurally. Secondly, the relative width σ_g of the grain width distribution is extracted, which gives us information about the uniformity and homogeneity of the films: the narrower the grain width distribution (small σ_g), the more homogeneous is g over the sample. In polycrystalline silicon, the grain width population $f(g)$ follows a log-normal distribution, which is obtained regardless of the preparation method [102]. This distribution results from random nucleation produced on amorphous substrates. The log-normal distribution for the grain widths is given by

$$f(g) = \frac{1}{\sqrt{2\pi} g \sigma_g} \exp\left(-\frac{1}{2}\left(\frac{\ln(g/g_{med})}{\sigma_g}\right)^2\right), \qquad (6.13)$$

where g_{med} is the median of the distribution. The statistical analyses given in this section are based on 150 to 300 grains measured for each sample. The measurements were performed on pictures of Secco etched samples, which yield the same values as TEM pictures.[14] Figure 6.8, part (a), shows a grain width population from a 150 nm thick film with SiN buffer layer, and its corresponding log-normal fit. The film has a g_{med} = 0.9 µm and σ_g = 0.5. If we crystallize silicon on a thin chromium layer, we get g_{med} = 1.21 µm and σ_g = 0.46 (see part (b) of Figure 6.8), showing us again that the nucleation process does not depend on the substrate, as a consequence of the SLS-growth.

---

[14] After a comparison with statistical data obtained from TEM images, of the same samples.
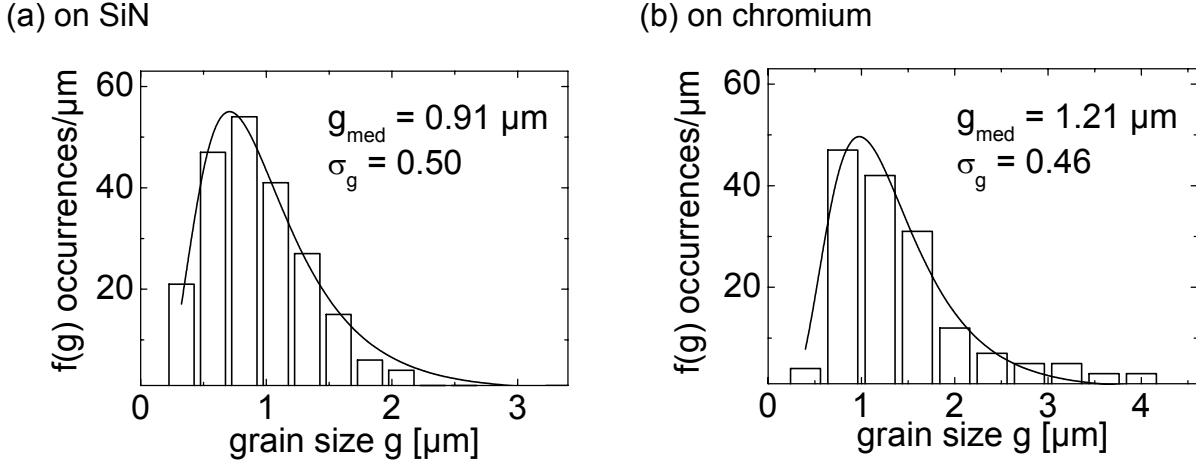
(a) on SiN   (b) on chromium

Figure 6.8: Grain size populations *f(g)* observed in laser-crystallized Si films follow a log-normal distribution (solid line). Part (a) corresponds to a lc-Si film on a SiN substrate, while part (b) uses a chromium layer. The similarity of the distributions relies on the SLS-growth of both layers, which is independent of the substrate.

Using the possibility to vary the grain size, I made samples with different grain sizes and analyzed them fitting the distributions with the log-normal function. The experiments show that a correlation between σ_g and g_{med} is obtained. Figure 6.9 shows that there is an increase of σ_g with g_{med}, and that this increase is valid regardless of the type of substrate (i.e. chromium, glass or SiN). The different grain sizes were obtained either by increasing the laser power, the film thickness, or the pulse frequency. The fact that large σ_g are linked to large values of g_{med}, means that when preparing large-grained films, one must pay the price of a lower grain width homogeneity. To quantify the relation between grain size and homogeneity, I define a *quality factor Q* as

$$Q = \frac{g_{med}}{\sigma_g},$$ (6.14)

which gives credit to films that have large grains *and* small grain width variations. This factor has a profound significance not only from the structural point of view, but also from the electronic point of view: the higher the structural homogeneity is, the higher is the homogeneity of the electronic properties.

In the g_{med} *vs.* σ_g plot, the value of Q is given by the slope. The best lc-Si films with SiN buffer or on glass I obtained, have a quality factor of about $Q = 1.8$ µm, while the films on chromium show $Q = 2.6$ µm. What is the explanation for the more uniform grain widths in Cr-films, knowing that the growth mechanism is not

affected by the type of substrate? I suspect that this property could be related to the higher thermal conductivity of chromium with respect to the insulators. On chromium, heat is conducted better and the silicon melt must have a more homogeneous temperature profile. When cooling down, the homogeneously heated film leads to more homogeneous conditions for crystallite growth, and therefore we obtain the lower values of σ_g found.
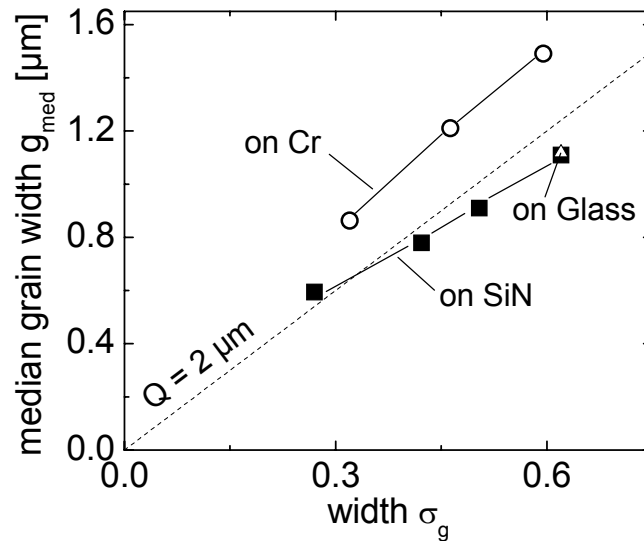

Figure 6.9: This data show that there is a correlation between g_{med} and σ_g. The black squares are data of lc-Si films with SiN buffers, the triangle is crystallized directly on glass, and the open circles belong to lc-Si on Cr. Surprisingly, lc-Si films on Cr show higher values of g_{med} at the same σ_g than films with SiN buffer or crystallized directly on glass! Therefore, we can say that films on chromium have higher structural (and therefore electronic) homogeneity.

6.3 Optical characterisations

6.3.1 Absorption coefficient and band gap

This section describes the measurement of reflectance and transmittance, which allows the determination of the film thickness and the absorption coefficient of the films. In the next section, these quantities are needed to make a quantitative analysis of the photoelectric characterizations.

The measurement of the film thickness is carried out only by optical means, because the lc-Si films are very thin. A white-light spectrophotometer is used to measure the film reflectance r and obtain the thickness d, using a software provided with the equipment. It measures the reflectance in a range of wavelengths from 400

to 1000 nm. The software models the film's reflectance using estimated optical constants for substrate and film, and then fits the measured data using the thickness d as a parameter. Figure 6.1 shows an example of a measured reflectance spectra (open circles), and the fit to the data (line), which yields $d = 345$ nm.
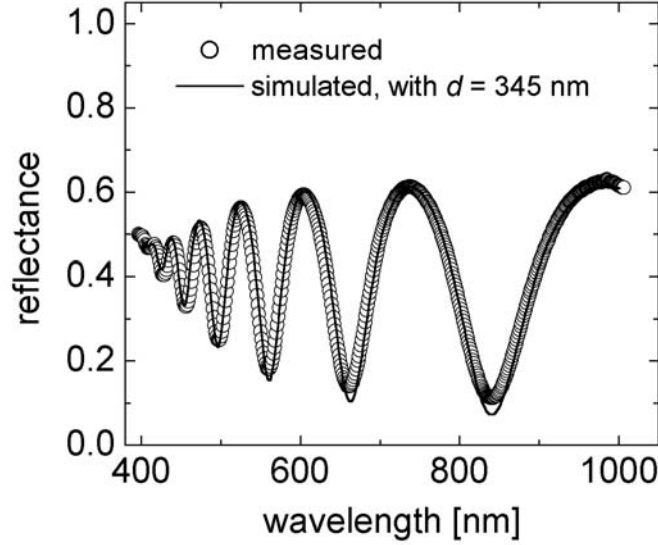

Figure 6.10:   Example of a reflectance measurement (circles) and the corresponding fit (solid line) to determine the film thickness d. The software of the spectrophotometer makes the fit considering single-crystalline silicon parameters.

Knowing the film thickness and the reflectance, we can go further and measure the transmittance, which is needed to determine the absorption coefficient. Taking into account the reflection of light at the surface between air and lc-Si, and at the interface between lc-Si and the substrate, with reflectances r_1 and r_2 respectively, the absorption coefficient α becomes (derived from Eq. A9.1 in Ref. [103])

$$\alpha = \frac{1}{d} ln\left(\frac{-(-r_1 r_2 + r_1 + r_2 - 1) + \sqrt{(-r_1 r_2 + r_1 + r_2 - 1)^2 + 4 r_1 r_2 t^2}}{2t} \right), \qquad (6.15)$$

where d is the film thickness, and t is the measured transmittance. This expression neglects any other reflection events than the two reflections described above. Thus, Eq. (6.15) cannot be used for red and infra-red light, because that light is weakly absorbed by silicon, and therefore reflected several times before absorption (in thin layers in particular). Equation (6.15) also neglects light scattering in the bulk, and light scattering by surface roughness and grain boundaries. Light scattering in the

grains should be small because from the TEM pictures, we know that the density of structural defects, which serve as scattering centers, is very low.

Light scattering at the surface can also be neglected in our films. If the mean roughness of the front surface is smaller than $\lambda/(2\eta)$, being η the refraction index of the film, scattering of light at the surface can be neglected. As shown by Köhler et al. [104], our laser-crystallized films have roughnesses smaller than 5 nm. Taking a c-Si refraction index of $\eta = 5.6$ at $\lambda = 400$ nm, we obtain $\lambda/(2\eta) = 36$ nm. At higher values of λ, η decreases, and $\lambda/(2\eta)$ is much greater than the mean roughness. The condition to neglect light scattering at the surface is thus fulfilled. Optically, the surfaces of these films can be considered flat. The only left process is light scattering at grain boundaries. To simplify the analysis, I neglect this scattering process, but knowing that it can be an error source.

The measurements of the transmittance t were performed using a spectrophotometer. Figure 6.11 shows reflectance and transmittance spectra of a 150 nm thick lc-Si film.[15]

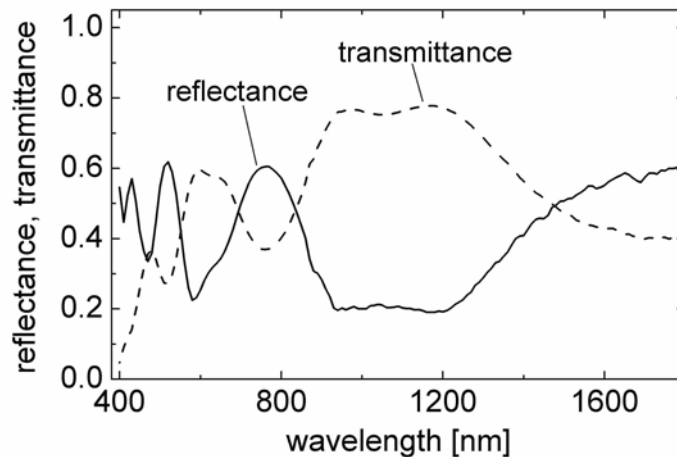Figure 6.11: Reflectance and transmittance spectra a of a laser crystallized film with 150 nm thickness. The spectra are used to calculate the absorption coefficient of the film.

---

[15] A reliable measurement of r and t shows the maxima and minima of r and t taking place at the same wavelenghts, since for the maximum reflection at the front surface, the transmitted light has minimum intensity.

The reflectance r_2 needed to evaluate α from Eq. (6.15), is not accessible via direct measurements. I estimated r_2 considering an interface c-Si/substrate, instead of lc-Si/substrate, using the equation

$$r_2 = \frac{\left|\eta_{c-Si} - \eta_{substrate}\right|^2}{\left|\eta_{c-Si} + \eta_{substrate}\right|^2},$$

(6.16)

where the complex refraction index η_{c-Si} and $\eta_{substrate}$ are taken from literature [105]. After Eq. (6.16), if we use a Corning glass substrate, we get $r_2 = 25~\%$ at $\lambda = 500$ nm.

Since we already obtained d, r_1, r_2 and t, we calculate the absorption coefficient using Eq. (6.15). Figure 6.12 shows the absorption coefficient $\alpha(h\nu)$, for two laser-crystallized films, together with monocrystalline silicon data (solid line) taken from the literature [105] for comparison. The open circles are data of a film with a SiN buffer layer, while the crosses belong to a film crystallized directly on glass. The oscillations observed in some regions of the circles data, arises from a measurement inaccuracy originated in a shift of about 10 nm between the maxima and minima of r and t. The figure also shows us that the laser-crystallized films have α-values about two times higher than c-Si.
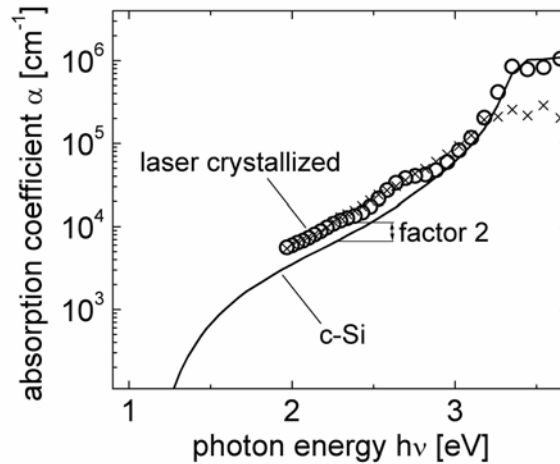
Figure 6.12: Absorption coefficient of laser crystallized silicon films that were deposited directly on glass (crosses) and on a SiN buffer layer (open circles), calculated from transmittance and reflectance data using Eq. (6.15). Light absorption appears to be about two times stronger than in monocrystalline silicon (solid line).

Does lc-Si really absorb more light than monocrystalline silicon? The higher values of α obtained can come from different sources: instrumental errors, light scattering (and thus more absorption) at grain boundaries, absorption at amorphous

residuals within the films, or a larger number of inner reflections than considered in Eq. (6.15). Defect absorption contributes mainly for energies below the band gap, i.e. for $h\nu < 1.1$ eV, and not at the values of energy where we observe the increased absorption. Light scattering at GBs plays a role mainly at small grain sizes [36], and was not detected in thin films with grain sizes of the order of 1-10 μm [107]. Regarding the absorption by amorphous phases, if the films contain a-Si, the experimentally measured absorption coefficient α_{exp} is determined by the volume fractions of each component, by

$$\alpha_{exp} = \beta\alpha + (1-\beta)\alpha_{a-Si}, \qquad (6.17)$$

where β is the crystalline volume fraction, α the absorption coefficient of microcrystalline silicon and α_{a-Si} the absorption coefficient of a-Si. Taking the measured data for example at hν = 2 eV, and the corresponding measured value of $\alpha_{exp} = 1.21\times10^4$ cm^{-1}, Eq. (6.17) gives a value of β = 0.04 (with α = 3.52×10^3 cm^{-1} and $\alpha_{a-Si} = 1.25\times10^4$ cm^{-1} taken from the literature). This value means that about 4 % of our films volume would be amorphous silicon. If we assume that the grain boundaries are amorphous, we can calculate the amorphous content. Estimating a grain boundary width of 1 nm and a grain area of about 1 x 100 μm^2, the relative amorphous volume is less than 0.2 %, well below the 4 % needed to explain the high values of α. Thus, we have to find the suspected 4 % of amorphous content within the grains. The amorphous content of a film can be investigated with Raman spectroscopy. In the case of a-Si, the spectra reveal a broad peak at 480 cm^{-1}, while a narrow peak at about 518 cm^{-1} is found in c-Si. This is also the case of the lc-Si films, as shown by the Raman spectrum of Figure 6.13. This measurement shows no contribution at 480 cm^{-1}, proving that the amorphous content is negligible in our films.
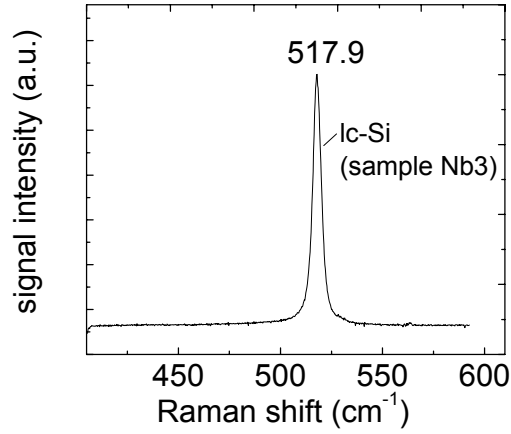
Figure 6.13: This Raman spectra of an lc-Si film indicates that there is no amorphous content in the film. If there were amorphous content, we should see a contribution to the spectra at 480 cm^{-1}, according to the maximum of the Raman peak found in amorphous silicon.

With no a-Si absorption and light scattering at GBs, I suspect that the greater values of α compared to c-Si values could come the estimation of r_2, since the values for $\eta_{substrate}$, taken from literature, may differ from the values of η of the substrates used in this work. These differences surely play a role because we are dealing with thin films, were r_2 cannot be neglected.

With the measured α, we determine the band gap E_g. Indirect semiconductors like silicon, show a quadratic dependence of the absorption coefficient from photon energy $h\nu$, following the relation [106]

$$\alpha \propto \left(h\nu - E_g \pm h\Omega\right)^2 \qquad (6.18)$$

which is valid for values of $h\nu$ smaller than the direct band transition (at $h\nu = 3.4$ eV in silicon), and moderate light intensities. The quantity $h\Omega$ is the phonon energy, which is much smaller than E_g at room temperature. Therefore, the value of $h\Omega$ can be neglected. From equation (6.18), it follows that the band gap can be calculated if the curve $\alpha(h\nu)$ is known. Plotting $\alpha^{1/2}$ against $h\nu$ should yield a straight line, with an $h\nu$-axis intercept given by $E \cong E_g$. Figure 6.14 shows $\alpha^{1/2}(h\nu)$ plots for two different films, the crosses come from a film crystallized directly on glass, and the circles from a film with a SiN buffer layer. Around energies higher than the expected band gap ($h\nu > 1.1$ eV), these plots become a straight line, which gives us the band gap energy E_g. The value of the band gap obtained with the linear fit is E_g = 1.25 ± 0.12 eV, somewhat higher than the c-Si value of 1.12 eV. Is the band gap

really higher than the band gap of c-Si? Jensen measured α using three different measurement methods on polycrystalline films with similar grain sizes as the lc-Si films. His measurements show that the absorption coefficient has the same values as c-Si [107], leading to the same band gap energy. With this information, I conclude that the somewhat higher E_g measured here, comes from the uncertainty introduced by the estimation of r_2, involved in the $\alpha^{1/2}$ plot.
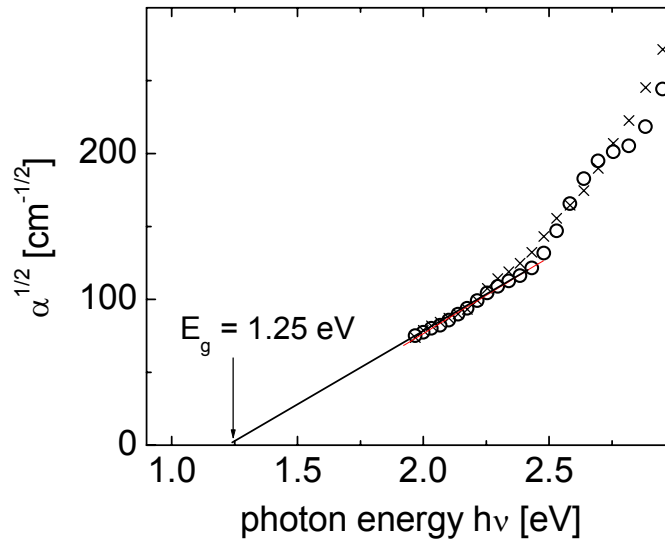

Figure 6.14: Plots of $\alpha^{1/2}$ for two different films, both showing a band gap $E_g = 1.25 \pm 0.12$ eV, obtained from the linear extrapolation of the data. The crosses belong to a film crystallized directly on glass, and the circles to a film with a SiN buffer layer.

6.4 Photoelectrical characterisations

From the previous sections, we know that lc-Si has long, elongated grains. This anisotropic structure influences carrier transport, since carriers flowing parallel to grains will encounter less grain boundaries than when flowing perpendicularly to them. The anisotropy results in an anisotropic resistivity: when transport is parallel to the grains, the resistivity is significantly lower than when it is perpendicular to them. Figure 6.15 shows the current flow parallel and perpendicular to grains. The curved arrows depict possible mean paths of a positive carrier. In the parallel conduction shown in part (a), the carrier flows rather unperturbed through the grain, eventually finding a GB in its path. When the transport is perpendicular, as in part (b), the carrier is forced to go through more grain boundaries than in the parallel case. The grain size relevant to such transport

paths is the mean grain width g_{med}. From now on, I refer to the term *grain size* to the *mean median grain width*, for simplicity.

Figure 6.15: Conduction parallel (part (a)) to grains, and perpendicular to them (part (b)). The electrons paths sketched with the thick, curved lines, show that when the transport is perpendicular to the grains, the electrons will encounter more grain boundaries, resulting a higher resistivity.

I prefer to describe the conduction in the perpendicular direction, because in that case it is clear that every carrier will encounter a grain boundary after traveling a distance of about g_{med}. This scenario resembles the 1D-Model of chapter 4. Therefore, I explain the data obtained with the lc-Si films with the 1D-conduction models.

The electrical characterizations of the films are performed under steady-state and transient conditions. The steady-state characterization involves three methods: conduction type measurements, dark conductivity, and differential photoconductivity. For all these measurements, I used lc-Si films with "T"-shaped contacts, made by evaporation of chromium through a mask. Figure 6.16 shows this contact geometry. The separation between the contacts is 500 μm, and the width is 1 cm.
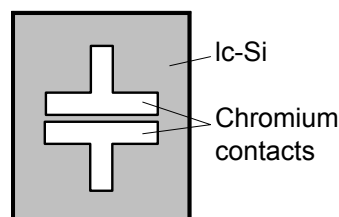

Figure 6.16: Contact geometry used for all the electrical characterizations presented in this section. The electronic transport occurs in the same plane as the film. The contacts are separated by 500 μm, and are 1 cm wide.

Before we get involved with the specific measurements, we need to know the behavior of the Cr/Si contacts, and its influence on the measurement of resistivity. Figure 6.17 (a) shows schematically a band diagram for the Cr/Si contact. The scheme was made using Anderson's rule, which says that the vacuum energy level E_{VAC} must be continuous at the interface, as shown by the figure. This level is given (above the Fermi-level) by the work function $q\phi_m$ of the metal, and by the quantity $q(\chi + E_g - E_F)$ on the semiconductor's side, where χ is the electron affinity. The band diagram assumes literature values for $q\phi_{Cr}$ = 4.6 eV and $q\chi_{c-Si}$ = 4.05 eV. It also assumes that the Fermi-level in silicon lies at midgap, as shown by the dashed line. The interface shown by the dotted lines is a native silicon-oxide, which always appears at room temperature in air.

(a)   (b)
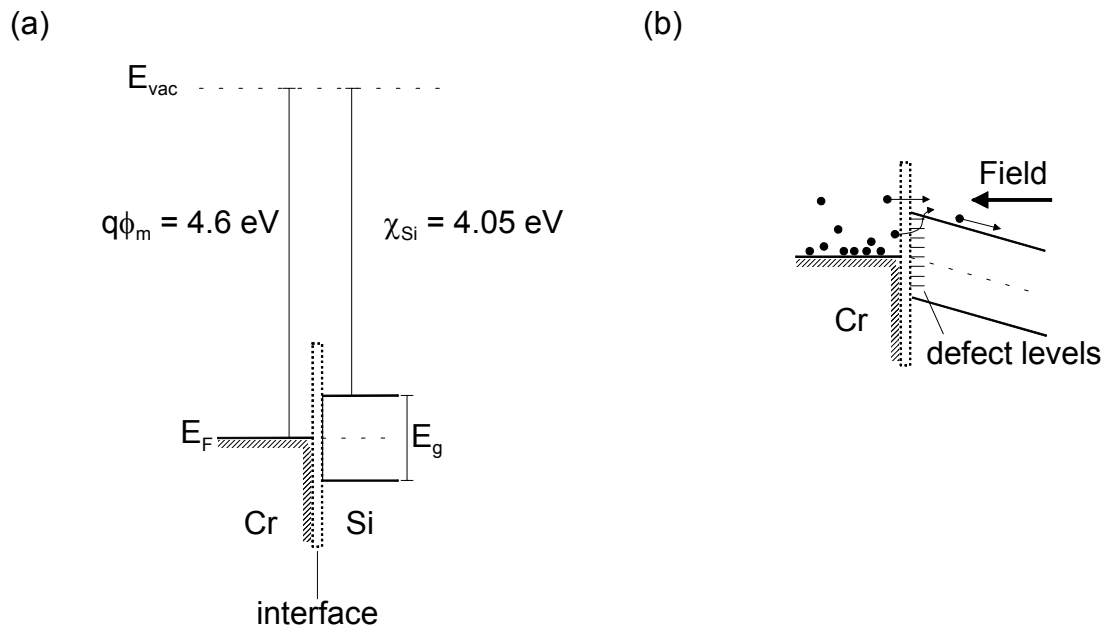
Figure 6.17: Part (a) is a schematic band diagram of a Cr/Si contact. In this case of intrinsic silicon, with the Fermi-level at midgap, the contact to Cr shows no band bending. The interface is a thin native silicon-oxide layer. Part (b) shows the same contact but with an applied electric field, and also adds the energy levels in the forbidden gap of silicon that arise from defects formed at the interface. Carriers tunnel the native oxide because it is very thin. Electrons with high thermal energies reach the conduction band of Si, while electrons with lower energies use the defect levels as conduction path.

Part (b) of Figure 6.17, shows the same band diagram but after applying a potential between the two extremes, making up an electric field (which produces the slope of the bands). Some energy levels in the forbidden gap of silicon were included, representing the defect levels that arise from lattice mismatch with the oxide, and from so-called "metal induced gap-states" (as explained in Ref. [108]). Since the

native oxide is only few nanometers thin, the electrons shown in the picture can tunnel it and get into the semiconductor. Carriers with high thermal energy surpass the energy barrier and make it up to the conduction band in silicon. Low-energy electrons cannot surmount the barrier, and find their way to the silicon using defect levels as conduction paths. Therefore, at low temperatures, the thermal energy of the carriers is so low, that they can enter the semiconductor only by tunneling and using the traps at the interface.

6.4.1 Conductivity type

The conductivity type was obtained with the "hot-probe" method (described in page 42 in [109]). It consists in heating shortly one of the contacts, with a soldering iron for example, and then measure the voltage rise (or drop) between both contacts. If the hot contact shows a positive potential with respect to the cold one, the semiconductor is n-type. A p-type semiconductor gives a negative potential.

All the lc-Si layers made during this work show p-type conductivity, indicating an unintentional doping by incorporation of impurities during the preparation process. Since the crystallization takes place in air, the main source for impurity incorporation is the crystallization process, rather than the deposition of a-Si. An incorporation of impurities from the glass substrate can also be excluded because the samples analyzed here had a SiNx diffusion barrier. Thus, we are aware of the fact that oxygen and nitrogen incorporation is natural to the preparation process. In c-Si, *both* elements have been shown form acceptors or donors (see Ref. [109] for the doping character of oxygen, and Refs. [110] and [111] for nitrogen). The p-type character observed in the lc-Si films indicates that there is a larger number of activated acceptor atoms than donor atoms.

6.4.2 Hall measurements

Hall measurements at small magnetic fields are suitable to obtain the carrier type, the carrier concentration, and the carrier mobility of a semiconducting film. In polycrystalline films, the Hall experiment averages the carrier concentration between the grain center and the grain boundary. Bennet showed that in a polycrystalline material with grains having a dimension much larger than the

other, like lc-Si films, the Hall constant R_H is related to the average carrier concentration $\overline{p}$ by the equation [116]

$$R_H = \frac{F(g, V_b)}{q\overline{p}},$$
(6.19)

where $F(g, V_b)$ is a function which depends on the grain size and the band bending. In low doped samples with a grain size of 1 μm, Bennet calculated $F(g, V_b) = 1$ at V_b = 25 mV, and $F(g, V_b) = 10$ at V_b = 150 mV. Here, since V_b is unknown a priori, I consider $F(g, V_b) = 1$, but bearing in mind that $\overline{p}$ could be an order of magnitude larger.

To measure R_H in the lc-Si films, I utilized the Van der Pauw technique using a cloverleaf-shaped sample (see page 523 in Ref. [103]). The magnetic field strength was 0.5 Tesla, and the current was set to 0.1 μA. The results obtained for R_H have a large error of about 150 % because it was technically difficult to measure the Hall voltage with a good precision. This difficulty comes from the problem that, since the lc-Si samples have a high resistivity, the voltage measured at the hall contacts *without* magnetic field, is much greater than the Hall voltage, making a determination of the Hall voltage difficult. Nevertheless, it is useful to know $\overline{p}$ within a range of an order of magnitude. The values of $\overline{p}$ obtained considering a value of $F(g, V_b)$ of 1 and 10, are respectively $\overline{p} = 4 \times 10^{12}$ and $\overline{p} = 4 \times 10^{13}$ cm^{-3}. This indicates that the impurity dopants compensate each other strongly, yielding the low measured carrier concentration. Additionally, the band bendings at the GBs must be very low, and the space-charge regions around the GBs must reach the grain centers. The range of $\overline{p}$ determines a range of the Hall mobility μ_H, given by $\mu_H = R_H/\rho$ [103], by $12 < \mu_H < 120$ cm^2/Vs. The latter value is of the same order of magnitude of the mobility measured by the photoconductivity measurements presented below.

We can now estimate the position of the Fermi-level in the middle of the grains as follows. Considering small band bendings, the concentration of holes in the middle of the grains approaches $p_0 = \overline{p}$. Taking both values of $\overline{p}$ respectively, the Fermi-level would lie between 0.41 and 0.35 eV above the valence band edge.

It is worth to note that the oxygen acceptor in c-Si shows an energy level at 0.41 eV above the valence band [109]. In the present case, this would mean that the Fermi-level lies close to the acceptor level. The measurement of the temperature-dependent dark conductivity provides more information about the position of the Fermi-level.

6.4.3 Dark conductivity

To obtain the temperature-dependent dark conductivity, I apply a constant voltage of 50 V between the T-contacts of the sample, and measure the current, in the temperature range from 150 to 450 K. The current density J and the electric field F, give the conductivity $\sigma = J/F$. At room temperature, the conductivities perpendicular to the grains show values of about 10^{-4} $\Omega^{-1}cm^{-1}$. Parallel to the grains, σ is between one to two orders of magnitude greater than in the perpendicular case, namely between 10^{-3} and 10^{-2} $\Omega^{-1}cm^{-1}$. This strong dependence from conductivity on conduction direction, drives us to the following conclusions:

1. surface scattering effects on conductivity are negligible, as shown in chapter 4. If surface scattering would dominate transport, the actual conduction direction would have no influence on the conductivity σ, and

2. conduction is *strongly* dominated by grain size, and hence by the grain boundaries. The difference of one to two orders of magnitude between σ in each direction, corresponds to the difference of one to two orders of magnitude between grain width (around 1 μm) and grain length (up to 100 μm).

Since the measured conductivity reflects directly the conduction in the film (and not through its surface), the 1D model for conductivity of chapter 4 is suited to evaluate the data. Due to the p-type nature of the films, I neglect the electron conduction, assuming that the total resistivity is due to holes. The resistivity ρ of a single grain is given by

$$\rho = \frac{1}{q\mu_{pGB}p_{GB}}\frac{\delta}{g_{med}/2} + \frac{1}{q\mu_p p_0}\frac{\sqrt{\pi}\,\mathrm{erfi}\left(\sqrt{V_b/V_t}\right)}{2\sqrt{V_b/V_t}}, \qquad (6.20)$$

where δ is the width of the grain boundary. The subscript "GB" denotes grain boundary properties, while "0" indicates properties at the center of the grain. In Eq.

(6.20), I supposed completely depleted grains, assuming that the width W of the SCR is equal to $g_{med}/2$. This assumption makes sense, because the lc-Si films are undoped. Here, I am interested in the temperature dependence of ρ and of the conductivity $\sigma = 1/\rho$. Neglecting the temperature dependence of the mobilities, we find that the only temperature dependent terms in Eq. (6.20) are p_{GB}, p_0 and the term containing the error function. With the barrier height $q\Phi$ and the energy difference $q\zeta$ between Fermi-level and valence band edge at the center of the grain, defined in Figure 6.18, and the corresponding expression for p (see chapter 2), the quantities p_{GB} and p_0 are expressed as a function of the temperature T by

$$p_{GB} = N_{GB} \exp\left(\frac{-q\Phi}{kT}\right),$$
(6.21)

where N_{GB} is an effective density of states at the grain boundaries, and

$$p_0 = N_V \exp\left(-\frac{q\zeta}{kT}\right).$$
(6.22)

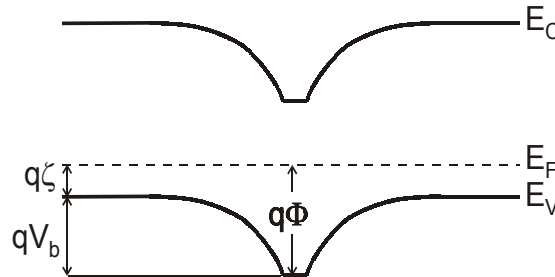Figure 6.18: Band diagram of a grain boundary in p-type Si, showing the barrier height $q\Phi$.

As explained in chapter 4, the term in Eq. (6.20) with the error function has a temperature dependence of the form $\exp(qV_b/kT)$. Thus, considering Eqs. (6.20) and (6.22), the resistivity of the SCR is proportional to $\exp[q(\zeta + V_b)/kT]$. Inspecting the band diagram of Figure 6.18, we note that $\zeta + V_b = \Phi$. This means that both, the resistivity of the SCR and of the GB, show *the same* temperature dependence. Hence, the total resistivity of a *single* grain is proportional to $exp(q\Phi/kT)$ (and the conductivity is proportional to $exp(- q\Phi/kT)$).

At this point of the discussion, we can expect that the conductivity measured in a sample with *many* grains is expressed by the proportionality $\sigma \propto exp(-E_A/kT)$,

where E_A is defined as the activation energy of the conductivity. From an Arrhenius plot of $\sigma(T)$, E_A is calculated using

$$E_A = -k \frac{d(\ln \sigma)}{d(1/T)}. \tag{6.23}$$

In the case of the isolated grain boundary of Figure 6.18, the Arrhenius plot of $\sigma(T)$ must yield a constant value $E_A = q\Phi$, independently of T.

Figure 6.19 shows typical plots of $\sigma(T)$ measured in lc-Si samples, which show a curved Arrhenius characteristic. After Eq. (6.23), this curvature means that E_A *varies* with $1/T$. Such curved Arrhenius plots appear also in other types of polycrystalline silicon [114]. The samples shown in Figure 6.19 have different grain sizes, Na23 has a grain width g_{med} = 0.66 μm, and sample Na46 has g_{med} = 0.91 μm. The $\sigma(T)$ curves are plotted separately because they lie close to each other.
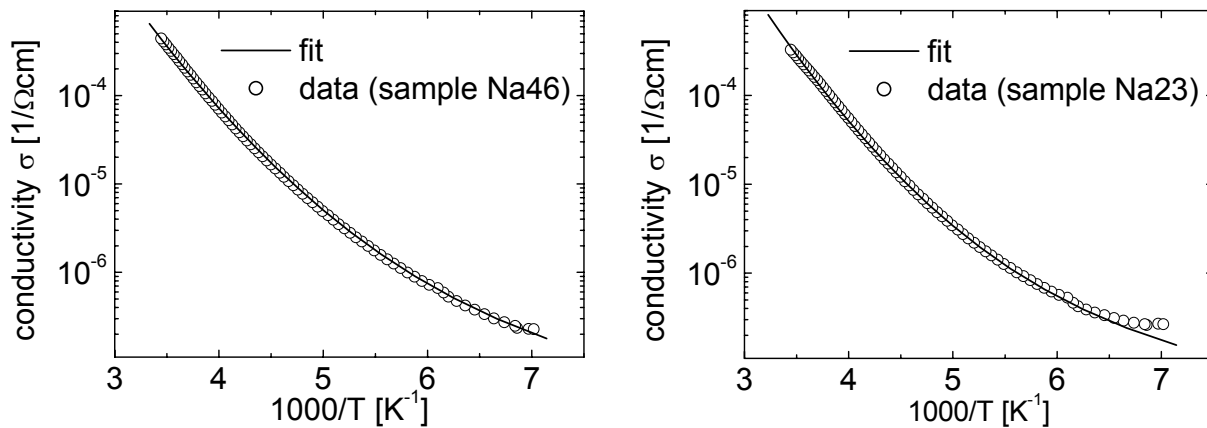

Figure 6.19: These Arrhenius plots of the conductivity in two different samples are curved. The curvature implies that there is a distribution of activation energies, and is explained by the fits (solid lines) provided by the model of grain boundary barrier height inhomogeneities given in the text.

The curved Arrhenius plots were successfully explained by a model that considers a *distribution* of activation energies given by J.H. Werner [114]. The model properly explained curved Arrhenius plots of $\sigma(T)$ measured in many different polycrystalline semiconducting materials [114]. The idea behind a distribution of the activation energy relies in a physically realistic explanation: the trap and impurity densities, and hence the charge density at the grain boundaries, vary from grain to grain. These inhomogeneities of grain boundary charges give different band bendings, and hence different barrier heights. All these different barrier heights result in the value of E_A extracted from the $\sigma(T)$ measurement. Note

that it is more realistic to assume spatial inhomogeneities of the charge at the GBs than supposing the same charge density at *all* the GBs involved. Considering that the barrier heights are described by a gaussian distribution, Werner showed that measured activation energy E_A must follow a linear dependence of $1/T$ given by [114]

$$E_A(T) = q\left(\overline{\Phi}_0 - \frac{\sigma_\Phi^2}{kT/q}\right), \qquad (6.24)$$

where $q\overline{\Phi}_0$ is the *mean barrier height* at the GBs at $1/T = 0$ K^{-1}, and σ_Φ the standard deviation of the distribution.

Within this model, an Arrhenius plot of E_A yields a straight line (*if* the distribution of barrier heights is gaussian). Figure 6.20 shows that the lc-Si samples have a a linear dependence of E_A from $1/T$. Fitting the data with (6.24), we find $\overline{\Phi}_0$ = 530 mV and σ_Φ = 76 mV for sample Na46, while sample Na23 is fitted using $\overline{\Phi}_0$ = 610 mV and σ_Φ = 85 mV. These values of $\overline{\Phi}_0$ and σ_Φ are typical in low-doped polycrystalline silicon [114]. Here, I assume that the values of $\overline{\Phi}_0$ are approximately independent of T.
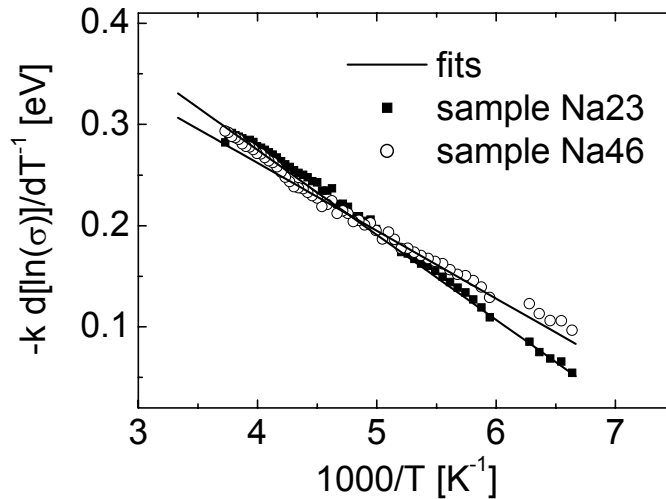
Figure 6.20: The activation energies shown in this plot give the barrier height at the grain boundaries. The model of barrier inhomogeneities explained in the text predicts the values of the mean barrier height $\overline{\Phi}$ at the grain boundary at 0 K, and its standard deviation σ_ϕ. The fits using the model yield $\overline{\Phi}_0$ = 0.53 eV, σ_Φ = 76 mV for sample Na46, and $\overline{\Phi}_0$ = 0.61 eV, σ_Φ = 85 mV for sample Na23.

With the values of $\overline{\Phi}_0$, we know the mean position of the Fermi-level at the grain boundary, but not the band bendings. However, we can estimate the band

bending V_b by assuming that the Fermi level in the grains lies just at the shallowest acceptor level produced by oxygen in c-Si, at 0.41 eV above the valence band, as suggested by the Hall measurements. Thus, the band bending is then given by qV_b = $q\overline{\Phi}_0$ − 0.41 eV. For example, sample Na46 has qV_b = 0.53 eV − 0.41 eV = 0.12 eV.

With the values of V_b, and the carrier concentrations obtained from the Hall measurements, it is possible to extract the defect density at the GBs using the 1D-model of chapter 4. Here, I obtain a minimum defect density by assuming that all defect levels are filled. Since the actual carrier concentration in the center of the grain p_0 must be greater than $\overline{p}$, I assume that p_0 is at least equal to the largest value of $\overline{p}$ obtained with the Hall measurements. Thus, using $p_0 = 4\text{x}10^{13}$ and V_b = 0.12 V, the minimum defect density N_t^0 becomes

$$N_t^0 = \sqrt{\frac{8\varepsilon_0\varepsilon_S\, 4\text{x}10^{13}\,\text{cm}^{-3}\,0.12\,\text{V}}{q}} = 1.6\text{x}10^{10}\,\text{cm}^{-2}, \tag{6.25}$$

This value is rather low, compared to polycrystalline silicon films obtained by other methods, where N_t ranges between 10^{11} to 10^{13} cm^{-2} [112]. But we have to bear in mind that this value is a minimum value.

With N_t^0, we can go a step further and estimate the lifetime in the lc-Si films. If we distribute the total number of defects at the grain boundaries uniformly through the grain, we obtain an effective density N_{eff} of defects per unit volume. The validity of this approach has been proved by Green [113]. In the case of lc-Si films, where the length L of the grain is much larger than g_{med} and than the film thickness d, N_{eff} becomes

$$N_{eff} = \frac{2}{d}N_t^0 = 1.6\text{x}10^{15}\,\text{cm}^{-3}, \tag{6.26}$$

assuming a typical layer thickness of d = 200 nm. With N_{eff}, which is a minimum value, we can define a *maximum* lifetime τ^* by (see chapter 2),

$$\tau^* = \frac{1}{v_{th}\sigma_n N_{eff}}. \tag{6.27}$$

With $v_{th} = 10^7$ cm/s, a capture cross section of minority carriers of 10^{-15} cm^2, and N_{eff} = $1.6\text{x}10^{15}$ cm^{-3}, Eq. (6.27) gives τ^* = 62.5 ns. This is a rough estimate, since the value of the capture cross section should be measured instead of estimated.

6.4.4 Photoconductivity

The photoconductivity is the conductivity measured under optical illumination. The differential conductivity $\Delta\sigma$ is the difference between σ under illumination and its dark value. The measurement of $\Delta\sigma$ permits the evaluation of the product between carrier mobility and a minority carrier effective recombination lifetime τ_{eff}. This lifetime includes recombination of minority carriers at GBs, in the bulk, and at the film's surfaces. It is worth to note that if the generation rate is so low that the increase of resistivity is much lower than the dark resistivity, i.e. $\Delta\rho <<$ ρ, the change in conductivity is given by

$$\Delta\sigma = \frac{\Delta\rho}{\rho^2} .$$

(6.28)

Next, I find an expression for $\Delta\rho$ considering the expression for the resistivity ρ of a polycrystalline sample given in chapter 4, and relating it to the generation rate. Under illumination, the hole and electron concentrations increase by Δp and Δn ($= \Delta p$). With a generation rate G, the change in the carrier concentration Δn is given by

$$\Delta n = G\tau_{eff} ,$$

(6.29)

After Beer's law, if the reflectance at the surface of the film is r, and the incident photon flux is ϕ_{phot}, the generation rate is given by

$$G = \frac{(1-r)\phi_{phot}\left(1 - e^{-\alpha d}\right)}{d} ,$$

(6.30)

where d is the film thickness and α the absorption coefficient at the wavelength chosen for the experiment.

Now I obtain an equation for $\Delta\sigma$ using the equations of the resistivity. Expressing the hole resistivity ρ_p from Eq. (6.20) by

$$\rho_p = \frac{2\delta}{g_{med}}\rho_{pGB} + \rho_{p0} ,$$

(6.31)

where ρ_{pGB} is the resistivity of the grain boundary, and ρ_{p0} the resistivity of the SCR. If we consider an analogous expression to (6.31) for the electron resistivity, and assume that the carrier densities increase by Δp and Δn upon illumination, the change $\Delta\rho$ of the total resistivity can be expressed by the equation

$$\Delta\rho = \frac{2\delta}{g_{med}}\Delta\rho_{GB} + \Delta\rho_0 , \tag{6.32}$$

where $\Delta\rho_{GB}$ and $\Delta\rho_0$ are the total changes in resistivity given by holes *and* electrons at the grain boundary and in the bulk, respectively. From this equation, we note that a plot of $\Delta\rho$ vs. $1/g_{med}$ gives a straight line, with a slope given by $2\delta\Delta\rho_{GB}$, and a $\Delta\rho$-axis intercept $\Delta\rho_0$. Using the measured value of $2\delta\Delta\rho_{GB}$, we can estimate the mobility-lifetime product $\mu_{GB}\tau_{eff}$ as follows: the differential conductivity $\Delta\sigma_{GB}$ of the grain boundary is given by

$$\Delta\sigma_{GB} = q\left(\mu_{pGB}\Delta p + \mu_{nGB}\Delta n\right) = q\left(\mu_{pGB} + \mu_{nGB}\right)\Delta n . \tag{6.33}$$

For simplicity, I define a mean grain boundary mobility μ_{GB}, given by $\mu_{GB} = (\mu_{pGB} + \mu_{nGB})/2$. Replacing this definition in Eq. (6.33) and using Eqs. (6.28) and (6.29), the product $\mu_{GB}\tau_{eff}$ becomes

$$\mu_{GB}\tau_{eff} = \frac{1}{2qG}\frac{\Delta\rho_{GB}}{\rho^2} . \tag{6.34}$$

The measurements of photoconductivity were done using blue light with a wavelength of 400 nm, at which $\alpha = 10^5$ cm^{-1}, and $r \approx 0.5$. The photon flux, measured with a calibrated solar cell, is $\phi_{phot} = 4.4 \times 10^{12}$ photons/cm^{2}s. Since the film thickness of the samples is $d = 150$ nm, Eq. (6.30) gives $G = 1.1 \times 10^{17}$ cm^{-3}s^{-1}. The variation in the current from the dark to the light state, is measured with a modulation method (described in Ref. [117]).

Figure 6.21 shows the increase of photoresistivity with g_{med} found experimentally in the lc-Si films. The dispersion of the data at same values of $1/g_{med}$ arises from samples separated some centimeters on the substrates. However, it cannot be discriminated between an actual difference in resistivity, or if the contacts have slightly different resistances in each case.

The solid line in Figure 6.21 is a linear fit to the data, showing the linear dependence predicted by Eq. (6.32). The linear fit yields a slope of 3.3×10^3 Ωcm^2 (with a 20 % error). This value corresponds to the product $2\delta\Delta\rho_{GB}$ (see Eq. (6.32)). The independent term $\Delta\rho_0$ has an error larger than its magnitude and is therefore unreliable, but nevertheless sufficient to indicate that the intra-grain resistivity is much lower than the GB resistivity.
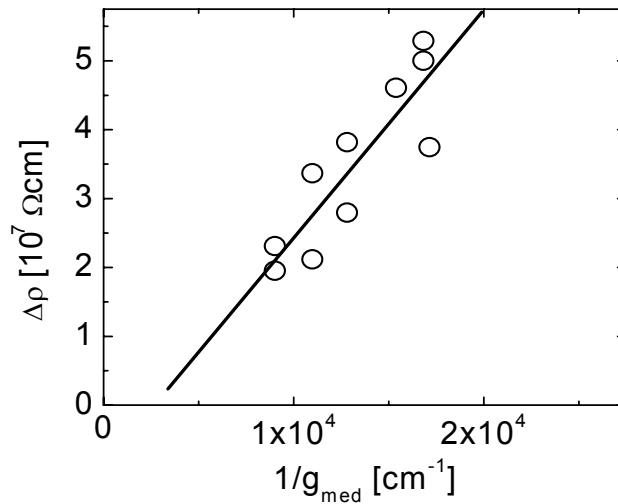
Figure 6.21 The differential photoresistivity $\Delta\rho$ shows approximately a linear relation with $1/g_{med}$. This linear dependence means that the electrical transport in the laser-crystallized films is dominated by the grain boundaries. The dispersion of the data comes from samples that were prepared from regions of the substrate separated by some centimeters.

Now I utilize Eq. (6.34) to calculate the $\mu\tau$-product of the lc-Si films. With a grain boundary width of 1 nm, the set of samples from Figure 6.21 show $\mu_{GB}\tau_{eff} = 2.3\times10^{-5}$ cm^{2}V. Assuming that τ_{eff} reaches the maximum value of 62.5 ns calculated in the previous section, the mobility is $\mu_{GB} = 368$ cm^2/Vs. This value seems reasonable, since it is of the same order of magnitude as the field effect mobility μ_{FE} reached by TFTs made from lc-Si. Indeed, TFTs having lc-Si layers of the same thickness and grain size, and the grain boundaries also perpendicular to current flow, reach $\mu_{FE} \approx 210$ cm^2/Vs [115]. An exact match between μ_{FE} and μ_{GB} should not be expected, because μ_{FE} depends on the dimensions of the channel, and the oxide thickness (see page 441 in Ref. [13]).

6.5 Test diodes

The analysis of the current/voltage characteristics of diodes made with lc-Si gives us information about the transport parameters, which do not provide neither the resistivity nor the photoconductivity measurements. In a vertical diode, the current flow takes place perpendicularly to the film, not in the same plane of it. Since the film's structure is columnar, with the grain boundaries going from front to back of the layer, most of the carriers flowing through the diode will not encounter grain boundaries. Thus, the electrical transport parameters provided by an analysis

of the current/voltage characteristics, correspond mainly to intra-grain properties. This statement is true provided the band bending induced by the grain boundaries is not large, i.e. for undoped films, and for thin films. The lc-Si films studied here fulfill both conditions. The only quantity still dominated by grain boundaries is the carrier lifetime, since carriers recombine mainly at the grain boundaries, were the defect concentration is much higher than in the grains.

6.5.1 Diode structure

The diodes are composed of five layers deposited onto a glass substrate in the following sequence: chromium (front contact), lc-Si (active layer), nanocrystalline-Si (p-type), and an aluminum layer as back contact. Figure 6.22 (a) shows the layers that constitute the diode. Figure 6.22 (b) presents the band diagram for this structure, which is sketched using Anderson's rule taking literature values for the work functions of Cr and Al, and c-Si values for the electron affinity of nc-Si and lc-Si. Since the lc-Si is undoped, and the thickness of the layer is about 300 nm, no appreciable SCR (and hence no band bending) builds up at the Cr/lc-Si interface. I assumed that the lc-Si has its bulk Fermi-level at 0.5 eV above the valence band edge, according to the values of the Fermi-level taken from the $\sigma(T)$ measurements. This fixes the relative positions between the bands and the common Fermi-level at the Cr/lc-Si interface.

With no significant SCR, the bands in the lc-Si become straight lines, as seen in part (b) of Figure 6.22. The Fermi-level in the nc-Si lies at about 100 meV above the valence band edge (corresponding to carrier density of about $p = 10^{18}$ cm^{-3}, measured with the Hall technique). The nc-Si layer is about 200 nm thick. At the interface to the aluminum contact, a very high and narrow barrier builds up in order to align the vacuum levels at the nc-Si/Al interface, satisfying Anderson's rule. I will further assume, that due to the very narrow barrier, this contact is ohmic. The built-in potential V_{bi} of the diode is given by energy difference between the bands at the Cr/lc-Si interface and the lc-Si/nc-Si interface. Following the band diagram, a value for V_{bi} of around 500 mV arises for this structure. Indeed, the analysis of the current/voltage characteristics shown below, yields V_{bi} = 490 mV.

It is possible to understand the Cr/CrSi$_2$/lc-Si contact of Figure 6.22 (b) as a Schottky contact with approximately equal barrier heights for electrons and holes. Here, I assume that under <u>forward bias</u> conditions, this contact injects electrons into the lc-Si, and that the electron current is equal to the hole current injected from the Al into the nc-Si. Additionally, I assume that the recombination velocity of minority carriers at each contact is infinity. Considering this assumptions, I model the test diodes as *pin* diodes with a narrow space-charge region, as explained below.
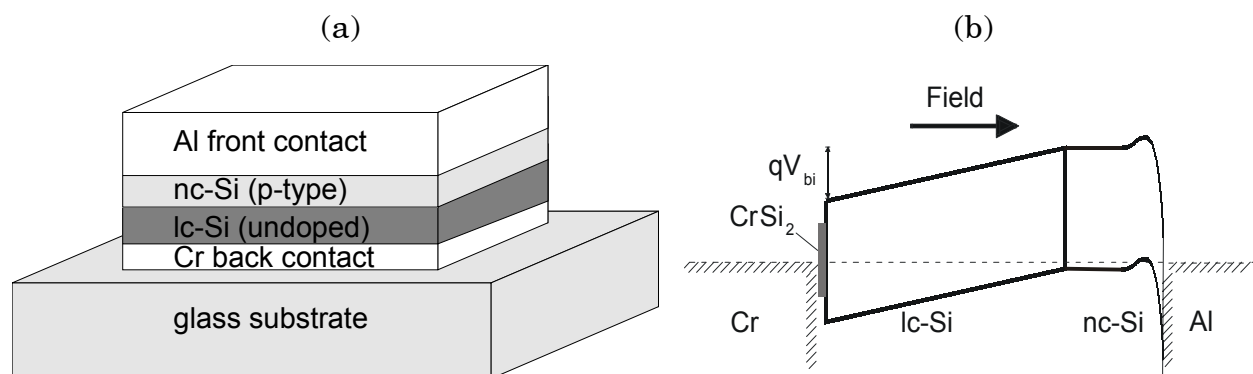

Figure 6.22: Part (a) shows the different layers deposited to make the diode. Note that the lc-Si is crystallized on the chromium contact. With chemical vapor deposition, a nc-Si layer is deposited on the lc-Si film to make the front contact with the evaporated Al layer. Part (b) sketches a model for the band diagram of this structure. The bands are drawn using Anderson's rule and respecting the positions of the Fermi-level corresponding to each layer. No appreciable SCR is found near the lc-Si/nc-Si interface, resulting the straight bands shown for the lc-Si layer.

6.5.2 Preparation

The diodes are prepared by evaporating about 40 nm Cr on a cleaned Corning glass, and depositing the a-Si to be crystallized on it using PECVD. The PECVD[16] involves first a hydrogen plasma etching to clean up the Cr surface, followed by the deposition of intrinsic a-Si at about 250 °C substrate temperature, and 30 W plasma power (at 13,56 MHz). The chamber pressure was 800 mTorr, using a SiH$_4$ flow of 30 sccm and an H$_2$ flow of 10 sccm. These deposition conditions are employed specifically to incorporate the lowest possible amounts of hydrogen into de films, enabling their tempering after deposition[17]. After deposition, the layers are tempered in a quartz oven with a 30 sccm nitrogen flow, for 6 hours at a

---

[16] The a-Si depositions were performed by J. Glöckner at our institute, to whom I am very grateful for his time and cooperation.

[17] Films with high hydrogen content show bubbles or "blow ups" when tempered.

temperature of 450° C. The next step is laser crystallization, which I did using 20 KHz pulse frequency, a scan velocity of 10 mm/s, and laser powers between 450 and 500 mW (depending on film thickness). The crystallized layers are then dipped in a 5 % concentrated HF-solution to remove native oxides formed at the surface of the films. After the dipping, highly doped p-type nc-Si layers are deposited on the lc-Si by the Hot Wire Chemical Vapour Deposition method[18]. Immediately after the nc-Si depositions, the films are brought to a metal evaporation chamber for the last processing step. I evaporated aluminium on top of the nc-Si, using a shadowing mask with round openings for the metal contacts, which have a diameter of 2 mm. The resulting diode's area is then 0.031 cm^2.

6.5.3 Current/voltage characteristics

The current(I)/voltage(V) characteristics were measured under dark conditions. The analysis of the I/V-characteristics gives us the built-in potential, the µτ-product and the diffusion constant of the lc-Si layers.

Before we can extract any information from the I(V) curves, we have to correct them with the series- and parallel resistance of the diodes (R_S and R_P, respectively), which are not included in the physical models for the I/V-characteristics. We can expect a priori a high series resistance, because the Cr-layers are very thin, and a low parallel resistance because the cells are very thin. Such combination of high R_S and low R_P will strongly modify the shape of the I(V) curves, being a correction mandatory. Here, I use the correction method described in Ref. [103], which yields accurate values of the series and parallel resistance, permitting a reliable correction of the I(V) curve. Figure 6.23 shows the measured and corrected I(V) curves of one of the diodes. I model the J/V-characteristics and extract physical parameters from the corrected curves.

In order to extract the physical parameters of the diode's material, we have to find a model for the I/V-characteristic. The band diagram of Figure 6.22 resembles the constant field region assumed for the *pin* diode described in chapter 5, where we had an intrinsic layer sandwiched between two contacts.

---

[18] I would like to thank Ch. Koch for his kind cooperation depositing the nc-Si layers at our institute.
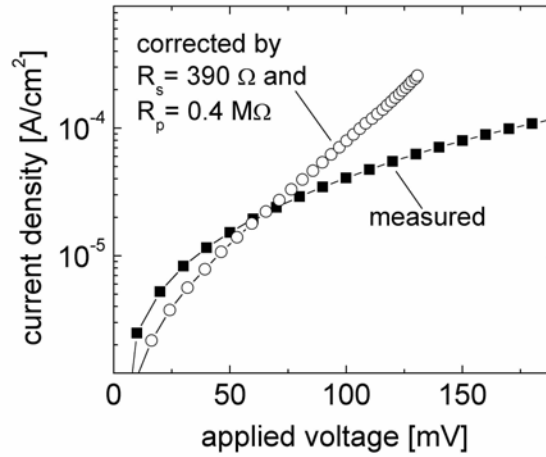
Figure 6.23: Typical measured and corrected current/voltage curves shown by test diodes. This sample shows a series resistance R_S = 390 Ω, and a parallel resistance R_P = 0.4 MΩ.

The model of the *pin* cell gives different simplified expressions for the I/V-characteristics, depending on the distinguishing features in each case. The most significant difference between each expression is reflected by the value of the diode's ideality factor n_{id}. The corrected I/V-characteristics of the test diodes analyzed here, show values of n between 1.0 and 1.15. After the model of the *pin* diode presented in this work, an ideality near unity appears when the current is dominated by surface recombination. If we consider a very high recombination velocity and a narrow i-layer (below 0.5 μm), and considering a voltage $V > 0$, the current density can be written as (see Appendix B)

$$J = \frac{2qn_{p0}D}{W}\frac{V_{bi}-V}{V_t}\exp(V/V_t),$$
(6.35)

which has an ideality of 1, as seen in the exponential term. The restriction of a narrow i-layer applies to the present case, because the lc-Si layer is only 300 nm thick. High recombination at the boundaries of the i-layer is also expected, since the contacts are not treated in any way to reduce the recombination. Under all these conditions, Eq. (6.35) is correct for the case under study.[19] Putting all the measured quantities in Eq. (6.35) on the left hand side (l.h.s), we obtain

$$\frac{V_t W J}{2q\exp(V/V_t)} = n_{p0}D(V_{bi}-V).$$
(6.36)

---

[19] Eq. (6.35) assumes that electron and hole currents are equal, resulting the factor 2.

If we plot the l.h.s. of this equation against V, we get a straight line with negative slope. The intercept of the V-axis is given by V_{bi}, and its slope by $n_{p0}D$. Figure 6.24 shows this linear behavior on a test diode, where the intercept yields a built-in voltage of 0.49 V, and a slope $n_{p0}D = 1.2 \times 10^7$ cm^{-1}s^{-1}.
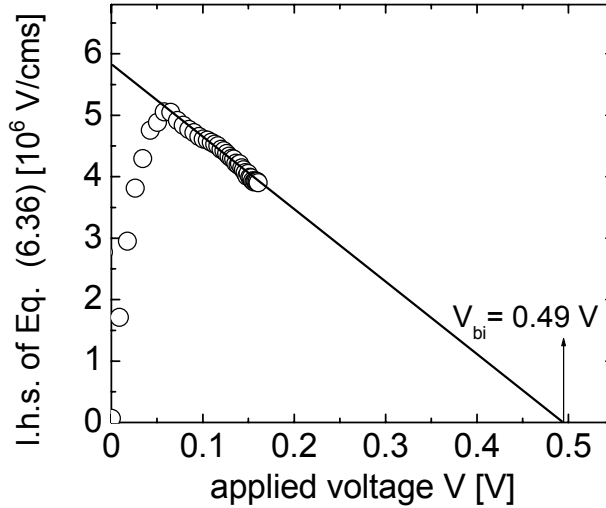

Figure 6.24: If we plot the left hand side of Eq. (6.36) against the applied voltage, we obtain a linear region, as shown in this example. The axis intercept reveals a built in voltage of 0.49 V. The slope gives the product between the diffusion constant D, and the minority carrier concentration n_{p0} at the interfaces between the i-layer and the contacts of the diode. In this example, $n_0D = 1.2 \times 10^7$ cm^{-1}s^{-1}.

It is possible to estimate the diffusion constant from this slope, by estimating the value of the density of electrons n_{p0} at the i/p interface. Assuming that the i-layer has a majority carrier concentration $p = 4 \times 10^{13}$ cm^{-3},[20] we obtain a minority carrier concentration in the i-layer of $n_i = 2.5 \times 10^6$ cm^{-3}. Deep in the p-layer the majority carrier concentration of 10^{18} cm^{-3} imposes a minority carrier concentration $n_p = 10^2$ cm^{-3}. Thus, the value of n_{p0} is restricted to $n_{p0} < 2.5 \times 10^6$ cm^{-3}. The diffusion constant D extracted from the slope $n_{p0}D$ is then given by $D > 4.8$ cm^2/s, i.e. a mobility $\mu > 187.5$ cm^2/s. The order of magnitude of this mobility value is in agreement with the values extracted from photoconductivity measurements, where $\mu_{GB} = 368$ cm^2/Vs, and the upper Hall mobility $\mu_H < 120$ cm^2/Vs. With V_{bi}, n_0D, and the thickness W of the i-layer, it is possible to estimate the product between lifetime

---

[20] This carrier concentration is the maximum value given by the Hall measurements of lc-Si samples crystallized on SiNx, as described in section 6.4.

and diffusion constant contained in the saturation current density J_0, using the equation (explained in Appendix B)

$$J_0 = 2qn_{p0}D\left(\frac{\exp\left(-V_{bi}/2V_t\right)}{\mu\tau F_0} + \frac{F_0}{V_t}\right),\qquad(6.37)$$

which is valid for high recombination velocities at contacts.[21] The values of J_0 obtained from the corrected J(V) curves lie around 2×10^{-6} A/cm^2 (with 30 % deviation among all diodes analyzed). In order to reach this value of J_0, Eq. (6.37) imposes $\mu\tau$ $\cong 4\times10^{-6}$ cm^2/V. Assuming $\mu = 187.5$ cm^2/s, we obtain $\tau = 21$ ns. This value is of the same order of magnitude as the estimate of the maximum lifetime $\tau^* = 62.5$ ns obtained from the analysis of the band bendings at the GB (see Eq. (6.27)).

6.6 Conclusions

The analyses presented in this chapter describe the electronic properties of undoped lc-Si films by the following results:

i)   The type and resistivity measurements indicate that the films crystallized on a SiN buffer layer are slightly p-type, most probably due to the incorporation of oxygen during the crystallization in air. The Hall measurements give a hole density between 4×10^{12} and 4×10^{13} cm^{-3}, and a mobility between 12 and 120 cm^2/Vs. The temperature-dependent measurements of conductivity show a distribution of grain boundary band bendings, with a mean band bending around 120 mV. An estimation of the minimum areal defect density at the grain boundaries yields 1.6×10^{10} cm^{-2}. Such a low density corresponds to a minority carrier lifetime of 62.5 ns, or to a recombination velocity S_{GB} at grain boundaries in the range 100-1000 cm/s (see chapter 4).

ii)   The photoresistivity shows that, when the transport takes place in the plane of the film, the grain boundaries dominate the resistivity, with a negligible resistivity of the intra-grain regions, resulting resistivities

---

[21] This expression differs from Eq. (5.10), because (5.10) is only valid for a cell thicker than 500 nm, with a built-in voltage higher than 0.7 V.

around 10^4 Ωcm at 300 K. The grain size dependence of the photoresistivity is explained by the conductivity model of chapter 4, permitting a rough estimation of the μτ-product, yielding μτ = 2.3x10^{-5} cm^2/V. With a lifetime of 62.5 ns, the mobility of the films is 368 cm^2/Vs, in agreement with the values of field-effect mobilities obtained in transistors prepared with this type of films. Such values of the mobility are close to monocrystalline silicon values.

iii)   The analysis of the J/V-characteristics of test diodes yield a mobility around 190 cm^2/Vs, which is of the same order of magnitude as the mobilities obtained from the Hall and photoresistivity measurements. The J/V curves give also a μτ-product that must be of the order of 4x10^{-6} cm^2/V (implying a lifetime around 21 ns). The value μτ = 4x10^{-6} cm^2/V should not be compared to the value of μτ obtained in (ii), because the test diodes do not use a SiNx layer as diffusion barrier, implying a higher impurity concentration. The value μτ = 4x10^{-6} cm^2/V is still high compared to typical nc-Si values of around μτ = 5x10^{-7} cm^2/V (see chapter 5).

Herewith, I characterized the lc-Si films optically as well as electrically. The photoelectrical characterizations give a complete picture of the basic transport parameters of lc-Si, which were *unknown* up to know. Figure 5.11 indicates that solar cell efficiencies of up to η = 6 % are possible at μτ = 5x10^{-7} cm^2/V. At the value μτ = 4x10^{-6} cm^2/V reached by the lc-Si films obtained in this chapter, a calculation with the model of chapter 5 yields η ≈ 8 %, at a cell thickness of 4 μm.[22] The Nd:YVO$_4$ laser utilized in this work does not sustain a SLS-growth at thicknesses greater than 0.3 μm. Probably, a more powerful laser is needed to prepare thicker films suited for solar cells. Nevertheless, the high values of the μτ-product obtained here suggest, at least, that the reliability of lc-Si for minority carrier devices such as solar cells or bipolar junction transistors deserves further investigation.

---

[22] The remaining quantities involved in this calculation are the same as those utilized in Figure 5.11.

Appendix A

In this appendix I show that Eq. (3.37) is valid. The short circuit current density J_{SC} of a solar cell is determined by the generation rate G, and the collection probability f_c. The generation rate is determined by the following factors: the absorption coefficient of the semiconductor, the intensity and spectrum of the light, and the position within the cell x. The collection probability is the probability that a carrier generated by the light contributes to J_{SC}. To obtain J_{SC}, we have to consider the contributions of all carriers evaluating the integral

$$J_{SC} = \int_{0}^{W} f_C(x)G(x)dx,$$

(A. 1)

where $x = 0$ is placed at the np junction. If we consider an infinitely thick cell, the collection probability becomes [118]

$$f_C(x) = \exp\left(-\frac{x}{L_n}\right).$$

(A. 2)

This equation says that if a carrier is generated at the junction ($x = 0$), it will contribute to J_{SC} with a probability of 1. For carriers generated at $x > 0$, the probability decreases exponentially with a decay constant given by the diffusion length L_n. Carriers generated at distances greater than L_n from the junction are unlikely to be collected by it, and will not contribute to J_{SC}. Considering a cell of finite thickness, with a recombination velocity S_b in the back contact, $f_C(x)$ is given by [32]

$$f_C(x) = \frac{\cosh\left(\frac{W-x}{L_n}\right) + \sigma\sinh\left(\frac{W-x}{L_n}\right)}{\cosh\left(\frac{W}{L_n}\right) + \sigma\sinh\left(\frac{W}{L_n}\right)},$$

(A. 3)

where $\sigma = S_b L_n / D_n$. The aim of the following discussion is to show that Eq. ((A. 1) can be expressed by Eq. (3.37) using an effective diffusion length that considers the finite thickness. In that case, the collection probability of Eq. (A.3) is approximated by the expression

$$f_{C,approx}(x) = \exp\left(-\frac{x}{L_{eff}}\right).$$

(A. 4)

In monocrystalline cells, the effective diffusion length corresponds to the so-called injection diffusion length described by Eq. (8) in Ref. [66]. This quantity is expressed as

$$L_{mono} = L_n \frac{\cosh\left(\dfrac{W}{L_n}\right) + \sigma\sinh\left(\dfrac{W}{L_n}\right)}{\sinh\left(\dfrac{W}{L_n}\right) + \sigma\cosh\left(\dfrac{W}{L_n}\right)}. \qquad (A.\ 5)$$

Figure 6.25 shows the functions f_c and $f_{c,approx}$ for two different values of L_n/W. Comparing the curves, we note that the differences between f_c and $f_{c,approx}$ are larger when x approaches W, and for cells with diffusion lengths greater than the cell thickness. This differences also depend on σ, which in this case is $\sigma = 10$.
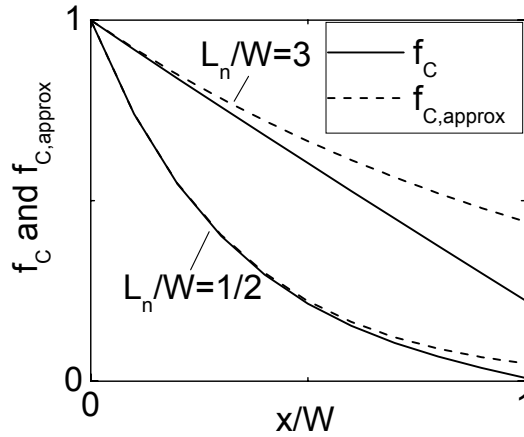

Figure 6.25: The difference between the approximate function $f_{c,approx}$ and f_c is negligible for low values of L/W, becoming larger when $L/W > 1$. Additionally, when x tends to $x = 0$, the differences disappear, regardless of the ratio L/W.

What is the error we introduce when using $f_{c,approx}$ to evaluate J_{SC} with Eq. (3.37)? In order to estimate it, I compare the integrals F_c and $F_{c,approx}$ of f_c and $f_{c,approx}$ integrated from $x = 0$ to $x = W$. Figure 6.26 shows the relative error $(F_{c,approx} - F_c)/F_c$ for all the possible values of σ, and all practical values of the ratio L_n/W. The error that can be made using $f_{c,approx}$ is always smaller than 25 %, and in most practical cases, where $0.1 < \sigma < 10$, the error does not exceed about 10 %.

Note that the error calculated in this way is the *maximum error* that can be made in the evaluation of J_{SC}, because when using Eq. (3.37), the function $G(x)$ accentuates the values of $f_{c,approx}$ at small x, where the error is negligible, as shown in Figure 6.25.
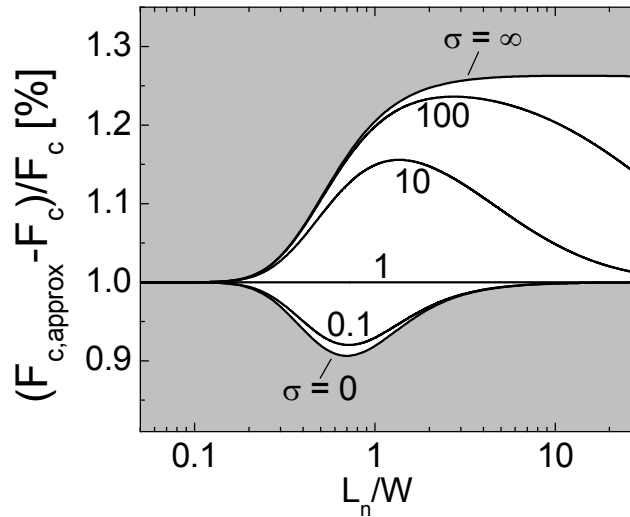
Figure 6.26: This curves show that a maximum relative error of 25 % can be introduced in J_{SC}, when using the approximate function $f_{c,approx}$ instead of the exact expression given by f_c. For most practical cases, it holds $0.1 < \sigma < 10$, and the error stays below 10 %.

Herewith, I proved that using $f_{c,approx}$ with L_{eff} is a valid approximation. This is useful from two points of view. On the one hand, we gain the simplicity of the simple exponential function given by $f_{c,approx}$, allowing a rapid physical interpretation of the collection probability like in the case of an infinitely thick solar cell. On the other hand, $f_{c,approx}$ permits an uncomplicated adaptation of J_{SC} for *polycrystalline np* cells: we only have to replace L_{eff} by the value L_{poly} given in Eq. (3.38).

The curves shown in Figure 3.3 are calculated with $f_{c,approx}$, taking L_{eff} and W as parameters, and integrating numerically with the generation rate $G(x)$ that depends on the thickness W. To obtain $G(x)$, I simulated numerically the absorption of the sun's light in a silicon structure with an Aluminium back contact that acts as a light reflector, and a 100 nm thick SiO_2 antireflective top layer facing the light. To simulate the diffusive reflectance of light produced by the roughness of surfaces, the simulation software introduces a Lambertian coefficient, which randomizes the direction of a light ray after reflection at a surface. Such light trapping layers are standards in solar cell technology. The ray tracing program utilized for the simulation is Sunrays, presented in [119].

Appendix B

To solve the continuity equation, I first write it in terms of *scaled parameters*. The scaling is done in order to obtain simplifications of the rather lengthy expressions that result after solving the continuity equation. These *scaled parameters* are functions of the physical parameters of the cell and its material. In the leftmost column of Table B.1, I introduce physical parameters such as the distance x, the electron concentration n, the diffusion length L, the recombination velocity S at the contacts, the potential drop in the i-layer V-V_{bi}, and the optical generation rate G. The central column of Table B.1 gives the definitions of the corresponding scaled counterparts, x_s, n_s, L_s, S_s, V_s, and G_s.

Table B.1: The scaled quantities, derived from the physical parameters, and the allotted range for the simplified solutions of the *J(V)* equation given in Chapter 3.

physical quantity	scaled quantity	range
distance x	$x_s = \dfrac{x}{W}$	$0 \leq x_s \leq \frac{1}{2}$
electron concentration n	$n_s = \dfrac{n}{n_{p0}}$	$1 \leq n_s$
diffusion length L	$L_s = \dfrac{L}{W}$	$L_s \leq 10$
surface recombination velocity S	$S_s = \dfrac{SW}{D}$	$S_s \leq 10^3$
potential drop V - V_{bi}	$V_s = \dfrac{V - V_{bi}}{V_t}$	$-V_{bi}/V_t \leq V_s < 0$
generation rate G	$G_s = \dfrac{G\tau}{n_{p0}}$	$10^5 \leq G_s \leq 10^{13}$

The simplified expressions of *J* given in chapter 5 are limited to specific ranges of some of the scaled parameters, shown in the rightmost column of Table B.1. These ranges are very wide and account for many combinations of physical parameters. The range for x_s is fixed by the geometry rather than by any simplification criteria. The range given for n_s means that the minority carrier

concentration at the doped layers is higher than the equilibrium value under injection conditions, i.e. with an applied voltage in forward bias mode.

General solution. When using the dimensionless quantities, the steady-state continuity equation for a region of space where the electrons are minority carriers reads

$$G_s + \exp(-V_{s0}x_s) - n_s(x_s) + L_s^2 V_s \frac{dn_s}{dx_s} + L_s^2 \frac{d^2 n_s}{dx_s^2} = 0 \qquad (B.1)$$

where $V_{s0} = -V_{bi}/V_t$. The general solution of this equation is given by

$$n_s(x_s) = G_s + n_s^* \exp(-V_{s0}x_s) + C_1 \exp(\lambda_1 x_s) + C_2 \exp(\lambda_2 x_s) \qquad (B.2)$$

where $n_s^* = \left(1 + (V_s - V_{s0})L_s^2 V_{s0}\right)^{-1}$, and the Eigenvalues λ_1 and λ_2 are given in chapter 5.

Boundary conditions. The surface recombination velocity at $x_s = 0$, produces the recombination current $S_s(n_s(0)-1)$ and equals the drift and diffusion currents, giving

$$S_s(n_s(0) - 1) = V_s n_s(0) + \frac{dn_s}{dx_s}\bigg|_{x_s=0} \qquad (B.3)$$

The second boundary condition uses the value of the electron concentration in the middle of the cell at $x_s = \frac{1}{2}$, assuming E_{Fn} = constant for $x \leq x_C$. The scaled expression of this boundary condition yields

$$n_s(1/2) = n(x_C)/n_{p0} \qquad (B.4)$$

replacing $n(x_C)$ and n_{p0}, this expression gives $n_s(1/2) = (n_i/n_{p0})exp(V/2V_t)$.

With Eq. (B2), and the boundary conditions given by Eq. (B.3) and (B.4), the constants C_1 and C_2 are determined, being

$$C_1 = -\frac{\exp(-\lambda_2/2)}{A_3}\left[A_1(\lambda_2 + S_s) + A_2 \exp(\lambda_1/2)\right], \qquad (B.5)$$

and

$$C_2 = \frac{\exp(-\lambda_2/2)}{A_3}\left[A_1(\lambda_1 + S_s) + A_2 \exp(\lambda_2/2)\right], \qquad (B.6)$$

where the quantities A_1, A_2 and A_3 are defined by

$$A_1 = n_s(1/2) - G_s - n_s^* \exp(-V_{s0}/2), \qquad (B.7)$$

$$A_2 = n_s^*(S_s - V_s + V_{s0}) - S_s + G_s(S_s - V_s), \text{ and} \qquad (B.8)$$

$$A_3 = -\lambda_2 - S_s + (\lambda_1 + S_s)\exp\left(\frac{\lambda_1 - \lambda_2}{2}\right). \qquad (B.9)$$

Using the solution for $n_s(x_s)$, I calculate the scaled current density J_s, integrating the generation-recombination term from $x = 0$ to $x = W/2$, adding the current density due to surface recombination, and multiplying by 2 in order to account for the hole current. The integration is done on the scaled coordinate x_s, resulting the scaled total current density

$$J_s = 2S_s(n_s(0) - 1) + 2\int_0^{1/2} \frac{n_s(x_s) - \exp(-V_{s0}x_s) - G_s}{L_s^2} dx_s. \qquad (B.10)$$

Replacing n_s from Eq. (B.2) in Eq. (B.10) and solving the integral, J_s becomes

$$J_s = 2S_s(C_1 + C_2 + G_s + n_s^* - 1) +$$
$$\frac{1}{L_s^2}\left[\frac{C_1(\exp(\lambda_2/2) - 1)}{\lambda_2/2} - \frac{C_2(1 - \exp(\lambda_1/2))}{\lambda_1/2} - \frac{(n_s^* - 1)(1 - \exp(-V_{s0}/2))}{-V_{s0}/2}\right]. \qquad (B.11)$$

The current density J in A/cm^2 is then given by

$$J = \frac{qn_{p0}D}{W}J_s, \qquad (B.12)$$

where the factor that multiplies J_s results from the scaling transformations.

Simplifications. Firstly, I obtain simplifications of the dark current density, having $G_s = 0$. At forward bias conditions (i.e. $V_{s0} < V_s$), it holds that $n_s(1/2) \gg n_s^*\exp(-V_{s0})$, which implies that $A_1 \approx n_s(1/2)$. Considering additionally the ranges of Table B.1, we find that $A_2 \ll A_1$, and $A_3 \approx (\lambda_1 + S_s)\exp[(\lambda_1 - \lambda_2)/2]$. With these equations, C_2 simplifies to $C_2 \approx n_s(1/2)\exp(-\lambda_1/2)$, and $C_1 \approx -C_2[(\lambda_2 + S_s)/(\lambda_1 + S_s)]$. Now I simplify the current density of Eq. (B.11). At forward biases, all terms in Eq. (B.11) containing n_s^* are negligible. Assuming also that the forward bias stays below V_{bi} (i.e. $V_s < 0$), it holds $\lambda_1 > \lambda_2$; which implies that in Eq. (B.11), the term with $\exp(\lambda_2/2)$ is negligible. With these simplifications, and considering Eq. (B.12), I obtain Eq. (5.9) of chapter 5. Additionally, at very high values of the surface recombination velocity and $V > 0$, J simplifies to Eq. (6.36), while the saturation current density J_0 is given by Eq. (6.37).

Secondly, under illumination, we have $G_s \neq 0$. The simplified values of A_1 and A_2 yield $A_1 = n_s(1/2) - G_s$ and $A_2 = G_s(S_s - V_s)$, while A_3 is still given by the expression

given in the above paragraph. Unlike the dark case, the values of A_1 and A_2 can be comparable depending on the generation rate, which impedes strong simplifications of C_1 and C_2. Equation (B.11) is simplified by neglecting the 1's and n_s^*, which holds for the ranges shown in Table B.1. The current under illumination simplifies to

$$J_s = 2S_s(C_1 + C_2 + G_s) + \frac{1}{L_s^2}\left[\frac{C_1(\exp(\lambda_2/2)-1)}{\lambda_2/2} + \frac{C_2\exp(\lambda_1/2)}{\lambda_1/2}\right]. \qquad \text{(B. 13)}$$

List of symbols and abbreviations

a_i	mesh spacing in the x-direction at the point i
A	solar cell area, integration constant
a-Si	amorphous silicon
b_j	mesh spacing in the y-direction at the point j
B	radiative recombination coefficient
c-Si	monocrystalline silicon
C_1, C_2	integration constants
C_p, C_n	auger recombination coefficients of holes (p), and for electrons (p)
d	thickness of a thin-film
D, D_p, D_n	diffusion constant, general, of holes (p), and of electrons (n)
E	energy
E_C, E_V	energy level of the edge of the conduction band (C), and of the valence band (V)
E_F	Fermi energy
E_A	activation energy
E_{Fp}, E_{Fn}	Fermi energies of holes (p) and electrons (n)
E_T	energy of a defect level, in de forbidden gap
E_g	band gap energy
f	frequency, mathematical function
f, f_{SRH}	Fermi-Dirac occupancy function, Shockley-Read-Hall occupancy function
f_C, $f_{C,approx}$	carrier collection efficiency (C), approximated carrier collection efficiency (C,approx)
F	electric field
F_0	electric field of a junction under equilibrium conditions
F_{max}	maximum electric field

FF	fill factor
FF_0	fill factor of a cell without resistances
g	grain size, mathematical function
g_{med}	median grain width
GB	grain boundary
G	generation rate of electron-hole pairs
G_S	scaled generation rate
h	Planck's constant
I	electrical current
I_{SC}	short-circuit current
I_{mpp}	current at the maximum power point
J	current density
J_S	scaled current density
J_{SC}	short-circuit current density
J_{mpp}	current density at the maximum power point
J_p , J_n	hole current density (p), electron current density (n)
J_{rec} , J_{phot}	recombination current density (rec), photonic current density (ph)
J_0, J_{01}, J_{02}	diode saturation current density, (01) base component, (02) space-charge region component
k	Boltzmann's constant
l	mean free path of charge carriers
$lc\text{-}Si$	laser-crystallized silicon
L , L_{eff}	diffusion length, effective diffusion length
L_p , L_n	hole diffusion length (p), electron diffusion length (n)
L_S	scaled diffusion length
$L_{eff,mono}$	effective diffusion length of a monocrystalline silicon pn solar cell

$L_{eff,poly}$	effective diffusion length of a polycrystalline silicon pn solar cell
$L^0_{eff,mono}$	minimum of $L_{eff,mono}$
n	ideality factor of a diode
n , n_0	electron concentration, electron concentration in equilibrium
n_{p0}	electron concentration in a p-type material, in equilibrium
n_i	intrinsic carrier concentration
n_t	electron concentration at a trapping level
n_1	electron coefficient in Shockley-Read-Hall statistics
n_{GB}	electron concentration at a grain boundary
n_S , n_S^*	scaled electron concentrations
N_A , N_A^-	concentration of acceptor atoms (A), concentration of ionized acceptor atoms (A, -)
N_{BULK}	density of defects in bulk material
N_C,N_V	effective density of states of the conduction band (C), effective density of states of the valence band (V)
N_d	density of dopant atoms
N_{GB}	total density of defects at the grain boundary, effective density of states at the grain boundary
N_t , N^0_t	density of defect states, minimum density of defect states
N_D , N_D^+	concentration of donor atoms (D), concentration of ionized donor atoms (D, +)
p , p_0	hole concentration, equilibrium hole concentration
$\overline{p}$	mean hole concentration
p_{n0}	hole concentration in a n-type material, in equilibrium
p_t	hole concentration at a trapping level
p_1	hole coefficient in Shockley-Read-Hall statistics
p_{GB}	hole concentration at a grain boundary
P , P_{light}	power, light power

q	elementary charge
Q	quality factor of a laser-crystallized film
Q_{GB}	charge at a grain boundary
QFL	Quasi Fermi Level
r	reflectance
r_1, r_2	reflectance at a front surface (1), and at a rear surface (2)
r_S	characteristic relative resistance
R_S, R_P	series resistance (S), parallel resistance (P)
R	Recombination rate
$R_{radiative}$, R_{Auger}, $R_{defects}$	radiative recombination rate, Auger-rate, and recombination rate through defects
R_{SRH}	Shockley-Read-Hall recombination rate
S	recombination velocity
S_b	recombination velocity at a back-contact of a solar cell
S_p, S_n	recombination velocity of holes (p), and of electrons (n)
S_s	scaled recombination velocity
S_C	recombination velocity at a metal/semiconductor contact
S_{GB}, S^*_{GB}	recombination velocity at a grain boundary, maximum recombination velocity at a grain boundary (max)
t	optical transmittance
T	absolute temperature
TF	thin film
TFT	thin film transistor
V	voltage
V_b, $V_{b,max}$	band bending (b), maximum band bending (b, max)
V_{OC}	open-circuit voltage
V_{mpp}	voltage at the maximum power point

V_s	scaled potential drop
V_{s0}	scaled potential drop voltage at zero voltage
W	width of a solar cell
x, y	spatial coordinates
x_C	coordinate x at a center
x_s	scaled coordinate x
z	constant
α	absorption coefficient
α_{exp}	experimentally measured absorption coefficient
$\alpha_{a\text{-}Si}$, $\alpha_{c\text{-}Si}$	absorption coefficient of amorphous silicon (a-Si), absorption coefficient of crystalline silicon (c-Si)
β	crystalline volume fraction
χ_{Si}	electron affinity of silicon
δ	width of a grain boundary
Δx	vertical displacement between two laser pulses
$\Delta\rho$	change in resistivity
$\Delta\rho_{GB}$	change in resistivity of a grain boundary (GB)
$\Delta\sigma_{GB}$	change in conductivity of a grain boundary
ε_0, ε_S	absolute dielectric constant of vacuum (0), relative dielectric constant of a semiconductor (S)
ϕ_m	work function of a metal
ϕ_{phot}	photon flux
$\overline{\Phi}$	barrier height at a grain boundary
η	solar cell efficiency, refraction index
$\eta_{c\text{-}Si}$, $\eta_{substrate}$	refraction index of crystalline silicon (c-Si), refraction index of a substrate
λ	wavelength

λ_1, λ_2	eigenvalues
μ	carrier mobility
μ_H	Hall mobility
μ_p, μ_n	mobility of holes (p), mobility of electrons (n)
μ_{GB}, μ_{pGB}	mean mobility of carriers at a grain boundary, hole mobility at a grain boundary
ν	photon frequency
ρ	resistivity
ρ_0, ρ_{GB}	resistivity of crystalline silicon (0), resistivity of a grain boundary (GB)
σ_0, σ_{GB}	conductivity of crystalline silicon (0), conductivity of a grain boundary (GB)
σ	contact recombination parameter
σ_g	relative width of a distribution of grain widths
σ_Φ	standard deviation of a distribution of barrier heights
τ, τ^*, τ_{eff}	lifetime, maximum lifetime, effective lifetime
τ_{0p}, τ_{0n}	capture-emission lifetimes for holes (0p), and electrons (0n) in the frame of the Shockley-Read-Hall statistics
τ_p, τ_n	hole lifetime, electron lifetime
ζ	difference between Fermi-level and valence band edge (in V)
Λ	grain size distribution function
Ω	phonon frequency
Ψ	electrostatic potential

Literature

[1]   A. Goetzberger, and Ch. Hebling, Solar Energy Materials and Solar Cells **62**, 1 (2000)

[2]   M. Schmela and J. Siemer, Photon **4**, 32 (2002)

[3]   See for example C. W. Pearce, in *VLSI Technology*, edited by S. M. Sze (Mc Graw-Hill, Singapore, 1988), p. 11

[4]   See discussion in D. Hartmann, *Ganzheitliche Bilanzierung der Stromerzeugung aus regenerativen Energien*, Dissertation thesis, (University Stuttgart 2001), p. 162

[5]   K. R. Catchpole, M. J. McCann, K. J. Weber, and A. W. Blakers, Solar Energy Materials and Solar Cells **68**, 173 (2001)

[6]   P. M. Smith, P. G. Carey, and T. W. Sigmon, Appl. Phys. Lett. **70**, 342 (1997)

[7]   T. Sameshima, Solid State Phenomena **37-38**, 269 (1994)

[8]   K. Yamamoto, M. Yoshimi, Y. Tawada, Y. Okamoto, A. Nakajima, S. Igari, Applied Physics A **69**, 179 (1999)

[9]   A. Gosh, Ch. Fishman, and T. Feng, J. Appl. Phys. **51**, 446 (1980)

[10]   R. B. Bergmann, Recent. Res. Devel. Crystal Growth Res. **1**, 241 (1999)

[11]   A. S. Grove, *Physics and Technology of Semiconductor Devices* (John Wiley & Sons, New York, 1967), p.116

[12]   See page 133 in Ref. [11]

[13]   S. M. Sze, *Physics of Semiconductor Devices* 2nd edition, (John Wiley & Sons, New York, 1981), p. 51

[14]   D. K. Schroder, *Semiconductor Material and Device Characterization* (John Wiley & Sons, New York, 1998), p. 422

[15]   J. H. Werner and H.J. Queisser, Mat. Res. Soc. Symp. Proc. **106**, 53 (1988)

[16]   E. H. Rhoderick, and R. H. Williams, *Metal-Semiconductor Contacts* (Oxford University Press, Oxford, 1988), p. 7

[17]   S. Hirae, M. Hirose und Y. Osaka, J. Appl. Phys. **51**, 1043 (1980)

[18]   H. C. de Graaf, M. Huybers und J. G. de Groot, Solid-State Electron. **25**, 67 (1981)

[19]   J. H. Werner und M. Peisl, Phys. Rev. B **31**, 6881 (1985)

[20]   C. R. Grovenor, J. Phys. C 18, 4104 (1985)

[21] M. Kohyama and R. Yamamoto, in *Polycrystalline Semiconductors III*, edited by H.P. Strunk, J.H. Werner, F. Fortin, O. Bonnaud (Scitec Publications, Switzerland, 1994), p. 55-66

[22] T. Kamins, J. Appl. Phys. **42**, 4362 (1971)

[23] J. Seto, J. Appl. Phys. **46**, 5250 (1975)

[24] J. H. Werner, and N. E. Christensen, in *Springer Proceedings in Physics, Vol. 54: Polycrystalline Semiconductors II*, edited by J.H.Werner and H.P.Strunk (Springer, Heidelberg, Germany, 1991), p. 145-150

[25] T. Kamins, Polycrystalline Silicon for Integrated Circuit Applications (Kluwer Academic, Norwell, 1996), 178

[26] See for example J. Schmidt and A. G. Aberle, J. Appl. Phys. **81**, 6186 (1997)

[27] See Ref. [9].

[28] R. B. Bergmann, Appl. Phys. A **69**, 187 (1999)

[29] K. R. Catchpole, M. J. McCann, K. J. Weber, and A.W. Blakers, Solar Energy Materials and Solar Cells **68**, 173 (2001)

[30] J. H. Werner, K. Taretto, and U. Rau, Solid State Phenomena **80-81**, 299 (2001)

[31] A. Goetzberger, B. Voß, and J. Knobloch, *Sonnenenergie: Photovoltaik* (Teubner, Stuttgart, 1997), p. 94

[32] See, for example, P. Basore, in *Proc. 23rd IEEE-Photovoltaic Specialists Conf.* (IEEE, New York, 1993), p. 149

[33] N. Jensen, U. Rau, R. M. Hausner, S. Uppal, L. Oberbeck, R. B. Bergmann, and J. H. Werner, J. Appl. Phys. **87**, 2640 (2000)

[34] L. Oberbeck, *Ionenassistierte Deposition von Siliciumschichten*, Dissertation thesis, (University Stuttgart 2001)

[35] F. Duerinckx, J. Szlufcik, Solar Energy Materials & Solar Cells **72**, 231 (2002)

[36] A. Poruba, A. Fejfar, Z. Remes, J. Springer, M. Vanecek, J. Kocka, J. Meier, P. Torres, and A. Shah, J. Appl. Phys. **88**, 148 (2000)

[37] R. Brendel and U. Rau, Solid State Phenomena **67-68**, 81 (1999)

[38] A. Takami, S. Arimoto, H. Morikawa, S. Hamamoto, T. Ishihara, H. Kumabe and T. Murotani, in *Proc. 12th Europ. Photovoltaic Solar Energy Conf.* (H. S. Stephens & Assoc., Bedford, 1994), p. 59

[39] Y. Bai, D. H. Ford, J. A. Rand, R. B. Hall and A. M. Barnett, in *Proc. 26th IEEE Photovoltaic Specialists Conf.* (IEEE, Piscataway, 1997), p. 35

[40] C. Hebling, S. W. Glunz, J. O. Schumacher, and J. Knobloch, in *Proc. 14th Europ. Photovoltaic Solar Energy Conf.*, (H. S. Stephens & Assoc., Bedford, 1997), p. 2318

[41] T. Mishima, S. Itoh, G. Matuda, M. Yamamoto, K. Yamamoto, H. Kiyama, and T. Yokoyama, in *Tech. Digest 9th Int. Photovolt. Solar Energy Conf.* (Dept. Electrical and Eletronic Engin., Tokyo, 1996), p. 243

[42] M. Spiegel, C. Zechner, B. Bitnar, G. Hahn, W. Jooss, P. Fath, G. Willeke, E. Bucher, H.-U. Höfs, and C. Häßler, Solar Energy Materials & Solar Cells **55**, 331 (1998)

[43] R. Auer, J. Zettner, J. Krinke, G. Polissky, T. Hierl, R. Hezel, M. Schulz, H. P. Strunk, F. Koch, D. Nikl, H. v. Campe, in *Proc. 26th IEEE Photovoltaic Specialists Conf.* (IEEE, Piscataway, 1997), p. 739

[44] A. Slaoui, S. Bourdais, G. Beaucarne, J. Poortmans, and S. Reber, Solar Energy Materials & Solar Cells **71**, 245 (2002)

[45] F. Tamura, Y. Okayasu, K. Kumagai, in *Techn. Digest 7th Intern. Photovolt. Sci. Eng. Conf.* (Dept. Electric. and Computer Eng., Nagoya, 1993), p. 237

[46] R. Shimokawa, K. Ishii, H. Nishikawa, T. Takahashi, Y. Hayashi, I. Saito, F. Nagamina, S. Igari, Solar Energy Materials & Solar Cells **34**, 277 (1994), the value of the doping concentration in the base was given in K. Ishii, H. Nishikawa, T. Takahashi, and Y. Hayashi, Jpn. J. Appl. Phys. **32**, L 770 (1993)

[47] H. S. Reehal, M. J. Thwaites, T. M. Bruton, phys. stat. sol. (a) **154**, 623 (1996)

[48] G. Beaucarne, M. Caymax, I. Peytier, and J. Poortmans, Solid State Phenomena **80-81**, 269 (2001)

[49] R. Brendel, R. B. Bergmann, B. Fischer, J. Krinke, R. Plieninger, U. Rau, J. Reiß, H. P. Strunk, H. Wanka, and J. H. Werner, in *Conf. Rec. 26th IEEE Photovolt. Spec. Conf.* (IEEE, New York, 1997), p. 635

[50] See page 180 in Ref. [8].

[51] T. Matsuyama, N. Terada, T. Baba, T. Sawada, S. Tsuge, K. Wakisaka, S. Tsuda, J. Non-Cryst. Solids **198-200**, 940 (1996)

[52] K. Saito, M. Sano, K. Matzuda, T, Jibdim N, Higasikawa, and T. Kariya, in *Techn. Digest 11th Intern. Photovolt. Sci. Eng. Conf.*, ed. T. Saitoh (Tokyo Univ. A&T, Tokyo, 1999), p.229

[53] O. Vetterl, F. Finger, R. Carius, P. Hapke, L. Houben, O. Kluth, A. Lambertz, A. Mück, B. Rech, and H. Wagner, Solar Energy Materials & Solar Cells **62**, 97 (2000)

[54] M. Kondo and A. Matsuda, Thin Solid Films **383**, 1 (2000)

[55] private communication of J. H. Werner with Michio Kondo, 21 July 2000

[56]   N. Wyrsch, P. Torres, M. Goerlitzer, E. Vallat, U. Kroll, A. Shah, A. Poruba, M. Vanecek, Solid State Phenomena **67-68**, p. 89

[57]   H. Keppner, J. Meier, P. Torres, D. Fischer, A. Shah, Applied Physics A **69**, 169 (1999)

[58]   M. A. Green, *Solar Cells* (Prentice-Hall, Englewood Cliffs, 1982), p. 97

[59]   J. H. Werner, in *Techn. Dig. 13th Sunshine workshop on Thin Film Solar Cells*, ed. by M. Konagai (NE-DO, Tokyo, Japan, 2000) p. 41

[60]   See page 95 in Ref. [58].

[61]   See for example Eq. 37 in C. H. Seager, J. Appl. Phys. **52**, 3960 (1981)

[62]   K. Taretto, Analytische Modelle für die elektrischen Eigenschaften von polykristallinem Silicium, internal publication of the IPE (University Stuttgart, 1999)

[63]   See for example Eq. 6.26 in P. Würfel, *Physik der Solarzellen* (Spektrum, Heidelberg, 1995), p. 104

[64]   D. M. Kim, A. N. Khondker, S. S. Ahmed, and R. R. Shah, IEEE Trans. Electron Devices **ED-31**, 480 (1984)

[65]   K. Seeger, *Semiconductor Physics* (Springer, Berlin-Heidelberg, 1999), p. 161

[66]   See page 147 in Ref. [32].

[67]   K. L. Chopra, *Thin Film Phenomena* (McGraw-Hill, New York, 1969), 434

[68]   H. Keppner, J. Meier, P. Torres, D. Fisher, and A. Shah, Appl. Phys. **A 69**, 169 (1999)

[69]   K. Yamamoto, M. Yoshimi, Y. Tawada, Y. Okamoto, A. Nakajima, and S. Igari, Appl. Phys. **A 69**, 179 (1999)

[70]   K. Yamamoto, T. Suzuki, M. Yoshimi, and A. Nakajima, in *Proc. 25th IEEE Photovoltaic Specialists Conf.* (IEEE, Washington, 1996), p. 661

[71]   G. Beaucarne, J. Poortmans, M. Caymax, J. Nijs, and R. Mertens, IEEE Trans. Electron Devices **ED-47**, 1118 (2000)

[72]   T. Matsui, H. Takakura, and Y. Hamakawa, in *Intern. Technical Digest PVSEC-11*, ed. by T. Saitoh (Tokyo University of Agriculture and Technology, Tokyo, 1999), p. 711

[73]   K. Kurobe, Y. Ishikawa, Y. Yamamoto, T. Fuyuki, and H. Matsunami, in *Intern. Technical Digest PVSEC-11*, ed. by T. Saitoh (Tokyo University of Agriculture and Technology, Tokyo, 1999), p. 295

[74] S. A. Edminston, G. Heiser, A. B. Sproul, and M. A. Green, J. Appl. Phys. **80**, 6784 (1996)

[75] G. A. M. Hurkx, D. B. M. Klaassen, and M. P. G. Knuvers, IEEE Trans. Electron Devices **ED-39**, 331 (1992)

[76] S. Selberherr, Analysis and Simulation of Semiconductor Devices (Springer, Wien, 1984), p. 80

[77] R. Brendel and H. J. Queisser, Solar Energy Materials and Solar Cells **29**, 397 (1993)

[78] M. A. Green, *High Efficiency Silicon Solar Cells* (Trans Tech Publications, Switzerland , 1987), p. 94

[79] See page 92 in Ref. [78].

[80] R. Crandall, J. Appl. Phys. **54**, 7176 (1983)

[81] H. Okamoto, H. Kida, S. Nomomura, K. Fukumoto, and Y. Hamakawa, J. Appl. Phys. **54**, 3236 (1983)

[82] See page 75 in Ref. [13].

[83] See page 85 in Ref. [13].

[84] C. Sah, R. Noyce, and W. Shockley, Proc. IRE **45**, 1228 (1957)

[85] E. Rhoderick and R. Williams, *Metal-Semiconductor Contacts* (Clarendon Press, Oxford, 1988), p. 93

[86] See page 57 in Ref. [13].

[87] M. Goerlitzer, P. Torres, C. Droz, and A. Shah, Solar Energy Materials & Solar Cells **60**, 195 (2000)

[88] P. A. Basore, IEEE Trans. Electron Devices **ED-37**, 337 (1990)

[89] N . Wyrsch, L. Feitknecht, C. Droz, P. Torres, A. Shah, A. Poruba, and M. Vanecek, J. Non-Cryst. Solids **266-269**, 1099 (2000)

[90] L. Pichon, K. Mourgues, F. Raoult, T. Mohammed-Brahim, K. Kis-Sion, D. Briand, and O. Bonnaud, Semicond. Sci. Technol. **16**, 918 (2001)

[91] R. R. Shah, D. Hollingsworth, and D. Lloyd Crosthwait, Mat. Res. Soc. Symp. Proc. **5**, 325 (1982)

[92] Y. Helen, R. Dassow, M. Nerding, K. Mourges, F. Raoult, J. R. Köhler, T. Mohammed-Brahim, R. Rogel, O. Bonnaud, J. H. Werner, and H. P. Strunk, Thin Solid Films **383**, 143 (2001)

[93]   See for example H.-G. Rubahn, Laseranwendungen in der Oberflächenphysik und Materialbearbeitung (Teubner, Suttgart, 1996), p. 88

[94]   R. Dassow, *Laserkristallisation von Silizium*, Dissertation Thesis, (University Stuttgart, 2001)

[95]   M. Nerding, S. Christiansen, J. Krinke, R. Dassow, J. R. Köhler, J. H. Werner, and H. P. Strunk, Thin Solid Films **383**, 112 (2001)

[96]   J. C. C. Tsai, in *VLSI Technology*, edited by S. M. Sze (Mc Graw-Hill, Singapore, 1988), p. 309

[97]   *Smithells Metal Reference Book*, edited by E. A. Brandes and G. B. Brook (Butterworth-Heinemann, Oxford, 1998), chapter 14

[98]   J. H. Werner and U. Rau, in *Silicon-Based Millimeter-Wave Devices*, edited by Luy et al. (Springer, Berlin, 1994), p. 97

[99]   V. E. Borisenko, *Semiconducting Silicides* (Springer, Berlin, 2000), p. 56

[100] E. Mollwo, in *Landolt-Börnstein – Zahlenwerte und Funktionen aus Naturwissenschaften und Technik*, edited by K. H. Hellwege and J. L. Olsen (Springer, Berlin 1985),**15b**, p .56

[101] M. Nerding, S. Christiansen, J. Krinke, R. Dassow, J. R. Köhler, J. H. Werner, and H. P. Strunk, Thin Solid Films **383**, 110 (2001)

[102] R. B. Bergmann, J. Krinke, H. P. Strunk, and J. H. Werner, Mater. Res. Soc. Symp. Proc. **467**, 325 (1997)

[103] D. K. Schroder, *Semiconductor Material and Device Characterisation* (John Wiley & Sons, New York, 1998), p. 634

[104] J. R. Köhler, R. Dassow, R. B. Bergmann, J. Krinke, H. P. Strunk, and J. H. Werner, Thin Solid Films **337**, 129 (1999)

[105] See page 189 in Ref. [58].

[106] See page 334 in Ref. [65].

[107] N. Jensen, Optische und elektrische Charakterisierung neuartiger polykristalliner Siliziumschichten auf Glassubstraten, Diploma thesis, (University Stuttgart, 1997)

[108] J. H. Werner and U. Rau, in *Silicon-Based Millimeter-Wave Devices*, edited by Luy et al. (Springer, Berlin, 1994), p.89

[109] See page 634 in Ref. [103].

[110] W. Cho, Y. Takeuchi, and H. Kuwano, Solid-State Electron. **37**, 1573 (1994)

[111] D. Yang, J. Lu, L. Li, H. Yao, and D. Que, Appl. Phys. Lett. **59**, 1227 (1991)

[112] See for example Ref. [20].

[113] M. A. Green, J. Appl. Phys. **80**, 1515 (1996)

[114] J. H. Werner, in *Polycrystalline Semiconductors III*, edited by H.P. Strunk, J. H. Werner, F. Fortin, O. Bonnaud (Scitec Publications, Switzerland, 1994), p. 213

[115] Y. Helen, R. Dassow, K. Mourges, O. Bonnaud, T. Mohammed-Brahim, F. Raoult, J. R. Köhler, J. H. Werner, and D. Lemoine, in *International Electron Devices Meeting 1999* (Electron Devices Soc. IEEE, Piscataway, NJ, USA, 1999), p. 297

[116] M. S. Bennet, J. Appl. Phys. **58**, 3470 (1985)

[117] J. W. Orton and P. Blood, The Electrical Characterization of Semiconductors: Measurement of Minority Carrier Properties (Academic Press, London, 1990), p.127

[118] See page 142 in Ref. [58].

[119] R. Brendel, in *Proc. 12th E.C. Photovoltaic Solar Energy Conf.*, ed. By R. Hill, W. Palz, and P. Helm (H.S. Stevens and Associates, Bedford, UK, 1994), p. 1339

Acknowledgments

I would like to thank also my relatives and friends for their support and advice during my stay in Germany. Their encouraging spirit was always present, despite the fact that we were separated by about 15000 kilometers.

Curriculum Vitae

Kurt Rodolfo Taretto

born on April 7 1974 in Buenos Aires, Argentina.

1980-1986   primary school at the *Instituto Primo Capraro* in Bariloche, Argentina.

1987-1991   attends high school at the *Instituto Primo Capraro*.

1992-1994   college studies at the engineering faculty of the *Universidad Nacional del Comahue* in Bariloche, Argentina.

1994-1998   continuates college studies at the engineering faculty of the *Universidad Nacional del Comahue* in Neuquén, Argentina.

1998   obtains the academic degree of *Industrial Engineer oriented to electrical engineering*. Receives a grant from the *FOMEC* programme (Argentina's funding programme for the improvement of academic quality) to work on a thesis project.

1999-2002   works on his thesis project at the *Institut für Physikalische Elektronik* from the *Universität Stuttgart* in Stuttgart, Germany.